Digital Signal Analysis for CsI(Tl) Detectors and the Active-Target at R^3B

Dissertation
zur Erlangung des Grades
"Doktor der Naturwissenschaften"
im Promotionsfach Physik

am Fachbereich Physik, Mathematik und Informatik
der Johannes Gutenberg-Universität Mainz

JOHANNES GUTENBERG
UNIVERSITÄT MAINZ

Joel Silva
geboren in Cadaval, Portugal

Darmstadt, 2016

Gutachter:
Zweiter-Gutachter:
Tag der mündlichen Prüfung: 26. April 2016

D 77, Dissertation Johannes Gutenberg-Universität Mainz

Abstract

Modern experimental setups tend to replace analogue front-end electronics with fully digital systems. The detector signals are sampled in early stages and most of the signal processing is performed digitally. The presented work is divided into two major subjects involving digital signal analysis: firstly employed to correct temperature dependent gain variations and perform particle identification of CsI(Tl) based detectors and secondly to test the functionality of an active-target prototype (AcTar) for the Reactions with Relativistic Radioactive Beams (R^3B) setup.

In the first part of this work a pulse shape based method for monitoring the interior temperature of the CsI(Tl) crystal is proposed. The method uses the correlation between the gain and defined pulse shape parameters to correct the effect of temperature variations in the energy calibration of the corresponding detector system. The suitability of the method was tested using both, a photomultiplier tube (PMT) and an avalanche photodiode (APD) readout photosensor. The analysis shows that the gain changes due to temperature variations can be corrected to a precision better than 1% with both the PMT and APD photosensors, well below the CsI(Tl) intrinsic resolution for ~1 MeV γ-rays. For particle identification, the fuzzy clustering algorithm is used to compute the principle pulse shape associated with the different particle species in an unsupervised fashion. The results show good discrimination between protons and γ-rays.

In the second part of this work the functionality of the AcTar prototype for the R^3B setup has been tested. The objective was to prove the feasibility and performance of such kind of detector with the use of heavy ion beams. As a proof of concept, a ^{58}Ni beam at 700 MeV/u was impinging on a He-H_2 (3%) gaseous target mixture. The presented results show the principle functionalities of the detector and suggest that pulse shape analysis can indeed be used to track the recoil particles and reconstruct the kinematics. It is the first time that an active-target of such kind has been successfully tested with beams heavier than carbon.

Zusammenfassung

Moderne experimentelle Setups tendieren dazu analoge Frontend Elektronik mit vollständig digitalen Systemen zu ersetzen. Die Detektorsignale werden in frühen Stadien abgetastet und die Signalverarbeitung erfolgt weitgehend digital. Die vorliegende Arbeit behandelt zwei Hauptthemen, die die digitale Signalanalyse einbeziehen: zum einen eingesetzt, um temperaturabhängige Verstärkungsänderungen zu korrigieren und Teilchenidentifikation von CsI(Tl) basierten Detektoren durchzuführen und zum anderen, um die Funktionalität eines Active-Target Prototyps (AcTar) für den R^3B Setup zu testen.

Im ersten Teil dieser Arbeit wird ein Pulsform-basierendes Verfahren zur Überwachung der intrinsischen Temperatur des CsI(Tl) Kristalls vorgeschlagen. Das Verfahren nutzt die Korrelation zwischen der Verstärkung und der Pulsform, um die Auswirkung von Temperaturschwankungen in der Energiekalibrierung des entsprechenden Detektorsystems zu korrigieren. Die Eignung des Verfahrens wurde unter Verwendung von jeweils einem Photomultiplier (PMT) und einer Avalanche-Photodiode (APD) als Auslesephotosensor getestet. Die Analyse zeigt, dass die Variation der Verstärkung aufgrund von Temperaturschwankungen, sowohl mit PMT und APD Photosensoren, mit einer Genauigkeit von besser als 1% korrigiert werden können, deutlich unter der CsI(Tl) intrinsischen Auflösung für ~1 MeV γ-Strahlen. Zur Teilchenidentifikation wird der Fuzzy-Clustering-Algorithmus verwendet, um die Grundpulsform entsprechend der verschiedenen Teilchensorten in einer unabhängigen Art und Weise zu bestimmen. Die Ergebnisse zeigen eine gute Diskriminierung zwischen Protonen und γ-Strahlen auf.

Im zweiten Teil der Arbeit wurde die Funktionalität des AcTar Prototyps für das R^3B Setup getestet. Ziel war es, die Durchführbarkeit und die Leistungsfähigkeit dieser Art von Detektoren unter der Verwendung von Schwerionenstrahlen zu beweisen. Als Proof of Concept , wurde ein ^{58}Ni Strahl bei 700 MeV/u und eine He-H_2 (3%) Gasmischung verwendet. Die Ergebnisse bestätigen die Funktionalitäten des Detektors mit den verwendeten Strahl und zeigen auf, dass die Pulsformanalyse in der Tat zur Nachverfolgung der Rückstoßteilchen und zur Rekonstruktion der Kinematik verwendet werden kann. Es ist das erste Mal, dass ein Active-Target dieser Art erfolgreich mit Strahlen schwerer als Kohlenstoff getestet wurde.

To Aurora Filipe,
Carlos Silva,
Emika Bartodziej,
and Carolina Silva.

Contents

Chapter 1

Introduction

The nucleus, at the very core of an atom, is a system of neutrons and protons held together by the strong force. Through research, nuclear physicists provide humanity with insights on the properties and structure of the nuclei and the mechanisms involved in their creation. The goal is to explain conclusively the fundamental physical processes which govern the formation of matter since the moment of the Big Bang and the limits for nuclear stability to help reveal the secrets of how the universe is put together. The most advanced experiments are being performed in large facilities built around accelerators, which require an enormous financial and intellectual contribution from many countries. The investment in nuclear physics provide leading-edge instrumentation, world-class facilities, support and training for the people involved in these researches. The result is a multitude of information that is helping us to understand the atomic nuclei at ever-deeper levels. Among future new facilities, one of the most resourceful is the Facility for Antiproton and Ion Research (FAIR), which is meant to provide particle beams with unprecedented intensity and quality.

Since the discovery of the atomic nucleus through alpha-scattering experiments [1], many nuclei have been identified and extensively studied throughout the 20th century. Our knowledge about the properties and structure of the nuclei is mostly based on studies employing stable nuclei or isotopes close to those stable nuclei, using electromagnetic or hadronic probes with sufficient energy. A substantial amount of experimental knowledge and theoretical background was acquired from investigations based on direct reactions. In particular, light-ion induced scattering reactions have largely contributed with nuclear structure information for stable nuclei. Such reactions are normally carried out in "normal kinematics", i.e. the light ions with intermediate-energy are scattered off a fixed target consisting of the stable nuclei to be investigated.

Although much effort has been made to provide a complete model that describes all nuclear species, different descriptions have been attributed to different areas of the nuclear chart, and short-lived nuclei still remain to a large extent not well known. Nuclei far from stability, characterised by much larger or much smaller ratio of neutron number N to proton number Z (either neutron rich or neutron deficient) compared to stable isotopes, are of major interest in the present days. These nuclei present truly exotic properties providing tests for existing nuclear structure models

and new physics such as halo [1] nuclei [2], new collective modes [3] and new shell closures ("magic numbers") [4]. Regardless of their very brief existence, exotic nuclei play a very important role in understanding the origin of the elements.

With the recent development of facilities employing accelerated beams of unstable nuclei around the world, exotic nuclei have become subject of extensive study. These facilities have considerably extended the number of finite nuclei available for experimentation in nuclear physics and therefore bring new challenges to our understanding of nuclear reactions and nuclear structure. There are primarily two methods for producing exotic nuclei: the Isotope Separation On-Line (ISOL) principle, where the reaction products of a primary beam are thermalised in a thick target and diffuse out to an ion source for further acceleration and separation, and the In-Flight Separation method, which involves in-flight projectile fragmentation of stable heavy-ions in a thin target with further fragment separation. While the fragment separation technique provides a short separation time, which essentially is determined by the flight time through the separator, the ISOL method is thought to provide better beam intensities, but requires longer half-lives. The ISOL method is used in facilities such as the ISOLDE facility at CERN [5], which has been operating since 1992, while the in-flight fragmentation method is available, for example, at the GSI (GSI Helmholtzzentrum für Schwerionenforschung GmbH, Darmstadt, Germany) accelerator facility with the FRS device. The GSI facility is capable of producing beams of every element until Uranium, with energies up to 1 GeV/u.

The upcoming Facility for Antiproton and Ion Research (FAIR[2]) will upgrade the existing GSI facility, aiming to offer an improved beam quality, separation efficiency and beam intensity, which will facilitate the investigation of secondary beam species even further from stability. The future Super FRagment Separator (Super-FRS) is characterised by a much larger phase-space acceptance [6].

The R^3B [7] experiment is a part of the NUclear STructure, Astrophysics and Reactions (NUSTAR) pillar at the FAIR facility, and will be located at the focal plane of the high energy branch of the Super-FRS. It comprises a rather sophisticated experimental setup intended to provide high efficiency, acceptance and resolution for obtaining kinematically complete measurements of reactions induced by relativistic short-lived ion beams up to 1 GeV/u. Including the coincident detection and identification of heavy residues, neutrons, protons and photons. The experimental configuration scheme is based on a concept identical to the existing ALADIN-LAND apparatus, which has been successfully used with secondary beams from the FRagment Separator (FRS) facility at GSI, however, with substantial improvements in resolution. The most essential upgrades concern an extended detection scheme that includes additional detection of light (target-like) recoil particles and a new high-resolution fragment spectrometer, see schematic view in Figure 1.1. The incoming secondary beams are identified and tracked on an event-by-event basis. Measurements of the magnetic rigidity $B\rho$[3], energy loss ΔE, and time-of-flight ToF provide unique identification and momentum determination of the isotopes.

[1] In nuclear physics an atomic nucleus is said to have a nuclear halo if the radius of the nucleus is considerably larger than that predicted by the liquid drop model, in which the nucleus is assumed to have the shape of a sphere with constant density.

[2] The FAIR project is a joint endeavour of sixteen countries widely devoted to the study of exotic nuclei that is expected to serve more than 2000 international users. http://www.fair-center.eu/

[3] Position measurement at the dispersive focus in the Super-FRS

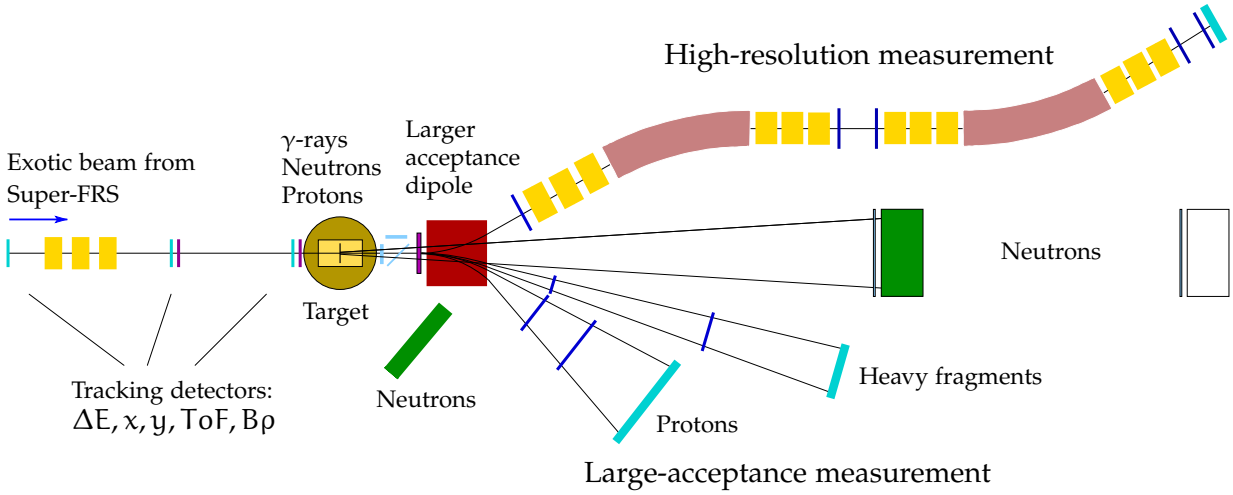

Figure 1.1: Schematic representation of the R^{3}B experimental setup. From the left to the right, the setup is comprised of incoming beam particle tracking, γ-ray and target recoil detection, a large-acceptance dipole magnet, a high resolution magnetic spectrometer, heavy-ion detection, neutron and light-charged particle detection. The target and AcTar will be surrounded by the CALIFA calorimeter.

The versatility of this complex setup with many detection systems, allows to accommodate experiments for studying different types of reactions and physics cases. The experiments proposed to investigate reactions of elastic scattering, inelastic scattering and charge exchange, primarily comprise the use of an active-target, a calorimeter surrounding the target and beam tracking detectors. These will allow registration of the recoil particles in coincidence with heavy fragments and gamma-rays.

The R^{3}B Active-Target detector, hereafter named AcTar, is a gas based ionising chamber which forms simultaneously the target and detection setup. Its design is optimised for direct reaction studies of the nuclear structure of short-lived nuclei at low momentum transfer.

The R^{3}B calorimeter, named CALorimeter for In-Flight emitted gAmmas (CALIFA), is designed to detect the in-flight emission of gamma-rays and light charged particles. It is a highly granular detection system, composed of many inorganic scintillation detectors, that is meant to provide high total absorption capability and exceptional resolution in order to identify gamma cascades and light charged particles. The Active-Target (AcTar) will be placed inside CALIFA for proper coincident detection of the recoils and the emitted gamma-rays.

These detectors will have a large number of output channels. As in most modern experiments, these systems equip fast fully digital electronic readout systems, which implement Analogue to Digital Converter (ADC) based high-speed digitises to allow fully record detector output. The result is the availability of a complete digital signal wave form which can be recurrently accessed to extract features from the signal's pulse shape characteristics.

1.1 Direct reactions in inverse kinematics

Among the experimental methods employed to study the structure of exotic nuclei, direct reactions (e.g. elastic and inelastic scattering reactions of light-ion, transfer reactions) are important, because

transitions can be selectively induced by means of proper choice of a probe and their relatively simple to understand experimental observables. This gives one of the most capable and incisive methods to explain in detail the structural and spectroscopic characteristics of the particles involved.

Nuclei far from stability are subjected to β-decay and thus can only be studied using a Radioactive Ion Beam (RIB); due to their short lifetime no target made of exotic nuclei can be produced. Instead, the target becomes the beam. Furthermore, the information of interest is most readily obtained in reaction where one of the elements involved has a relatively simple structure, e.g. H_2, D_2, ^{3}He and ^{4}He. For these reasons, the reactions induced by radioactive beams normally correspond to inverse kinematics and require the use of light targets. Therefore, detection systems are developed considering these experimental conditions. The information of interest can then be deduced by measuring the kinematical characteristics of the reaction products such as energies and angles.

Although the use of direct reactions with exotic nuclei seems to be intrinsically uncomplicated, different problems may have to be taken into account. First of all, the nuclei further from stability are usually the most interesting. Nevertheless, the production rate of exotic nuclei tends to decrease exponentially with the increase of proton-neutron imbalance and the nuclei of interest are often available only with a rate of few hundred or thousand particles per second. Consequently, the intensities of RIB available at the present facilities are very low (in general many orders of magnitude) compared to primary beams used to study stable nuclei; also their optical qualities (beam size and emittance) are often much poorer.

In order to compensate for these difficulties, new detection systems with fine spacial resolution and high efficiency are mandatory. Additionally, to further increase the reaction counting rate, thick reaction targets also required. The first requisite is generally not easy to achieve, and the second becomes a serious limiting factor as increasing target thickness leads to a high detection threshold and a large uncertainty of the interaction point in the target. That consequently leads to large uncertainties in the kinematic reconstruction and energy resolution, especially when low energy particles are involved.

Moreover, for some of the reactions to be studied (such as for investigation of low lying electric dipole (E1) strengths and giant monopole resonances (GMR)), the most interesting information is concentrated at very low momentum transfer. The recoil particles have typically low energies (few MeV) for the angular region of interest near zero degree in the centre-of-mass system for the case of elastic and inelastic reactions. As an example, the kinematics for the case ^{4}He (^{58}Ni, ^{58}Ni) elastic scattering and ^{4}He (^{58}Ni, ^{58}Ni*) inelastic scattering at the beam energy of 200 MeV/u is illustrated in Figure 1.2. The plot shows the kinetic energy E_{lab} versus the scattering angle in the laboratory frame of recoiling ^{4}He target nuclei. In this region the detection of the light recoil is often rather difficult. Therefore, it demands for high resolution detection of very low energy light target-recoil particles, desirably in coincidence with the projectile to reduce background contamination and enhance the spectra purity.

A well-established solution to overcome most of the experimental challenges above mentioned is the idea of an active-target, in which the target is no longer the inert material but used also to detect particles. Such device consists of a gaseous ionisation detector system, where the nuclei of the gas atoms are also the target nuclei. The low production rates of exotic nuclei can be compensated by a high detection efficiency, which can be as good as 100%. In addition, a very good position resolution in the three dimensions of the active-target allows excellent tracking capability (and so,

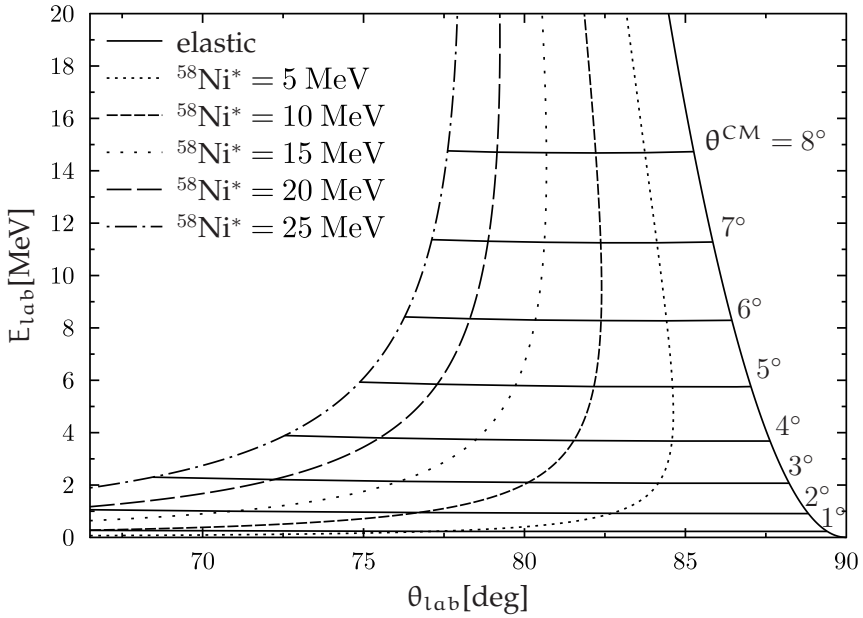

Figure 1.2: Kinematics plot of the energy as function of the angle for ^{4}He (^{58}Ni, ^{58}Ni) elastic and ^{4}He (^{58}Ni, ^{58}Ni*) inelastic scattering (with the excited states of the ^{58}Ni located at the excitation energies E* from 5 MeV up to 25 MeV). The energy of the incoming ^{58}Ni beam is 200 MeV/u. Centre-of-mass angles θ^{CM} are indicated in the curve.

the measurement of angular distributions) and the event-by-event detection of the interaction point between projectile and target nuclei, eliminating this way the energy loss effects associated with thick targets. In certain cases, the target thickness can even be increased to a value in which the incoming beam particle completely stops in the target without loss in resolution, thus optimising the use of the beam particle. A wide variety of target species is achieved via different options for filling gases. Light targets such as H_2, D_2 and He, are mainly available in gaseous form (allowing their use as inverse kinematic reaction target), which can therefore be chosen to optimally suit the purpose of the experiment. The ability to implement different gases enables to choose the one that best suits the experiment purpose. Finally, the problem of the low energy recoil considered above is addressed, as the recoil particles may be detected with an extremely low energy threshold. Another feature consists in exploiting the energy loss of the incident beam in the gas to obtain excitation functions for specific reactions with a single tuning of the accelerator, and thus optimising the beam time.

The active-target concept has rarely been used in nuclear physics research, in which only few active-targets were developed. Prior detectors were designed to be used with specific configurations, therefore allowing reduced experimental flexibility. For instance, the IKAR detector [8, 9] used at GSI, was developed for beam energies of around 1 GeV and operated with H_2 gas at 10 bar pressure. Another examples, are represented by the MSTPC (Multiple Sampling and Tracking Proportional Chamber) [10] designed at RIKEN (Japan), which studies astrophysical nuclear reactions and fusion at low energy using atmospheric pressure and the MAYA[11] detector designed at GANIL[4] (France) for the study of extremely exotic nuclei. Currently, new designs are mostly based on a gas-filled apparatus where the gas constitutes both, the target and the detection medium. Among these, there

[4]Grand Accélérateur National d'Ions Lourds

is the new AcTar detector, which is being developed and build at PNPI[5] as an upgrade of the IKAR detector. This detector consists of an Ionisation Chamber (Ionisation Chamber (IC)) designed for studying elastic and inelastic reactions in the region of very low momentum transfer, at very small scattering angles in the centre-of-mass system.

The AcTar detector is meant to be integrated in the R^3B setup. As part of this setup, the AcTar enables the registration of recoil particles in coincidence with the heavy fragments, neutrons and gamma-rays; and thus extending the R^3B possibilities in studies of nuclear structure of short-lived nuclei. For the R^3B experiment the inverse kinematic reactions will be studied with gaseous targets like: H_2, D_2, ^3He and ^4He, either pure or mixed with standard detection gases such as methane CH_4. The identification and detection of low energy recoil particles is most uniquely performed by an gaseous detector. This approach does not only permit to deduce the energy T_r of the recoil particles, but also their respective polar angle θ_R of scattering and the z-coordinate of the reaction point along the chamber longitudinal axis.

The experimental concept and opportunities of the AcTar detector within the R^3B setup are to a certain extent similar to those of the EXL (EXotic nuclei studied in Light ion induced reactions at the NESR storage ring) project [12]. But the two different projects complement each other in the way that AcTar provides access to experiments with exotic beams with half-lives shorter than 1 s, which are not accessible in EXL. A minimum time is required for beam preparation in the storage ring and for continuous accumulation. In this setup, the accumulation and recirculation of the beam in the ring with typical frequencies of several MHz allow to reach a much higher luminosity compared to regular beam line experiments, without the need of increasing the target thickness.

The employment of an active-target in the future R^3B project is mainly intended for three types of experiments to be performed in inverse kinematics: elastic scattering of exotic nuclei on protons at low momentum transfer, inelastic scattering of exotic nuclei on helium at the region of the giant resonances and charge exchange reactions. The implementation of those tasks differ on their constraints concerning the experimental setups. While, for instance, the investigation of elastic scattering reactions require the measurement of the recoils' energy and angular distribution, for the inelastic scattering reactions not only the recoiled particle needs to be detected but also the gamma-quanta is registered. Since the AcTar detector is not sensitive to gamma-radiation, an external gamma-ray calorimeter is therefore necessary.

Due to the high velocities of the reaction products in some inverse kinematics measurements, the emission of the gamma-rays by these products are subjected to Doppler shifts. In order to overcome the limitations imposed by Doppler broadening to a tolerable level, a highly granular calorimeter is required. The CALIFA detector, which is composed of thousands of inorganic scintillators, provides the necessary angular resolution to reconstruct the gamma-ray energy in the projectile rest-frame.

The use of an active-target in combination with gamma spectroscopy allows for the first time to perform $(\alpha,\alpha'\gamma)$ coincidence experiments on exotic nuclei in inverse kinematics. The CALIFA spectrometer at the R^3B setup will provide the necessary granularity, efficiency and resolution to investigate resonant reactions at low energies with this isoscalar probe.

The number of readout channels of nowadays detector systems is much higher then their precedents. Usually the number of channels of the detector systems constrains the minimal requirements for a Data AcQuisition (DAQ) system and the total price of the readout system. The DAQ system

[5]Petersburg Nuclear Physics Institute, Gatchina, Russia. http://www.pnpi.spb.ru/

should fulfil a number of strict requirements: low power consumption, compactness, the ability to record at high-rates several hundreds of channels and affordability. Modern experiments tend to migrate from analogue to fully digital and distributed systems, which allows for a more dynamic and comprehensive interaction between the user and the system. The speed and the availability of a new generation of high performance ADCs together with nowadays fast programmable digital electronics are the motivation to replace the analogue circuitry of the acquisition electronics with programmable digital systems.

In order for the detectors to perform at best certain conditions have usually to be met. For instance, Avalanche Photo-Diode (APD) photosensors used in CALIFA to readout the scintillation light output of the CsI(Tl) crystals are extremely temperature dependent devices, which require an active gain compensation or temperature stabilisation. One of the solutions to improve the performance of these detectors consists in exploiting the advantages of fully digital data acquisitions systems and the fact that the signals information is preserved for extensive feature extraction. Investigation shows that there are indeed information on the pulses from CsI(Tl) scintillators that, in principle, can be used for the purpose of particle discrimination and temperature gain dependent compensation.

1.2 Sampling — differences to analogue analysis

During the last decade, the development of fast sampling Analogue to Digital Converters (ADCs) with good resolution has made the digital processing of pulses from detectors possible. Many data acquisition systems now incorporate digital processing in place of the traditional analogue approach, which in some circumstances are proven to have significant advantages over analogue systems. Normally, read-out systems are much more compact as all the information from the pulses can be extracted from the digitised data either in offline analysis or already inside the sampling ADC.

The use of a sampling ADC with sufficient high speed and resolution allows to preserve all the information contained in a single analogue signal from the detector or preamplifier by taking multiple measurements of the pulse amplitude along the pulse duration and converting these samples into a data sequence of digital values. Depending on the pulse length, many samples are required during the interaction time of radiation in the detector in order to capture the full shape information. The pulse shape characteristics are therefore carried out in a string of digital values that can then be stored and manipulated using standard digital operations, such as multiplication, addition et cetera. The combination of these operations can be used to elaborate more complex shape transformations, including for instance, emulation of the standard shaping steps of integration and differentiation used to produce pulse shapes similar to those proven to be useful in analogue shaping. These digital shapers produce the same results as the equivalent analogue process.

Since the digital operations are carried out by software or firmware routines, digital signal processing allows for an unlimited choice of input parameters that can take on arbitrary values. Besides that, these parameters can be self-adjusted to adapt to changing conditions, e.g. discrimination threshold levels can be automatically adjusted with respect to the amount of (parallel) noise. The flexibility of the system is another advantage that can be exploited after investigating the properties of the pulse. By studying their shapes, new algorithms can be programmed to extract useful

information. In conventional electronics, changing parameters such as shaping times or trigger thresholds often require switching physical circuit components or adjusting potentiometers which are limited to a predetermined range of choices and require to repeat the measurement with the new set of parameters. Furthermore, there is a number of shaping approaches that are not feasible for analogue systems, such as removing the shaping effect of the preamplifier (deconvolution), trapezoidal shaping or averaging of multiple pulses (Section 2.4.1).

Another advantage of the digital approach is stability. Once the signal is converted into digital data, the information is no further changed and subsequent transport and treatment becomes immune to distortions caused by electronic noise and temperature instabilities. Digital manipulations will introduce no further noise into the system and behave perfectly linear. One disadvantage may arise when measuring the pulse arrival time. The discrete nature of digital signals limits timing accuracy to the nearest period of the sampling rate. Although some more complex techniques can be applied to improve accuracy, analogue timing methods often yield better timing information when fast detectors are involved.

This thesis deals with the development, implementation and test of digital signal processing algorithms for CsI(Tl) scintillation detectors (employing the CsI(Tl) crystals produced for the CALIFA prototype) and for the AcTar ionising chamber equipped with digital electronics. In Chapter 2 the digital pulse shape analysis algorithms suitable for the two detector concepts are presented. These methods deal with processing and transformation of digital signals. The aim is firstly to improve extraction of time and energy information from digitised raw signals, and later extract more complex information required in more modern experiments. Given the intrinsic distinction between scintillation detectors and ionising chambers, the experimental studies of the CsI(Tl) and the AcTar detectors are addressed in different chapters.

In Chapter 3 the methods presented in the previous chapter are implemented and tested exploiting the signal's pulse shape characteristics of the CsI(Tl) scintillation detector. The aim is to improve energy and timing measurements as well as perform more refined tasks such as the compensation for the temperature gain dependency of the CsI(Tl) detector system and particle identification. The proposed method to correct the temperature gain dependence of the detector allows conserving a good energy resolution in a temperature varying environment with no need for measuring the detector temperature externally. The particle identification approach is intended to identify the pulse shape of different particle species in an unsupervised and automatic way. Although these methods are of special interest for R^3B calorimeter, they are not only restricted to this purpose. Many other applications employing CsI(Tl) based gamma-ray detectors, that may be subjected to temperature variations, e.g. homeland security and background field radiation monitoring, can also benefit of these techniques to improve their performance. Thus, the present study covers both, the use of Photomultiplier Tube (PMT) and APD, as readout photosensors of the crystals scintillation.

Chapter 4 presents the functionality tests of the AcTar prototype for the R^3B setup. The objective is to test the feasibility and performance of such kind of detector with the use of a heavy ion beam. As a proof of concept, a ^{58}Ni beam at 700 MeV/u was impinging on a He-H_2 (3%) gaseous target mixture. Similarly to the scintillation detector, all the useful information, e.g. energy and scattering angle, was extracted in post-processing analysis of the digitised signals.

Chapter 2

Methods in digital signal analysis

Digital Signal Analysis (DSA) includes methods for dealing with transformations of digital signals and information extraction. This transformation process begins in the detectors and ends with the formatted data. The main objective of Digital Signal Processing (DSP) is to remove the unwanted information (baseline fluctuations, noise etc.) from the signal pulses and extract relevant information from it. This chapter addresses the algorithms used to extract information from sampled signal pulses provided by radiation detectors and evaluate means to classify their shapes. The radiation detectors are used for nuclear spectroscopy applications, therefore a determination of relevant quantities includes, e.g. the accurate measurement of the energy deposited in the detector, the time of arrival or the shape of the pulse.

2.1 Introduction

The fundamental output of a pulse type radiation detector is a burst of charge Q freed by a single radiation quantum (photon or particle) interacting within the detector active volume. While for some detectors, such as ionisation chambers, the Q results from sensing the direct ionisation created by the passage of radiation, for others such as scintillation detectors the energy of the radiation quantum deposited in the scintillator is first converted into a detectable light and then converted into Q by a photosensor. The charge Q is proportional to the energy deposited and is delivered as a transient current pulse, where Q is the time integral of the current pulse. With the continuous exposure to a source of radiation, the output of the detector is a series of these transient current pulses, occurring at random times and usually with differing duration and amplitudes.

The first step in the digital pulse processing chain is the signal digitisation. The complete signal waveform is acquired upon a trigger condition using a sampling Analogue to Digital Converter (ADC). The required time, energy and shape information is then extracted from the sampled and quantified signal by means of post-processing algorithms. The analogue waveform must be sampled at sufficiently high sampling rate in order to retain its fundamental properties: Shape, Q, amplitude

and time. All signal processing operations are done in the digital domain and are implemented in software which provides more flexibility in comparison to the analogue approach.

During post processing the large amount of stored raw signal data is reduced to only a few parameters classifying the pulse, such as time, energy and shape. For this work the numerical analysis of the pulse shape has been performed offline on the stored data. The used algorithms were implemented and tested using the high-level programming language C++ and the ROOT framework [13]. Although the computational resources are not of utmost relevance for offline analysis, when possible the DSA algorithms were chosen taking into account their performance.

The methods presented were chosen aiming to be used for digital signal analysis of the sampled signals from two different radiation detector systems, a CsI(Tl) scintillation detector (Chapter 3) and an active-target ionisation detector (Chapter 4). However, the presented methods are generic to a large extent and can thus be also applied to other types of detectors.

With the intention to expose the effects of the different methods in a clearer way, the data signals presented in this chapter are artificial and were simulated to have ideal features.

2.1.1 Sampling ADC — Principles of operation

Sampling ADC transform an incoming analogue signal to a binary number and then eventually to a digital data value for storage or monitoring. Since it involves quantisation of the signal in time and amplitude, this process inevitably induces errors to the system. The principle of how a sampling ADC works can be subdivided into three main phases: sampling, quantisation and encoding.

The time-continuous input signal is first sampled by a sample-and-hold (S/H) circuit and transformed into a discrete time signal by holding the signal for a period defined by the sampling frequency. The lower constraint for the sampling frequency is usually determined according to the Nyquist-Shannon sampling theorem [14, 15], which states that as long as the sampling frequency is at least twice the highest frequency component of the input analogue signal, it allows a full reconstruction of the initial signal waveform from the sampled data without the introduction of aliasing.

During quantisation, due to limited ADC resolution the input signal in quantised in discrete steps. The resolution is specified by the number of N bits that an ADC can handle and is usually defined with respect to the full-range reading V_{max} of the ADC. Therefore the smallest signal step $V_{LSB} = V_{max}/2^N$ determines how precise the pulse amplitude can be resolved, which directly contributes to the achievable energy resolution. Since the digital value is only an approximation of the true value of the analogue amplitude at a particular instant, it introduces irreversible quantisation errors which prevent an exact reconstruction. The maximum quantisation error e_q is obtained as $|e_q| \leqslant V_{LSB}/2$. A common assumption is that the quantisation error affects a signal processing system in a similar manner to that of additive white noise, and thus having negligible correlation with the signal [16]. Additionally, because the ADC sampling rate also introduces quantisation in time and is not correlated with the random detector pulses, the pulses are sampled with varying time offsets with respect to the ADC clock phase.

As the last step the output is encoded. The string of unary codes (outputs of the quantisation block) are normally first encoded into Grey codes to suppress sparkle code and metastability, and then converted into binary words [17].

2.1.2 Information contained in detector signals

When choosing to record the digital waveform of a detector signal the full pulse shape information is available to analyse and can be repeatedly accessed. This is very convenient since accessing this information often requires applying transformations to the pulse shape. The most important information contained in the detector signals is in many cases the energy deposited in the detector and the time of the event occurrence.

With modern high resolution ADCs some detector systems do not require further amplification before digitisation, the output pulse induced by a particle interaction in the detector medium can be directly measured. However, for some detector systems the current is too small to be measured directly. The current pulse is first preamplified to improve signal to noise ration before digitisation. The preamplifier frequently has a charge sensitive configuration, which integrates the transient current pulse to produce a signal with amplitude proportional to the total charge Q.

After digitisation by the ADC, the sampled signals (a.k.a. raw signals) contain undesired information such as baseline fluctuations, noise or pile-up which difficult signal analysis. In order to access the relevant information, the signal often require preparation by filtering the noise and transforming their pulse shape before further information processing. The filtering and shaping approaches addressed in the present work are explained in Section 2.2.

In case that the signal is sampled right after the detector, the energy is extracted integrating in time the current pulse above the baseline (assuming a positive polarity of the pulse). Ideally, the pulse would be integrated in its full extent since the energy resolution tend to improve when more charge is collected. If the signal is sampled after the charge sensitive preamplifier the energy information is conveyed by the maximum amplitude of the digitised signal. This maximum amplitude is usually underestimated due to the so called ballistic deficit effect [18], which limits the achievable energy resolution. The ballistic deficit can be compensated using a Moving Window Deconvolution (MWD) algorithm to restore the signal's original amplitude (see Section 2.2.5). The extracted value of the energy deposited in the detector will further be referred in this document as the calorimetric value of digitised signal.

In digitised signals the pulse time information is intrinsically carried by any sample in which its position relatively to the pulse shape is well known. Because the signal has often noise that limits measuring the exact start time, i.e. the sample index that determines the pulse start, this time is obtained in reference to the pulse leading edge. Assuming that the pulse rise time does not change, better timing can be extracted by locating the sample index for which the signal equals a constant fraction of its maximum amplitude. Detailed information on these approaches used for time extraction can be found in Section 2.3.

In addition to the energy (more precisely pulse height or pulse area) and timing information, the signal from some detectors also carry information in their shapes. In particular for scintillation detectors, the excitation mechanisms and time constants of the consequent fluorescent decay induced by the incident ionising radiation in the detection medium are reflected by the pulse shape of the detector signal. These excitation mechanisms are often affected by factors such as temperature and type of the ionising particle, which, depending on the characteristics of detection medium may be more or less pronounced. A similar effect may be found in ionisation detectors. Particles of different ionisation power produce shorter or longer ionisation trails in the detector volume, also particles

with different incident angles have a different projection of their ionisation trails in the detector anode. Both of these situations result in different charge collection times and hence different pulse shapes at the detector output. With an appropriate technique of pulse shape discrimination one can take advantage of this property to allow a distinction or quantisation of the factors that influence the pulse changes. The pulse shape discrimination algorithms used to classify different pulse shapes are explained in detail in Section 2.4.

2.2 Filtering and Shaping

As mentioned in the previous Section, digitised signal pulses from radiation detectors provide a variety of information of the detected radiation. However, the raw[1] signals need to be further processed to extract this information. There are a number of filtering and shaping methods with varying performances which can be applied to signal pulses in order to improve processing the pulses information.

In signal processing, digital filters are systems that perform mathematical operations on the sampled signals to reduce or enhance certain aspects of these signals. For instance, filters can be designed to perform tasks such as reducing noise (smoothing) to improve signal-to-noise ratio or changing the pulses shape such as integrating and differentiating. Reducing the noise improves the signal's timing and amplitude evaluation. Integrating the signal allows to calculate the area of the signal under determined regions and evaluate the signal's calorimetric value. Differential filters allow to calculate the slope of the signals edges and improve pile-up detection which based on this make a decision as to the acceptability of the event.

This Section presents the detailed information of five shaping filters further employed in the present work to process the digital signals. These filters consist of: two integrator/low-pass filters, a Moving Average (MA) filter and a Moving Binomial (MB) filter; two differentiator filters, a Moving Gradient (MG) filter and a Bipolar Moving Average (BMA) filter; and a MWD filter. All filters have a Finite Impulse Response (FIR), meaning that any input has zero effect after a finite time and, with the exception of the MWD filter, are computed as a discrete-time convolution applied to the signals data stream, which can simply be implemented as moving window filters.

2.2.1 Moving Average filter

The MA filter [19] is a simple FIR filter, most commonly used in digital signal processing for smoothing sampled data/signals. It is one of the easiest digital filters to understand and implement. In spite of its simplicity, the moving average filter is an effective low-pass filter for noise reduction while keeping the sharp step response. As the name suggests the moving average filter operates by averaging a number of points from the input signal to produce a single point in the output signal. This procedure is expressed by the following expression:

$$\mathrm{box}_N(k) = \begin{cases} 1/N & \text{if } k \in [0, N[\\ 0 & \text{otherwise} \end{cases}, \tag{2.1}$$

[1] Output signals from the digitiser

$$MA_N[k] = (S * box_N)[k]$$
$$= \frac{1}{N} \sum_{n=k-N}^{k} S(n). \tag{2.2}$$

The $MA[k]$ output sequence is the result of the convolution between input sequence $S[k]$ and the filter's impulse response, which is given by the coefficients of the box kernel, i.e. a sequence of coefficients with constant weight. The parameter N determines the width of the MA filter equal to the number of signal samples in the average. Depending on the value of N the standard deviation of the averaged signal can be reduced by a factor of $1/\sqrt{N}$ compared to the original signal [20].

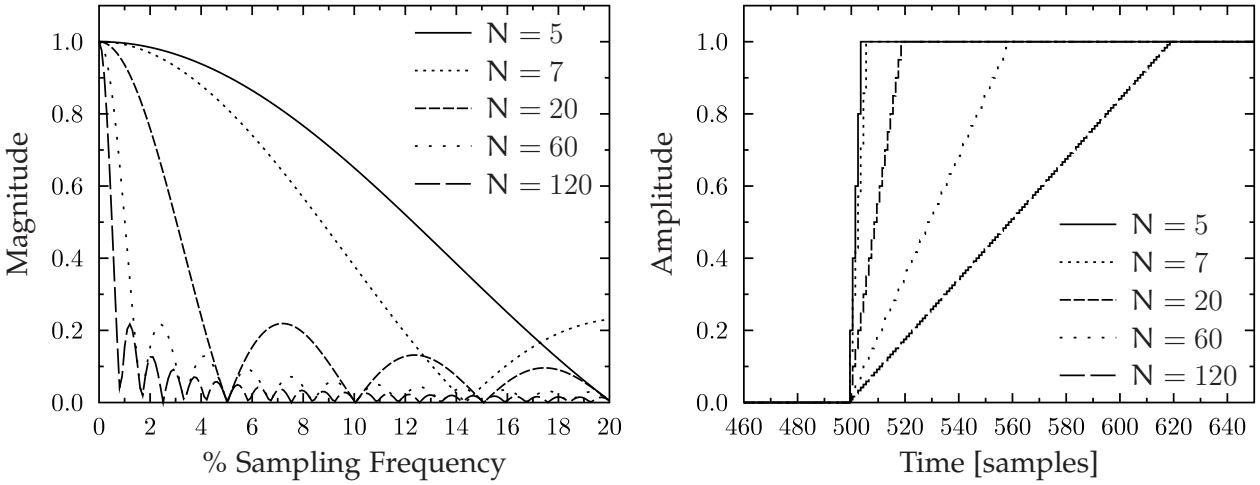

Figure 2.1: Transfer function (left frame) and step response (right) of the MA filter for five different filter lengths N. For a increasing filter length N the higher frequency components of the signal are strongly suppressed suggesting the low-pass behaviour of the filter.

Figure 2.1 illustrates the transfer function (left frame) and step response function (right frame) of the moving average filter for 5 different lengths. The transfer function is determined from the Fourier transformation of the filter coefficients. The transfer function of the MA filter shows an oscillating behaviour indicating that the attenuation does not constantly increase with the frequency. However, if the signal power is concentrated mainly in the lower frequency range, the MA is a preferred smoothing filter because of its simple structure. The moving average filter can also be expressed as a recursive filter, which improves substantially the speed performance of the filter. Since the coefficients weight does not change, it can simply be implemented by adding the newest weighted sampling point and subtracting the N-th entry from the previous sum:

$$MA_N[k] = MA_N[k-1] + \frac{1}{N}(S[k] - S[k-N]). \tag{2.3}$$

Besides smoothing of the signal noise, the moving average filter can be interpreted as a "moving integrating filter". The output of the MA filter is indeed the normalised integration of the input signal inside the filter window. If the width N of the filter window is set to a time scale characteristic of the length of the pulse to be integrated, the amplitude of the output signal $MA[k]$ is proportional[2]

[2]The constant of proportionality is the filter order N. A real integration is obtained by setting coefficients of the box kernel to unity.

to the integral area of the input signal S[k] under the later N samples. Therefore, the MA filter can be used to extract calorimetric information of the digitised current signals in a integrating time window $t = N \cdot f_s$ characterised by the filter width.

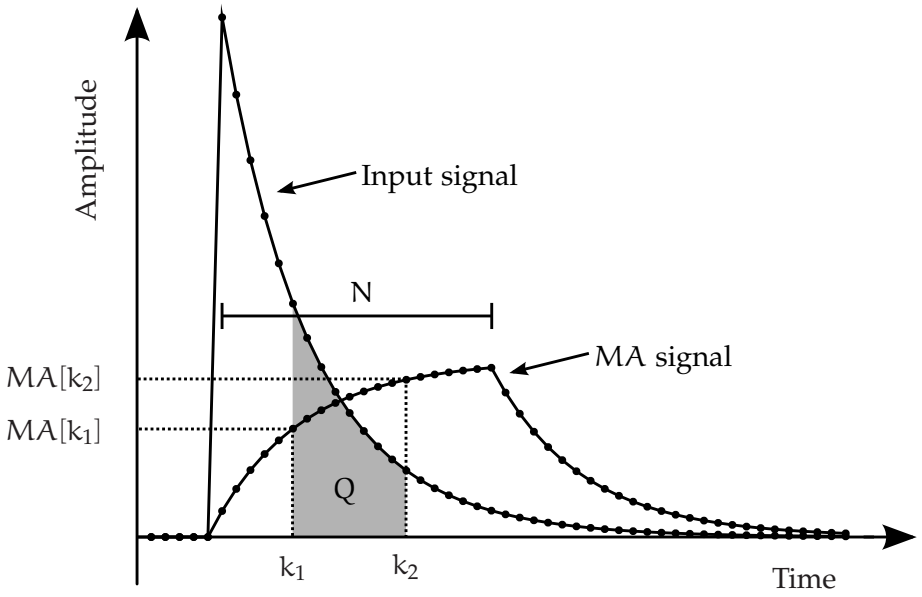

Figure 2.2: Concept of MA filter for determining the pulse integral in a defined region. The value of the area Q defines the integral of input signal from k_1 to k_2. The peak amplitude of the MA signal is equivalent to the maximum pulse integration inside window N.

Figure 2.2 illustrates the principles of the MA filter in calculating the integral of a representative exponential input signal. The peak amplitude of the MA is the integral of the input signal inside the window N. Since the integration occurs during the MA rise time, the amplitude difference between two sampling points k_1 and k_2 can be used to calculate the integral of a fractional pulse region Q of the input signal S[k]:

$$Q = \sum_{n=k_1}^{k_2} S[n] = (MA_N[k_2] - MA_N[k_1])\, N, \quad with \quad k_2 - k_1 < N. \tag{2.4}$$

2.2.2 Moving Binomial filter

The MB is another low-pass FIR filter. It is part of the family of Gaussian filters and is performed here using the method developed by Marchand and Marmet [21]. This filter is used for smoothing the signal removing high frequency noise and high frequency spikes within the signal. The binomial smoothing algorithm has following properties: (1) zero phase shift at all frequencies, (2) the sequence of smoothing coefficients b_k does not introduce undesired side effects such as multiple peaks when only one is present in the original data, (3) the transfer function is never greater than one in order to avoid enhancing some frequency components disproportionately, (4) the transfer function is always positive and never contains phase reversals. The moving binomial filter convolutes the input signals S[k] with a smoothing sequence of normalised coefficients b_n derived from the Pascal's triangle at a row level equal to $2N_p + 1$, defined as:

$$b_n = \binom{2N_p}{N_p + n} \Big/ 4^{N_p}, \tag{2.5}$$

where b_n is the binomial coefficient, $b_{-n} = b_n$, N_p is any positive integer characterising the filter order and n is a positive integer increment [21]. The filter computation is performed by using convoluted expression. The output filtered signal $MB[k]$ is given by:

$$MB_{N_p}[k] = \sum_{n=-N_p}^{N_p} b_n S[k-n], \tag{2.6}$$

The order N_p of the filter must be chosen to obtain the desired cutoff half-transition frequency $f_{1/2}$ defined as follows

$$f_{1/2} = (f_s/2) \cdot (2/\pi) \cdot \cos^{-1}(0.5^{1/2N_p}) \tag{2.7}$$

where f_s is the sampling frequency of the flash ADC.

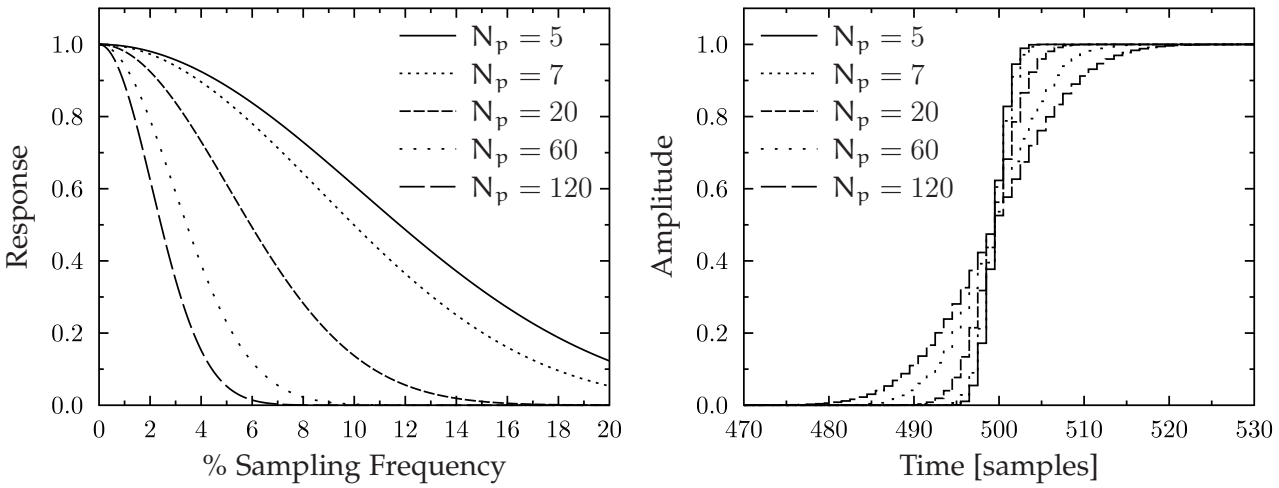

Figure 2.3: Transfer function (left) and step response (right) of the moving binomial filter for five different filter orders N_p. The transfer function of the binomial filter show no oscillation behaviour, contrary to what is observed in the MA filter.

The figure 2.3 illustrates the transfer function (left frame) and step response (right frame) of the moving binomial filter for 5 different orders. The transfer function is determined from the Fourier transformation of the binomial coefficients. Contrary to the MA filter, the binomial filter shows no oscillating behaviour in the transference function and is therefore a better low-pass filter than the MA filter. Also the sharpness of step response is less sacrificed by the binomial filter for identical cutoff frequencies. However, the filter is more demanding for computational resources than the MA filter. The MB coefficients have to be stored and the filter requires multiplications with fractional precision.

2.2.3 Moving Gradient filter

The MG filter is the first order derivative of the input signal. This filter returns the rate of change of the pulse amplitude over time, which is interpreted as the slope or tangent of the signal at each

sampling point. The fundamental problem is that according to its mathematical definition, a derivative can only be performed with continuous functions while the input signal is a discrete function of integer temporal coordinates. As a result the MG filter can only be seen as an approximation of the true derivative of the continuous detector signal. Furthermore, taking a derivative emphasises the high frequency noise present in the signal. The general solution involves combining the derivative operation with smoothing techniques.

A more robust derivative approach against the presence of noise in the input signal is therefore adopted in implementing the MG filter. It consists in taking a number of sampling points N_p before and after a given sample index k in the input signal. An approximate value of derivative at the sample index k is then calculated by averaging all slopes connecting every pair combination of $2N_p + 1$ sampling points in the interval $[k - N_p, k + N_p]$. In order to implement this method, the MG filter is computed using the odd convolution kernel defined by the normalised coefficients d_n, calculated as follows:

$$d_n = \begin{cases} \sum_{j=1-n}^{n} \frac{1}{j+N_p} \Big/ \binom{2N_p+1}{2} & \text{if } n > 0 \\ 0 & \text{if } n = 0 \\ -d_n & \text{if } n < 0 \end{cases}, \tag{2.8}$$

where N_p characterises the magnitude of the MG filter and $\binom{2N_p+1}{2}$ is the number of all pair combinations in the $2N_p + 1$ range. The output of the MG filter at the sample index k is given by the expression:

$$MG_{N_p}[k] = \sum_{n=-N_p}^{N_p} d_n S[k-n], \tag{2.9}$$

In defining the coefficients d_n in such manner, more weight is given to the samples which are further from the k-th sample. The same way, noise has gradually less impact in determining the true derivative at that point.

Figure 2.4 exemplifies the output waveform in the MG filter applied to a Gaussian-shaped input signal with no noise. The maximum slope of the input signal leading edge and respective sample point in which this maximum is reached can be measured by detecting the peak amplitude $MG[k_{max}]$ and position k_{max} of the first derivative signal during rise time. Analogous, the minimum slope and respective sample index of the input signal trailing edge can be measured by detecting the minimum $MG[k_{min}]$ and position k_{min} of the first derivative signal during the fall time. This method is useful to extrapolate the virtual points that define the beginning and end of the pulse identically to the way rise-point timing is obtained in Section 2.3.5.

2.2.4 Bipolar Moving Average filter

The BMA filter is a FIR filter that transforms a unipolar input signal into a bipolar and smoothed output signal. This filter is the box version of the first derivative, it produces similar results to the moving gradient filter MG in transforming the input signal, with the difference that the kernel coefficients have equal weight. The BMA method is therefore much simpler to implement and a faster filter from the computational point of view.

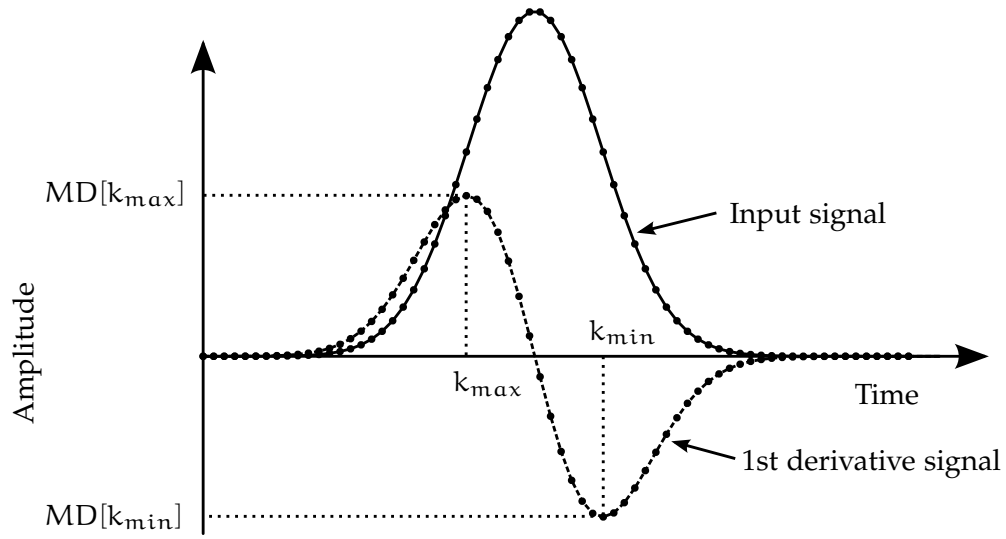

Figure 2.4: Waveforms in the moving derivative filter. The amplitude of the MG represents the evolution of the input signal. The local maximum of $MG[k_{max}]$during the input signal rise time returns the maximum slope of the leading edge, while k_{max} is the time index when the maximum slope is reached. Analogous, $MG[k_{min}]$ is the minimum slope of the signal fall edge occurring at the time index k_{min}.

The BMA filter is computed by convoluting the input data stream $S[k]$ with a bipolar box kernel (bibox):

$$\mathrm{bibox}_{W_b}[k] = \begin{cases} -1 & \text{if } k \in]-W_b, 0] \\ 1 & \text{if } k \in]0, W_b] \\ 0 & \text{otherwise} \end{cases}, \tag{2.10}$$

where W_b is both the width of the negative and positive part of the bibox kernel which characterises the magnitude of the filter. The $BMA[k]$ convoluted expression takes then the form:

$$\begin{aligned} BMA_{W_b}[k] &= (S * \mathrm{bibox}_{W_b})[k] \\ &= \sum_{n=k-2W_b}^{k-W_b} S[n] - \sum_{n=k-W_b}^{k} S[n]. \end{aligned} \tag{2.11}$$

The BMA output results in an averaged differentiation of the input signal. However, no quantitative information of the signal slope can be extracted, unless further normalisation is applied. Thus, the first derivative equivalent of the BMA filter can be calculated from:

$$BMA'_{W_b}[k] = \frac{BMA_{W_b}[k]}{W_b^2}. \tag{2.12}$$

Since the bibox is symmetric in polarity, the current baseline value is added and subtracted an equal number of times. Therefore, the BMA method is not affected by the baseline dynamics as long as the baseline fluctuations occur at a larger scale compared to the size of the bibox kernel W_b.

The sensitivity of BMA filter to the slope changes of the input signal makes it well suited for pile-up detection when performing trigger decision (2.3.2). The output waveform of the BMA filter, as

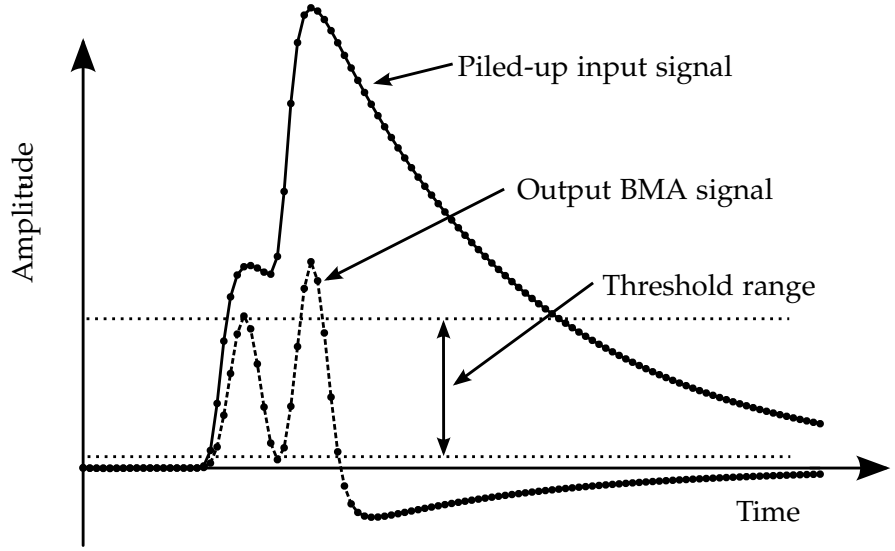

Figure 2.5: Waveforms in the bipolar moving average filter. The two piled-up pulses were delayed by 9 sampling points from each other. The lower dashed line is the smallest threshold value for which the two pulses will be detected, while the upper dashed line is the largest value for which the two pulses will be detected.

response to representative pile-up signal with no noise is illustrated in Figure 2.5. The occurrence of pile-up is detected by measuring a second peak in the BMA signal above a defined trigger threshold within a hold-off time window characteristic of the pulse length required for further analysis. It can be observed in Figure 2.5 that there is a range of thresholds for which pile-up events can be successfully discriminated. The upper limit for the threshold is the amplitude of the first peak while the lower limit is the dip between the two peaks.

In principle the trigger threshold is based on the magnitude of the noise level and, in order to not sacrifice the minimum detectable energy, the value of this threshold is usually set to a low value in the amplitude spectrum. The dip between the two pulses in the BMA waveform is affected by the relative amplitude between the pulses, the pulse rise time, the delay between the pulses and the magnitude W_b of the filter. Consequently, for the defined magnitude W_b there is a minimal delay between the pulses where the two peaks can be detected. Assuming a constant peaking time of the pulses, i.e. the time that a pulse needs to reach maximum amplitude, a fairly good approximation for the lower limit of delay can be obtained by satisfying the following inequality:

$$t_{peaking} + W_b \cdot T_s \leqslant t_{delay} \tag{2.13}$$

where $t_{peaking}$ and t_{delay} are respectively the peaking time and delay of the pulses and T_s is the sampling period. The fraction of events which are potentially distorted by pile-up can be estimated based on the delay information and on the trigger rate. If the arrival of pulses are independent and random events, then their time arrival obeys the Poisson statistics and the probability of N event occurrences in a time interval t is given by [22]:

$$P(N) = \frac{(\lambda t)^N e^{\lambda t}}{N!}, \tag{2.14}$$

where λ is the expected average event rate. Consequently, the probability of misidentifying a piled-up event takes the form:

$$P' = 1 - P(0) = 1 - e^{\lambda t}. \tag{2.15}$$

For example, to ensure less then 1% of undetected piled-up events the detector has to operate at a count rate below $\lambda < -\ln(0.99)/t$, with $t = W_b T_s$. For instance, if the BMA trigger is able to recognise events with arrival time difference $t \geqslant 500$ ns, less than 1% of undetected piled-up events are expected if the detector is operated at a rate below 20 kHz.

The graphical representation of the kernel functions of the four previous filters presented in this Section are graphically represented in Figure 2.6. Since this filters have finite impulse response (FIR filters), the kernel functions correspond to the their impulse response functions. The output of each filter is computed by convoluting the signals data stream with the respective kernel function.

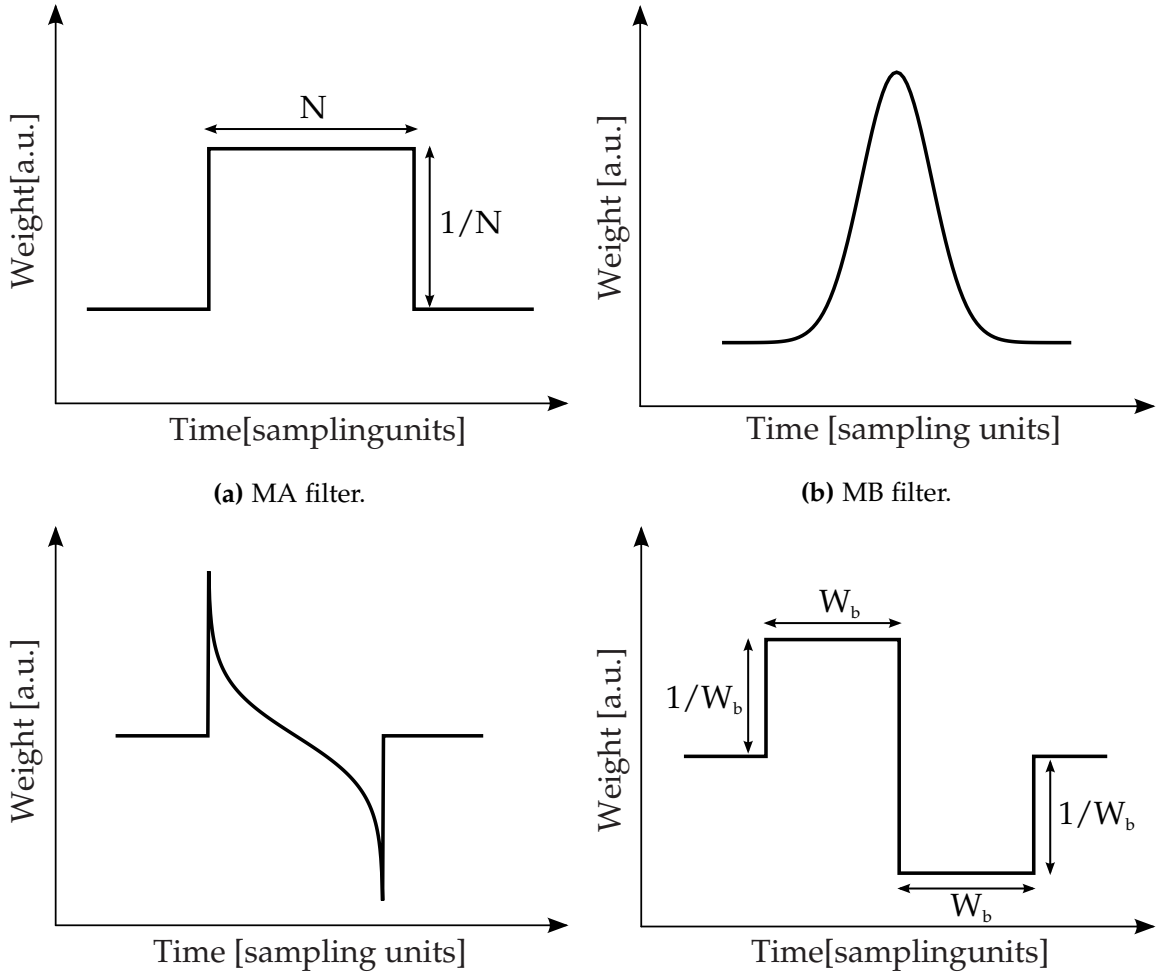

(a) MA filter.

(b) MB filter.

(c) MG filter.

(d) BMA filter.

Figure 2.6: Schematic representation of the kernel functions of the filters used in the presented work.

2.2.5 Moving Window Deconvolution

The MWD [23, 24] is an algorithm to extract the energy of digitised charge signals featuring an exponential decay. The basic motivation for the MWD is to convert the signal's exponential decay into a flat top signal containing the total amount of charge induced in the detector within a defined time window and to reduce the signal width.

The output signal from a charge sensitive preamplifier[3] results from the convolution of the charge distribution function of the detector wit the impulse response function of the preamplifier[4] (see Section 3.2.4). This signal has the shape of a fast rising step followed by a slow exponential decay characteristic of the continuous discharge of the preamp feedback loop[5]. The fast rise time is caused by the charge collection and reaches a maximum amplitude at the end of the charge collection process. For the case of a scintillator detector the charge collection time corresponds to the scintillation time, since the scintillation photons are converted into a charge current by the photosensor. The energy information is therefore carried by the amplitude of the preamp signal. However, because the rise-time is not infinitely short, the exponential decay reduces the final peak height depending on the signal rise time. A synthetic representation of the preamp signal $S[k]$ is illustrated in Figure 2.7. The gap between $S[k]$ peak and total charge U_0 differs depending on the charge collection process giving rise to different ballistic deficits [18].

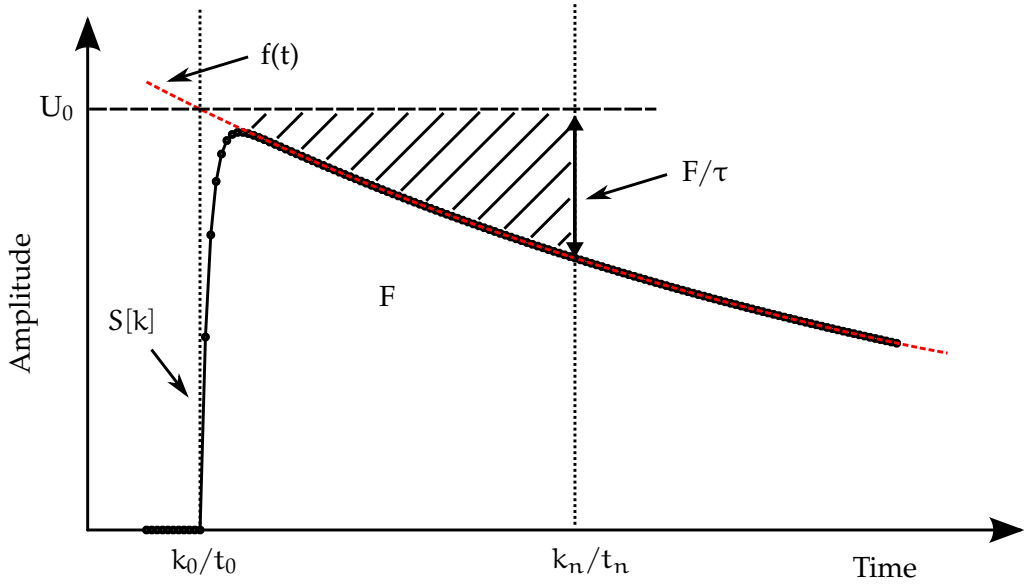

Figure 2.7: Principles of the MWD algorithm.The function $f(t)$ is a single exponential decay fitting the trailing edge of the preamplifier signal. The amplitude decrease of $f(t)$ after a time $t = t_1 - t_0$ is given by F/τ, where F is the integral of $f(t)$ from t_0 to t_1 and τ is $f(t)$ decay constant. The difference between the peak amplitude of the preamplifier signal $S[k]$ and U_0 determines the ballistic deficit.

[3]Such preamplifiers are used in the Avalanche Photo-Diode (APD) readout systems.

[4]The response function of a charge sensitive preamplifier can be well approximated by a single pole function, which corresponds to a single exponential decay, $h(t) = e^{\frac{-t}{\tau}}$

[5]The feedback of a charge sensitive preamplifier is normally equivalent to an RC circuit, i.e. a parallel circuit of a resistor and a capacitor.

One advantage of using MWD is the reconstruction of ballistic deficits, especially when detectors with slow signal rise time are involved. The reconstruction of the signal initial peak amplitude allows to improve energy resolution. A detailed discussion of the MWD algorithm can be found in [25]. Assuming that the preamplifier features a single exponential decay, by knowing the decay time and the start time of the signal, the initial amplitude can be calculated from any sample point of the decaying signal. Starting with an expression for a single exponential decay fitting the preamplifier signal beginning at $t = t_0 = k_0 T_s$ (see Figure 2.7)

$$f(t) = U_0 \cdot \exp\left(\frac{t_0 - t}{\tau}\right), \tag{2.16}$$

where τ is the decay constant and U_0 the initial amplitude at t_0. If t_0 and $f(t_0)$ are known, the value of U_0 can be derived from

$$\begin{aligned} U_0 &= f(t_n) + U_0 - f(t_n), \\ U_0 &= f(t_n) + U_0 \cdot \left(1 - \exp\left(\frac{t_0 - t_n}{\tau}\right)\right), \\ U_0 &= f(t_n) + \frac{1}{\tau}\int_{t_0}^{t_n} f(t)dt. \end{aligned} \tag{2.17}$$

The deconvolution expression 2.17 can then be applied to the charge sensitive preamplifier signal $S[k]$ to remove the influence if its continuous discharge. Since $S[k]$ is in the digital domain, it is convenient to write the expression 2.17 in the discrete form

$$U[k] = S[k] + \frac{1}{\tau}\sum_{n=-\infty}^{k} S[n]. \tag{2.18}$$

The extension of the sum to $-\infty$ can be made because the amplitude of $S[k]$ is zero for $k < k_0$. The signal $U[k]$ has the shape of a infinite staircase signal in which the amplitude increases during the rise time of $S[k]$ and reaches a flat top after the charge collection process is completed.

The next step is to transform the staircase signal $U[k]$ into a more handy signal by setting its length to a finite value. The numerical differentiation of the discrete deconvolution expression 2.18 leads to the MWD expression

$$\begin{aligned} MWD_N[k] &= U[k] - U[k-N], \\ MWD_N[k] &= S[k] - S[k-N] + \frac{1}{\tau}\sum_{n=k-N}^{k-1} S(n). \end{aligned} \tag{2.19}$$

where N is the width of the moving window. The MWD method gathers as basic elements operations of differentiation and moving average. This constitutes a rather fast and intuitive method to compensate for the exponential decay.

In order to illustrate the output MWD waveforms for different ballistic deficits, the preamplifier signals were simulated by using [26]

$$S(t) = \begin{cases} \frac{S_0}{\tau_f - \tau_f}\left(\exp\left(\frac{t_0 - t}{\tau_f}\right) - \exp\left(\frac{t_0 - t}{\tau_r}\right)\right), & \text{if } t \geqslant t_0 \\ 0, & \text{if } t < t_0 \end{cases}, \tag{2.20}$$

where τ_r accounts for the rise-time of the signal, associated to the charge collection time (or scintillation time) and τ_d is the signal decay time constant characteristic of the preamplifier time response, in which $\tau_r << \tau_d$.

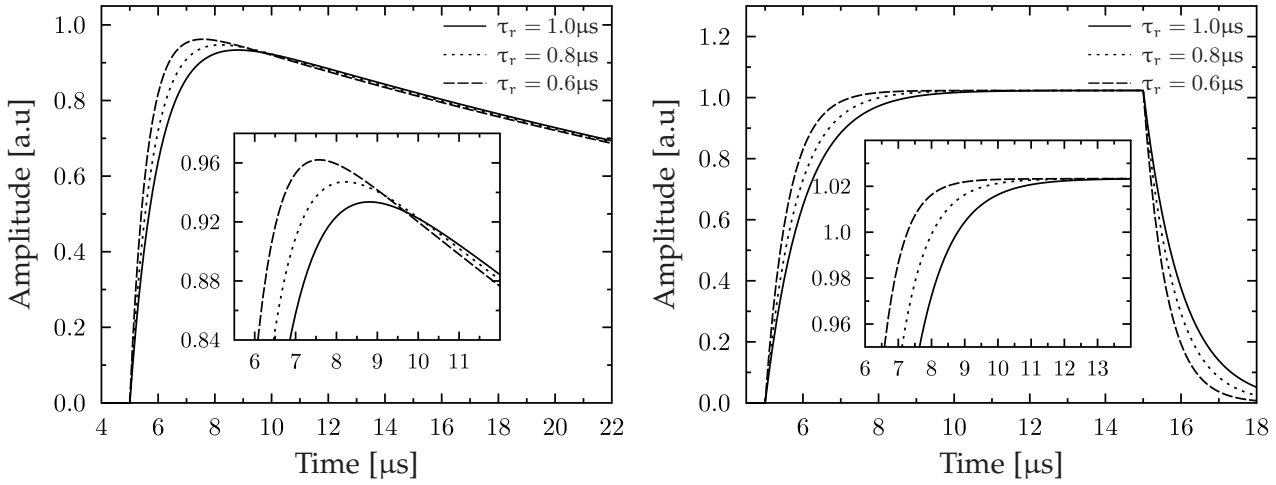

Figure 2.8: Waveforms in the MWD method. Simulation of three preamplifier signals with different rise time (left frame). The MWD step signal of each simulated signal (right frame).

Figure 2.8 shows the result of the MWD for three simulated signals with varying τ_r and constant $\tau_d = 40\mu$. It can be observed that independently of the rise time, all signals reach a common amplitude at the end of the flat top period of the MWD. It is important to notice that the MWD algorithm only deconvolutes the signal inside the window N. The value of N should be set to a value long enough to cover the signal rise time. By selecting a smaller N the processed signal shape never reaches a flat plateau and consequently the signal amplitude is not proportional to the deposited energy in the detector.

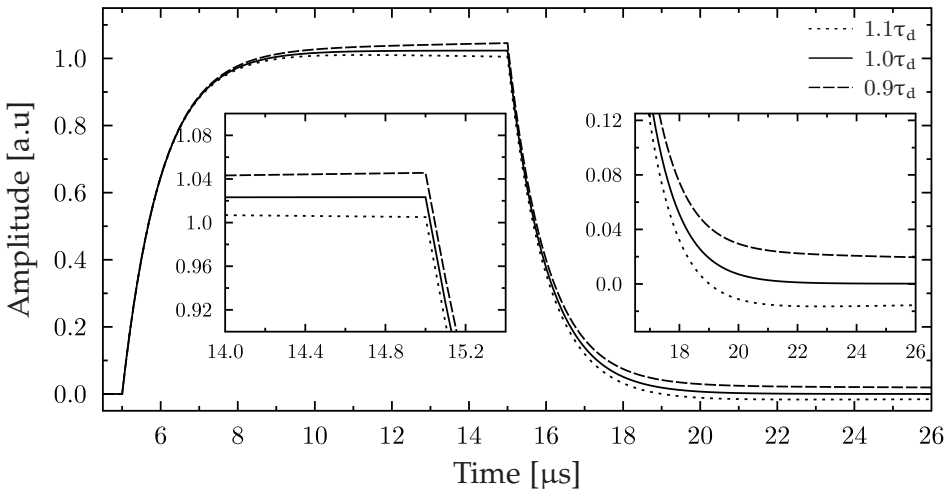

Figure 2.9: Variation in the MWD signal shape due to incorrect determination of the signal decay time τ_d. Different values of τ_d lead to different amplitudes at the end of the MWD. Also the baseline is different from its initial value afterwards.

Additionally, as mentioned before, the performance of the MWD algorithm relies on the correct knowledge of the decay constant τ_d. The effect of an incorrect determination of the decay constant τ_d in the shape of the MWD signal is shown in Figure 2.9. The underestimation of τ_d leads to a steadily increasing top of the MWD signal, while on the other hand an overestimation of τ_d leads to a steady decreasing top of the MWD signal. The baseline is also different afterwards, which consequently requires that the signal fully decays in order to the baseline recovers to its initial value.

2.3 Timing and triggering discrimination

The precise determination of the pulse arrival time is important for Pulse Shape Analysis (PSA), coincidence measurements and reconstruction of time correlated observables. In the active-target detector for instance, the angular scattering of the α-particles and the position of the reaction vertex is reconstructed by measuring the drift time of the electrons through the gas volume (Chapter 4). Therefore, the time between pulses across neighbouring anodes need to be well determined. Additionally, the evaluation of the Principal Pulse Shape (PPS) (Section 2.4.1) and performance of the pulse shape discrimination algorithms (Section 2.4) relies strongly on the good time alignment of the individual pulses.

A first time information may be already provided during the DAQ trigger decision. However, the resolution is not optimal due to the general uncertainty of the trigger decision and the limited ADC sampling rate. To achieve a more precise time reconstruction, the trigger thresholds have to be adjusted according to the pulse amplitude. Also, the information of multiple samples is normally used to interpolate the time information between sampling points. These approaches can be implemented using different methods.

2.3.1 Baseline correction

The baseline (i.e. zero value of the amplitude) is defined by the signal before the leading edge of the detector pulse. This baseline is expressed in ADC units and has an offset that usually changes for each event due to low frequency oscillations. Additionally, the baseline may show drifts or fluctuations due to temperature, noise pick ups or changes in the detector leakage current.

Many of the filters used for digital pulse processing require the baseline to have zero offset to produce optimal results. The baseline is then determined by averaging every input signal over the region immediately preceding the pulse leading edge. This region should be broad enough to yield a reliable mean value, but not too large to prevent including the tail of previous pulses. Because the signals are already trimmed during the recording process, the average region is usually set between the first sample and the pulse beginning. The resulting mean value is then subtracted from the full signal. Figure 2.10 illustrates a digitised signal waveform in units of ADC channels before baseline subtraction, where the shaded area represents the time interval for the reconstructed baseline to be subtracted from the signal amplitude.

With the signal from the active-target (featuring a Gaussian shape) the pulses often suffer down-pulling induced by the preamplifier after the trailing edge. In this case the baseline is also calculated

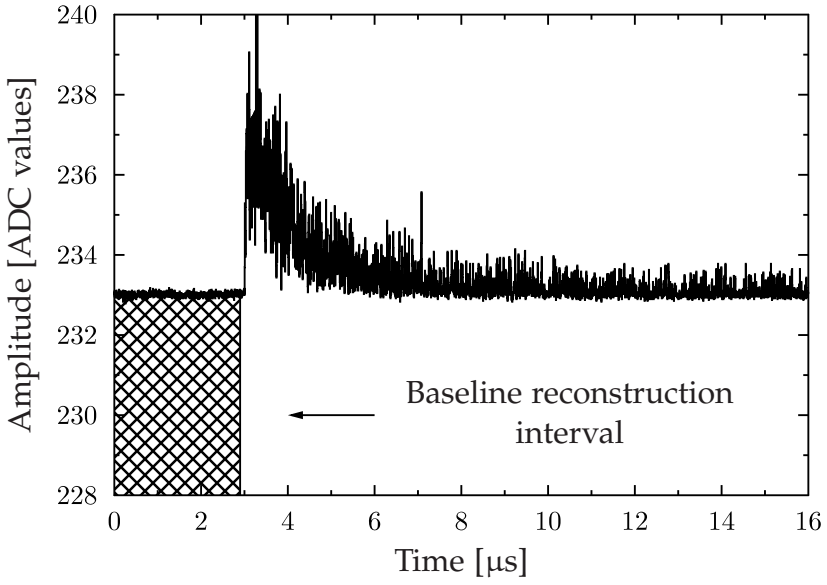

Figure 2.10: Reconstruction of the baseline. The shaded region represents the averaging interval preceding the pulse used to determine the baseline offset later to be subtracted from the signal amplitude.

after the pulse end. The mean value of the baseline calculated before and after the pulse defines the true signal baseline during the pulse integration for energy extraction.

2.3.2 Trigger decision

The first step of the digital signal processing chain is to discriminate the detector pulses from the background noise. This is normally achieved by comparing each sample from a digital data stream S[k] with a given trigger threshold. When the data value is bigger than the threshold level S_{thr}, the transition of the trigger output T[k] from $0 \rightarrow 1$ indicates that the current signal should be further processed, or otherwise discarded.

$$T[k] = \begin{cases} 0 & \text{if } S[k] \leqslant S_{thr} \\ 1 & \text{if } S[k] > S_{thr} \end{cases} . \tag{2.21}$$

Normally, a smoothing filter is applied to the data in combination with the triggering process to improve discrimination between signal and noise. Additionally, if a large rate of events is expected, the input data stream is often previously passed through a differential FIR filter in order to improve the discrimination of piled-up events (see Section 2.2.4).

Since the pulse amplitude is correlated to the energy of the detected particles, the level of the trigger threshold corresponds to a lower energy limit of the detected particles. In some applications it is desirable to set the trigger threshold to a level very close to the noise amplitude in order to prevent misidentifying of low energy events. In the active-target detector for instance, the energy of the recoil particles is collected across several anodes. Therefore, the energy resolution relies on the ability to detect small amounts of deposited energy while still avoiding to trigger on the noise of channels without signals.

A robust way of choosing the trigger level consists in predetermining the Root Mean Square (RMS) value of the noise amplitude over a range of N samples where no pulse is present, in order

to create a reference for the threshold level. By assuming a Gaussian profile of the noise amplitude distribution, the RMS_{noise} value is equivalent to the standard deviation of the noise relative to the baseline BL value which is given by:

$$RMS_{noise} = \sqrt{\frac{1}{N}\sum_{k=1}^{N}(S[k] - BL)^2}, \tag{2.22}$$

where S[k] is the input data stream containing the noise. An identical but less exhaustive method consists of using the Mean Absolute Deviation (MAD)[6] of the input signal S[k] from the baseline BL as an equivalent of the standard deviation:

$$MAD_{noise}[k] = \frac{1}{N}\sum_{n=k-N}^{k}|S[n] - BL|, \tag{2.23}$$

where k is the current time index. This expression can also be written in a recursive form as:

$$MAD_{noise}[k] = MAD_{noise}[k-1] + \frac{1}{N}(|S[k] - BL| - MAD_{noise}[k]), \tag{2.24}$$

in which incoming data points update the current $MAD_{noise}[k]$ value. The number of samples N reflect the dynamics of the digitised data stream and should be set to a value suitable for this method to pick up the changes in the noise fluctuations.

The standard deviation of noise is not necessarily constant, either over time or across different input channels. There are factors such as temperature changes and grounding of the hardware involved (e.g. high voltage supply, preamplifier, sensors) that can lead to changes in the noise level. The trigger level $S_{thr}[k]$ can then be defined as a dynamic quantity as a function of the noise standard deviation:

$$S_{thr}[k] = r \cdot MAD_{noise}[k], \tag{2.25}$$

where r is the trigger threshold in unit of $MAD_{noise}[k]$, which is used as a tuning parameter.

2.3.3 Leading edge timing

The leading edge timing (Leading Edge Trigger (LET)) [27] is the simplest approach to derive a time information from the sampled pulse data. Similarly to the trigger decision (2.3.2), the pulse data are compared to a fixed threshold value. When the signal exceeds the threshold value, the time index k_{LET} of the current sample value is considered as the starting time of the pulse.

The time difference between sampling points and consequently the ADC sampling frequency defines the lower limit for the achievable time resolution. Unfortunately, the ADC sampling frequency cannot be set arbitrarily high, especially when the recording of sampled analogue signals is intended, due to limited storage resources, power consumption or price of the ADC chip. Even though the achievable time resolution can be further improved by interpolating the signal between sampling points, the major drawback of the LET approach lies on its dependence on the pulse amplitude. Assuming constant rise time, for higher amplitudes the signal exceeds the fixed threshold

[6]For the standard distribution, the ratio of the mean absolute deviation to the standard deviation is $\sqrt{2/\pi}$=0.7978....

earlier than for lower amplitudes, which introduces "amplitude walk" in the timing result as illustrated in Figure 2.11. The concept of constant fraction timing (see below) is usually used to solve this problem.

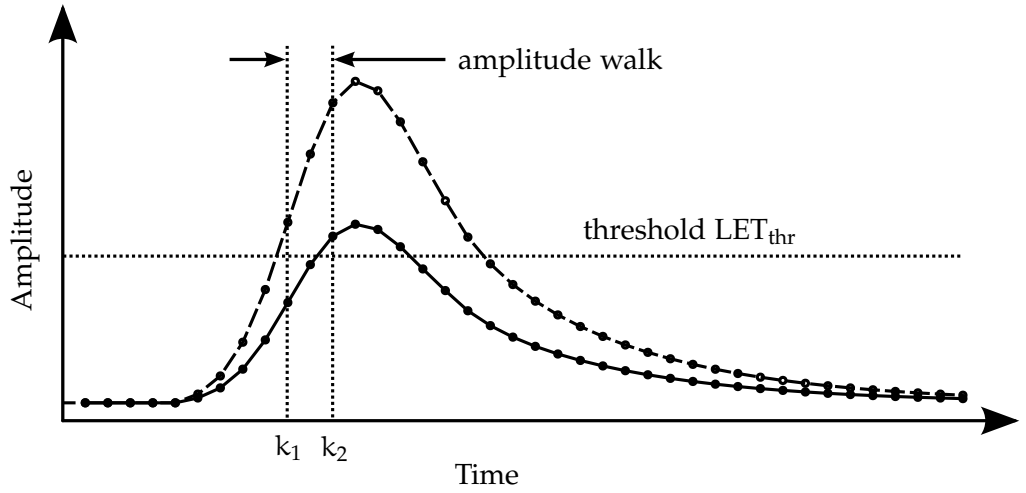

Figure 2.11: Amplitude walk associated with the leading edge timing method: The signal with higher amplitude (dashed) crosses the threshold $\mathtt{LET}_{\mathtt{thr}}$ earlier than the lower signal (solid), which causes the mismatch between k_1 and k_2.

In dealing with fast detector systems such as scintillation detectors readout by photomultiplier tubes (PMTs), an unique method for providing timing information can be applied using leading edge timing if the ADC sampling frequency and the PMT output band width are good enough to sense the arrival of single photoelectrons. Excellent time information can be carried out simply by sensing the arrival of the photomultiplier signal corresponding to the first single photoelectron [28]. This is achieved by setting the trigger level $\mathtt{LET}_{\mathtt{thr}}$ as low as physically possible. Because photomultiplier noise has recurrent spikes that would also trigger at this level, the triggering signals are crosschecked against the calorimetric value[7], i.e. if the signal has no considerable energy following the trigger, the time $t_{\mathtt{LET}}$ is disregarded. The LET is then carried on until this condition is eventually satisfied.

2.3.4 Constant fraction discriminator timing

For the constant fraction discriminator (Constant Fraction Discriminator (CFD)) timing, in contrast to LET, the pulse data is compared to a variable threshold which is scaled with the pulse amplitude. The pulse time is therefore evaluated at a "constant fraction" of the pulse amplitude. Assuming that the pulse rise time does not change with different amplitudes, the CFD gives a time information for the pulse independent of the peak height, essentially eliminating the amplitude-dependent time walk. Figure 2.12 illustrates the constant fraction principle.

Given that the data is available as sampled analogue signals, the most direct way of implementing a digital constant fraction discriminator (CFD) algorithm consists of previously determining the

[7]The calorimetric value is the value of the charge collected in the detector, normally translated into the pulse amplitude or area depending if it is a charge or current pulse.

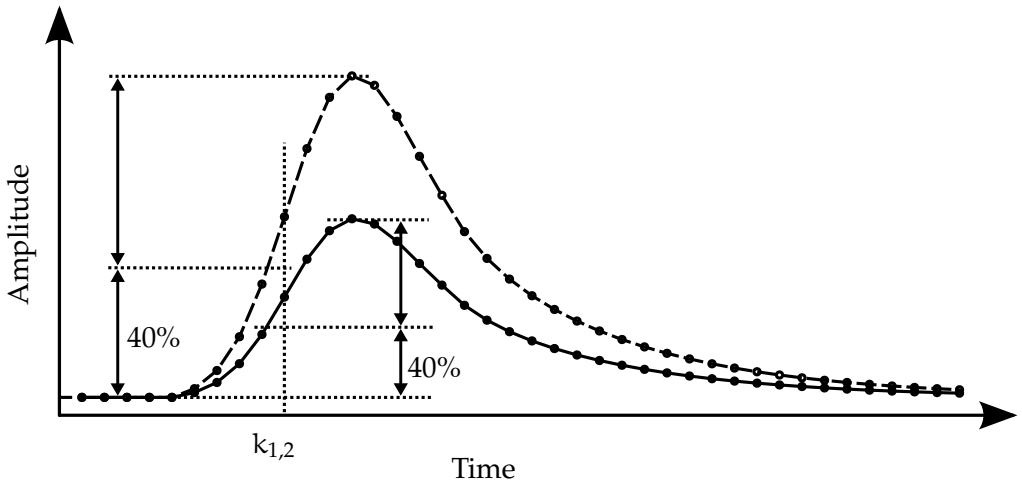

Figure 2.12: Constant fraction discrimination (CFD) timing schematic. For each signal amplitude an independent threshold is calculated, based on the present amplitude fraction (example: 40%), which results in matching time ($k_1 = k_2$) for both signals.

pulse peak height S_{max}. Then, based on the peak height and a defined fraction F_{CFD} the constant fraction threshold CFD_{thr} is evaluated as

$$CFD_{thr} = S_{max} \cdot F_{CFD} \qquad with \qquad 0 < F_{CFD} \leqslant 1. \tag{2.26}$$

The constant fraction timing can therefore be determined in a similar way to the leading edge trigger, where instead of a fixed threshold the determined constant fraction threshold is used.

Another way of implementing a digital constant fraction discriminator CFD, that does not require the peak height is a method usually used with analogue signals [29, 30]. The original signal is delayed by a time delay D and a copy of it is inverted and scaled by a factor F, with $F \in [0 : 1[$. The two signals are then added. This process, with good choice of D and F, transforms the unipolar pulse into a bipolar pulse. The digital bipolar output signal $CFD[k]$ is expressed as

$$CFD_{D,F}[k] = S[k - D] - F \cdot S[k], \tag{2.27}$$

where $S[k]$ is the original input signal and k the sample index. The time at which this signal crosses the zero axis corresponds to the original point of optimum fraction on the delayed signal and is independent of the amplitude, which delivers zero walking. To ensure the CFD timing, the zero-crossing has to occur during or after the peak amplitude of the fractional signal, consequently the delay D value is obtained using the relationship [31]

$$D = t_{rise}(1 - F), \tag{2.28}$$

where t_{rise} is the input signal rise-time (defined as the transition time from 10% to 90% of the amplitude). The waveforms in the digital constant fraction technique are illustrated in Figure 2.13.

Due to the discrete nature of sampled signals, the constant fraction zero crossing often occurs between sampling points, which adds a phase shift ϕ to the true CFD time t_{CFD}. As previously

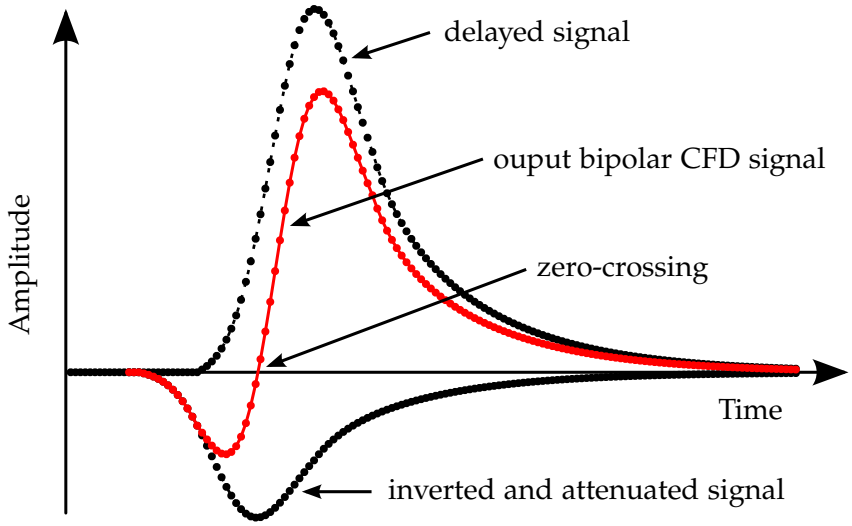

Figure 2.13: Waveforms in the digital constant fraction technique. The zero crossing of the bipolar signal yields the constant fraction timing.

mentioned (Section 2.3.3), further refinement of the pulse time information without increasing sampling frequency, can be accomplished by interpolating the signal between the sampling points. The simplest way of doing so is using a first order linear interpolation. Because the CFD acts on the pulse rising edge, the linear approximation introduces only small errors due to the steep signal slope. The principle of a digital constant fraction discriminator based on linear interpolation is illustrated in Figure 2.14.

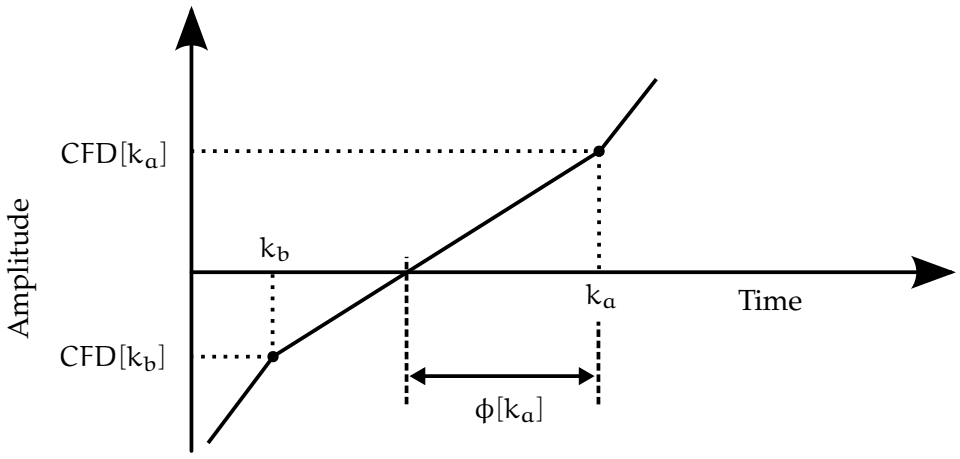

Figure 2.14: Principle of digital constant fraction discriminator algorithm with linear interpolation between the two sampling points CFD_{k_b} and CFD_{k_a}, i.e. before and after the signal crosses the zero axis. The time distance between k_a and the zero crossing time determines the pulse phase shift $\phi[k_a]$.

Considering the linear interpolation between the two sampling points $CFD[k_b]$ and $CFD[k_a]$, corresponding to the amplitude of the digital CFD signal before and after it crosses the zero axis, the phase shift $\phi[k_a]$ between the zero crossing and the time of the sample index k_a can be determined as follows

$$\phi[k_a] = \frac{CFD[k_a]}{CFD[k_a] - CFD[k_b]}. \tag{2.29}$$

The true constant fraction timing t_{CFD} can finally be estimated by subtracting the phase shift from the sample index k_a. Since the original signal has been delayed by D, it also needs to be corrected. The phase corrected t_{CFD} in units of time is obtained using:

$$t_{CFD} = (k_a - \phi[k_a] - D) \cdot T_s, \tag{2.30}$$

where T_s is the sampling period. For alignment purposes, as required for determining the principal pulse shape (see 2.4.1), all signals have to be shifted so they share a common time. Because the signal can only be shifted by integer number of sampling points, unless up-sampling is applied, the constant fraction time t_{CFD} is approximated to its closest sample index, so that:

$$t_{CFD} = \begin{cases} (k_b - D) \cdot T_s & \text{if } \phi > 0.5 \\ (k_a - D) \cdot T_s & \text{if } \phi \leqslant 0.5 \end{cases}. \tag{2.31}$$

2.3.5 Rise-point timing

In some applications, additionally to a precise time reference for the detector signal, it is important to know the pulse rise-point, i.e. the time at which charge starts being collected in the detector. For detector signals with a relatively slow rise time the difference between the CFD time and the rise-point may not be negligible. If the rise time of the detector signal is constant, the difference between the rise-point and the CFD time is also constant and can be determined to estimate the rise-point. However, if the rise time is not constant, the CFD approach results in inaccurate determination of the rise-point that increases with higher constant fraction thresholds. A different approach to obtain the rise-point time consists in approximating the signal leading edge to a linear shape, which is determined by the tangent of the input signal in the sample point where the leading reaches maximum gradient. The virtual point t_z, corresponding to the interception of the tangent line with the baseline, can be used to extrapolate rise-point and is given by:

$$t_z = \frac{BL + m_{rise} \cdot k_m - S[k_m]}{m_{rise}}, \tag{2.32}$$

where m_{rise} is the maximum slope of the input signal leading edge, k_m is the sampling point in which the leading edge slope reaches its maximum, $S[k_m]$ is the amplitude of the input signal at k_m and BL is the baseline level (where $BL = 0$ if the baseline has been subtracted). The values m_{rise} and k_m are obtained using the moving gradient (MG) filter as explained in Section 2.2.3.

The principles of the rise-point timing approach are illustrated in Figure 2.15 using two Gaussian shaped pulses without noise. The two pulses are time aligned so they share the same rise-point. Although the two pulses have different rise time and amplitude, it can be observed that the virtual point in which their maximum slope tangent intercepts the baseline is common to both signals. The extrapolated t_z point can therefore be used as an approximation for the rise-point timing.

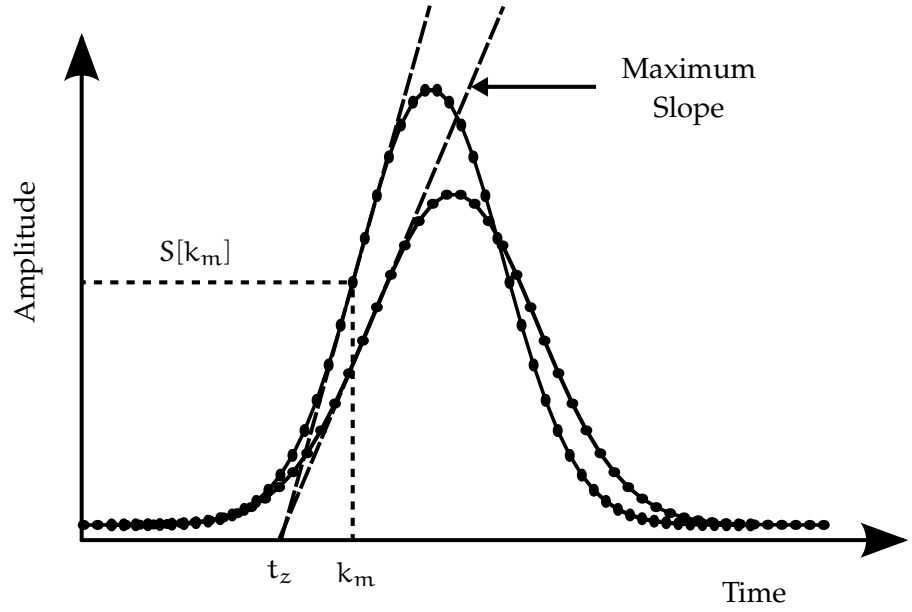

Figure 2.15: Rise-point timing. The tangent lines of the two signals represent their maximum slope during rise time, which converge to the same point t_z at the baseline level. $S[k_m]$ and k_m are respectively the amplitude and the time index of the input signal.

2.4 Pulse shape algorithms

There are applications in nuclear measurements where the information contained in the pulse shape is also important. Discerning the differences in the pulse shape can serve a useful purpose when applied to digitised detector signals. The applications addressed in the present work include (1) correction of temperature-dependent gain effects of a scintillation detector employing a CsI(Tl) crystal; (2) separation of various particle types in a CsI(Tl) scintillator; (3) rejection of defective pulses, caused by factors such as pile-up or noise structures.

Most pulse shape differences arise from changes in the time profile of the current produced in the detector, i.e. changes in the slope of the pulse rising and trailing edge. If the signal is digitised from the output of a charge sensitive preamplifier, the shape of the pulse is obtained by collecting the current produced in the detector across a large time constant and will mainly show changes in its leading edge.

In principle, the waveform of digitised signals for a given detector can be fitted by a function characteristic of the detector response, in which the fitting parameters, constitute a way to classify the pulse shape. Nevertheless, even with a small number of fitting parameters this is a rather complex approach, which is not feasible for a large amount of data or online analysis. More efficient methods of sensing the differences in the pulse shape are normally preferable to achieve Pulse Shape Discrimination (PSD).

One widespread approach to perform PSD consists in deriving a signal based on integrating the total charge over two different time periods, the so called integration method. More recent approaches take advantage of digitising the detector signal using fast sampling ADC. The pulse

shape of sampled analogue signals can be recorded allowing to perform different algebraic PSD methods on the same pulses.

2.4.1 Principal pulse shape

The pulse shape of single detector signals is often not well defined and does not constitute a reliable observable to determine the shape characteristics of the pulse. This is especially true for photosensors with faster response compared to the arrival time of scintillation photons. The presence of noise, baseline fluctuations and the stochastic nature of the scintillation process during pulse formation induce discrepancies among single signals. Assuming that the pulse shape of signals induced by a given particle specie can be considered constant, i.e. the speed in which the shape changes is much slower compared to the rate of incoming events, a better representation of the true pulse shape can be obtained when taking several signals in account to determine the pulse characteristics. Therefore the concept of Principal Pulse Shape (PPS) is introduced to define the true pulse shape, which is obtained by averaging the total pulse waveform over multiple signals.

In order to yield an optimal representation of the PPS, the signals need to be perfectly aligned, thus the signals were shifted accordingly so they share the same time reference. Additionally the signals are trimmed so the PPS length is well defined.

Since the detector signals have different amplitude values depending on the energy deposited in the detector, simply averaging multiple signals would lead to different amplitudes of the PPS depending on the profile of the energy spectrum. Consequently the signals are previously normalised by equalising the signal calorimetric value Q to unity, making the PPS energy independent.

Thus, the simplest way for obtaining the PPS is averaging over a fixed number of sequential signals. Considering a n-th measurement S of the normalised true pulse shape T with noise u, the additive model is assumed:

$$S_n = (T \cdot Q_n + u_n)/Q_n, \tag{2.33}$$

where Q_n is the calorimetric value of S_n and the noise u_n is (usually) an uncorrelated white sequence of random values with equal variance. The PPS (or average) of a set with n pulse signal measurements takes the form of:

$$\mathrm{PPS} \equiv \mu_n = \frac{1}{n}\sum_{i=1}^{n} S_i. \tag{2.34}$$

Supposing that data is continuously taken, the PPS can be recomputed for newer signal measurements. However, it is more efficient to use the old value of μ_n and continuously make updates using new signal measurements S_{n+1}. Considering the arrival of a new signal S_{n+1}, the new average estimate μ_{n+1} is given by:

$$\mu_{n+1} = \frac{1}{n+1}\sum_{i=1}^{n+1} S_i = \frac{n}{n+1}\left(\frac{1}{n}\sum_{i=1}^{n} S_i + \frac{1}{n}S_{n+1}\right), \tag{2.35}$$

which can easily be written in the recursive form as:

$$\mu_{n+1} = \frac{n}{n+1}\mu_n + \frac{1}{n+1}S_{n+1} = \mu_n + K(S_{n+1} - \mu_n), \tag{2.36}$$

where $K = 1/(n+1)$. This provides a revised estimate of the PPS, as a weighted average of the old μ_n and the single value of S_{n+1}. The revised sample variance can also be recalculated recursively from:

$$\sigma^2_{n+1} = \frac{n}{n+1}\left[\sigma^2_n + \frac{1}{n+1}(S_{n+1} - \mu_n)^2\right] = (1-K)(\sigma^2_n + K(S_{n+1} - \mu_n)^2). \tag{2.37}$$

In Equation 2.36 the gain factor K represents how much the correction term $(S_{n+1} - \mu_n)$ will influence the update of μ_{n+1}. Initially, when n is small, the estimates are not very reliable and the correction term has more influence. As n becomes larger so does the confidence in μ_n. Therefore, the weight of μ_n is larger than the weight of the new measurement S_{n+1}. In the limit the gain factor K approaches zero and the correction term is completely ignored. If the signal pulse shape remains constant in time, the value of $K = 1/(n+1)$ is indeed the optimal gain value. However, if the pulse shape is not constant due to factors such as temperature, this approach does not produce a good estimate of the current true pulse shape T.

Equation 2.36 can be recognised as the Kalman filtering [32] state update equation for this simple case. If the detector signal pulse shape is expected to change in time, the Kalman filter provides the means to recursively estimate the current PPS by finding the optimal gain factor K (denominated Kalman gain). This is achieved in the way of minimising the estimate of the mean-square error (with the error being $e_n = \mu_n - S_n$). The optimal gain for the Kalman filter is recursively calculated in the form:

$$K = \frac{P_n}{P_n + R}, \tag{2.38}$$

where P_n is the prior average μ_n error estimate covariance (which in this simple case is the variance σ^2_n), and R is a constant that defines the estimated measurement error covariance introduced by the signals noise u_n (typically R is the variance of the noise, and is often used to tune the filter). The newest estimate for the average μ_{n+1} error covariance is computed recursively:

$$P_{n+1} = (1-K)P_n. \tag{2.39}$$

The whole process can be casted into a series of steps that are followed iteratively. Given n points and an initial calculation of μ_n and P_n (σ^2_n), when a new signal S_{n+1} is measured the gain factor K is calculated using Equation 2.38. Then the average estimate μ_{n+1} is updated using Equation 2.36 and finally, the average error covariance P_{n+1} is updated using Equation 2.39, for the next iteration. The PPS is therefore obtained from the updated average μ_{n+1}.

Figure 2.16 shows the evolution of the principal pulse shape of a scintillation detector with increasing number of averaged signal. It is clear that for a single signal the amount of fluctuation in the amplitude makes it extremely difficult to visualise and analyse the pulse shape. However, the true shape of the pulse starts being revealed the more signals are averaged.

If more then a "family" of similar shapes is present in the dataset, averaging all the signals produce a mean pulse shape that is a blend of all families of shapes, rather than a principal pulse shape. In order to reveal the true pulse shape each family of shapes need to be first grouped. One way of achieving this is using a clustering algorithm as it will be further explained in Section 2.4.3.3.

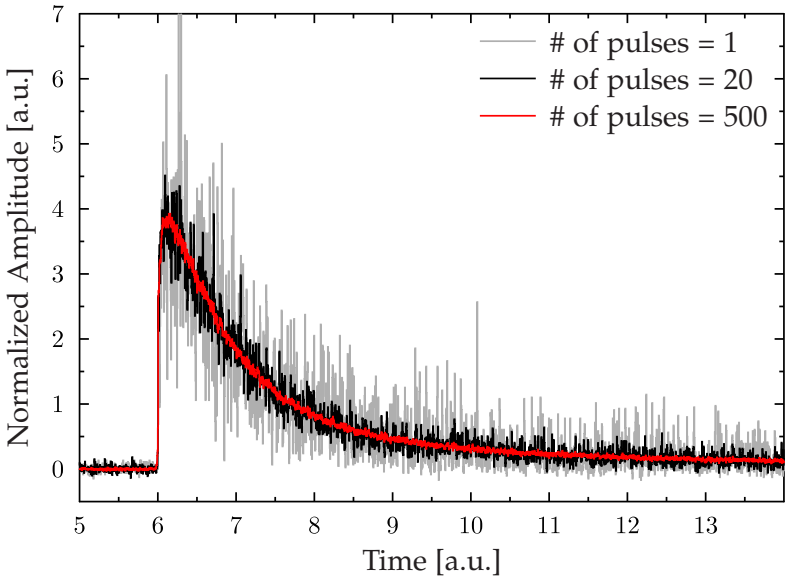

Figure 2.16: Evolution of the PPS as the number of averaged signal increases. The true pulse shape starts being revealed the more signals are averaged.

2.4.2 Integration method

The integration method[33, 34] is a simple and efficient method for PSD. This method takes the ratio of two integrals

$$\frac{Q_1}{Q_2} = \frac{\sum_{k=a_1}^{b_1} S[k]}{\sum_{k=a_2}^{b_2} S[k]} \tag{2.40}$$

over two different regions $[a_1, b_1]$ and $[a_2, b_2]$, delimiting respectively the integrals Q_1 and Q_2. When calculating Q_1 and Q_2 by using the MA filter (2.2.1), a simpler expression is obtained

$$\frac{Q_1}{Q_2} = \frac{MA_N[a_1] - MA_N[b_1]}{MA_N[a_2] - MA_N[b_2]}, \tag{2.41}$$

with the width N of the MA filter being large enough to overlap the two regions. The advantage of taking the ratio over other arithmetic operations is that this approach makes the value independent of the pulse amplitude. Thus, this method can be used to assign a shape parameter that is independent of the energy, without the need of normalisation.

In order to achieve best discrimination results, the integration regions usually require careful manual adjustments. Since the optimal adjustment is related to the principal pulse shape [35, 36], the integration regions can therefore be obtained from the predetermined principal pulse shape. One possible drawback for the integration method arises from the fact that integration regions normally depend on individual detectors, in which manual adjustments are especially inadequate for detector systems composed of many channels.

By defining the two integrations in subsequent regions with an identical width, the integration method can be used to estimate the decay or growth rate of the pulse in a given part. A particular example of this approach is the calculation of the decay time constant of the detector signals featuring a single decay component. Starting by considering two sampling points $S[k_1]$ and $S[k_1 + N]$ at the trailing of the pulse $S[k]$, they are linked with the exponential decay as follows:

$$S[k_1 + N] = S[k_1] \cdot e^{\frac{-N \cdot T_s}{\tau}}, \tag{2.42}$$

where T_s describes the sampling period, and N an integer number of samples. Rewriting the equation 2.42, the decay time τ of $S[k]$ is thus expressed by

$$\tau = \frac{N \cdot T_s}{\ln r_1}, \quad with \quad r_1 = \frac{S[k_1]}{S[k_1 + N]}. \tag{2.43}$$

Selecting the integration regions under the pulse trailing edge so that they have the same width and are subsequent, e.g. $b_1 - a_1 = b_2 - a_2 = N$ and $a_2 = b_1 + 1$, a representative mean value of the decay time $\bar{\tau}$ can then be calculated by employing the integration method to define a mean ratio $\bar{r}$:

$$\bar{\tau} = \frac{N \cdot T_s}{\ln \bar{r}}, \quad with \quad \bar{r} = \frac{Q_1}{Q_2}. \tag{2.44}$$

If the detector signal features more than one decay component this method can not disentangle the contribution of each component involved. Different values of the integration method are obtained depending on the chosen integration regions. The position of the integration areas with respect to the pulse shape has to be kept fixed in order to yield a consistent parameter for pulse shape discrimination.

2.4.3 Geometric approach

After being sampled by an ADC a detector pulse is given by a sequence of discrete amplitude values describing the development of the analogue signal in time. With the knowledge of the pulse timing, the signals can be cropped to contain a fixed number of sampling values corresponding to a well defined pulse region. If the cropped signal $S[k]$ contains L samples, it can therefore be treated as a vector $\vec{s}$ in L dimensions, where the vector $\vec{s}$ is represented by an L-tuple $\vec{s} = (S[k])_{k \in [1,L]}$ with respect to an arbitrarily chosen orthogonal basis of $\mathbb{R}^L$.

By representing the pulses as vectors, the pulse characteristics can be interpreted in terms of both vectorial quantities, magnitude and direction. The vector direction is related to the pulse shape, while the vector magnitude is related to the amplitude and area of the pulse. Consequently, two pulses with similar shape point in similar directions in the L-dimensional vector space. In performing pulse shape discrimination, one vector corresponds normally to the PPS to be identified while the other corresponds to a discriminant shape of reference.

A proper measurement of similarity between the two vectors can be used to determine how close two pulse shapes are from each other. The most intuitive approaches to calculate this similarity are the angle and Euclidean distance between two vectors.

Whenever more than a single "family" of similar shapes are expected in a dataset, often due to parallel detection of different particle species, it is important for many applications to group each family of shapes into different subsets. If a measurement to quantify the similarity of two vectors is available, it is then the aim of a clustering algorithm to find these groups in an unsupervised learning approach.

2.4.3.1 Angle method

If a detector pulse can be expressed as a vector, the angle between two vectors provides means to quantify the similarity of two pulse shapes. The angle $\theta(\vec{s},\vec{u})$ is defined as follows

$$\theta(\vec{s},\vec{u}) = \cos^{-1}\frac{(\vec{s}\cdot\vec{u})}{|\vec{s}||\vec{u}|}, \tag{2.45}$$

where $\vec{s}$ is the PPS vector to be identified and $\vec{u}$ is a discriminant vector of reference, $|\vec{s}|$ and $|\vec{u}|$ are norms of the vectors and $(\vec{s}\cdot\vec{u})$ is the scalar product. Since the angle θ of the two vectors is independent of their magnitude, this method does not require normalisation of the pulses if the pulse shape is independent of the amplitude.

2.4.3.2 Distance method

The distance between two vectors provides another measurement to quantify the similarity of two pulse shapes. The distance $D(\vec{s},\vec{u})$ between a vector $\vec{s}$ representing the shape to be identified and a discriminant vector $\vec{u}$ is the Euclidean norm defined by

$$\begin{aligned} D(\vec{s},\vec{u}) &= \|\vec{s}-\vec{u}\| \\ &= \sqrt{(\vec{s}-\vec{u})^{T}(\vec{s}-\vec{u})}. \end{aligned} \tag{2.46}$$

In contrast to the angle method, the distance between two vectors is strongly dependent on their magnitude. In order to make distance only sensitive to changes in the pulse shape, the pulses have to be normalised to their amplitude or area.

It is important to note that the distance D does not take some properties of real signals such as noise into account. The noise present in the signals is accumulated when calculating the Euclidean norm and may increase significantly the distance between two otherwise very close pulse shapes, producing false results. An alternative way to minimise this problem consists in defining the distance in the form

$$d(S,U) = \sum_{k}(S[k]-U[k]) \tag{2.47}$$

with $S[k]$ and $U[k]$ being the $\vec{e}_k$ component of the vectors $\vec{s}$ and $\vec{u}$. This alternative approach has the advantage of being less sensitive to the noise. In the sum of equation 2.47, the signs of the differences between the single components are accounted allowing for part of the signals' white noise to cancel out.

2.4.3.3 Clustering

Clustering algorithms provide a way to partition a set of N vectors into C clusters[8] such that vectors sharing the same cluster are similar to each other. The criterion for similarity is based on the distance between a vector from the set and the centroid of a cluster. The cluster centroids are representatives of the clusters and are determined by the cluster algorithm. The number of clusters, however, is a parameter of the algorithm and needs to be known beforehand.

[8]Clusters refer to groups of signals of the same shape.

The degree of membership between the i-th vector and the j-cluster defines their closeness and is designated by the membership value u_{ij}. The u_{ij} is normalised to a range of $[0,1]$ so that the total degree of membership is $\sum_{j=1}^{C} u_{ij} = 1$. Depending on the allowed membership values two clustering categories may be considered: (1) hard clustering where $u_{ij} \in \{0,1\}$, i.e. a vector belongs only and fully to a single cluster; (2) fuzzy clustering employing the full range of $u_{ij} \in [0,1]$, i.e. a vector belongs to all C clusters simultaneously, but with different membership degrees u_{ij}. In the following only fuzzy clustering algorithms will be referred because they comprise the general case. Here the Fuzzy C-Means (FCM) algorithm [37, 38] is taken as an example.

The FCM algorithm performs clustering by minimising the objective function J_m of weighted distances

$$J_m = \sum_{i=1}^{N} \sum_{j=1}^{C} u_{ij}^m \cdot D(\vec{v}_i, \vec{c}_j)^2, \quad 1 \leqslant m < \infty \tag{2.48}$$

satisfying the constraints

$$\sum_{j=1}^{C} u_{ij} = 1, \quad i \in \{1, \cdots, N\}, \tag{2.49}$$

$$\sum_{i=1}^{N} u_{ij} > 0, \quad j \in \{1, \cdots, C\}. \tag{2.50}$$

Here, $\vec{s}_i$ denotes i-th vector of the set, $\vec{c}_j$ denotes the j-th cluster and $D(\vec{v}_i, \vec{c}_j)$ is the distance expressing their similarity; N is the number of vectors and C is the number of assumed clusters. The constraint (2.49) ensures that every vector has the same overall weight in the dataset, while the constraint (2.50) makes sure that none of the clusters is empty.

The parameter m influences the fuzziness of the partition: For m approaching one, the membership values u_{ij} become more and more discrete[9], while for $m \to \infty$ all the membership values become $u_{ij} = 1/C$, reaching a maximum fuzziness. A rather weak dependence of the clustering results on m is observed in the range $m = [1.1, 2]$. A more detailed discussion on the m dependence of the FCM algorithm can be found in [39].

The FCM partitioning is carried out by an iterative optimisation of the objective function 2.48, with the update of the cluster centroids c_j calculated as

$$\vec{c}_j = \frac{\sum_{i=1}^{n} u_{ij}^m \cdot \vec{v}_i}{\sum_{i=1}^{n} u_{ij}^m} \tag{2.51}$$

and the update of the value of membership u_{ij} calculated as

$$u_{ij} = \frac{1}{\sum_{k=1}^{C} \left(\frac{D(\vec{v}_i - \vec{c}_j)}{D(\vec{v}_i - \vec{c}_k)} \right)^{2/(m-1)}}. \tag{2.52}$$

The iterative process starts from a randomly chosen u_{ij} obeying the constraints 2.49 and 2.50, and terminates when $\max(|u_{ij}(k) - u_{ij}(k-1)|) < \epsilon$. Where, ϵ is the termination criteria between

[9] For m=1 the algorithm degenerates to the hard K-means algorithm.

[0,1] and k is the iteration step. The random choice of u_{ij} ensures an unbiased application of the algorithm in a most unsupervised approach, however, if some knowledge of the membership function is available a priori, it can be used when initialising the algorithm to improve its convergence.

The centroids of the different clusters are in fact the principal pulse shape, as defined in 2.4.1, for each group of pulse shapes present in the dataset (i.e. the principal pulse of each measured particle specie). It should be noted that the partitioning of the vectors into clusters by the FCM algorithm is based on the distance between themselves ($D(\vec{v}_i, \vec{c}_j)$). Consequently the pulses need to be normalised in order to make the clustering process independent of the pulse amplitude.

Chapter 3

Pulse shape analysis using CsI(Tl) scintillators

The following chapter presents the experimental studies done in the framework of applying pulse shape analysis to digitised signals from CsI(Tl) scintillation detectors. In this analysis the methods presented in the previous chapter were implemented and tested exploiting the signal's shape characteristics. These methods allow performing tasks such as temperature gain correction for CsI(Tl) detector systems and particle identification.

The methods proposed to correct the temperature dependent gain of the detector aim at conserving a good energy resolution in a temperature varying environment without the need to measure the temperature of the detector externally. For performing particle identification, the fuzzy clustering algorithm is used to compute the principal pulse shape associated with different particles species in an unsupervised and automatic way. A discrimination approach that uses principal pulse shapes is proposed to distinguish protons and gamma-rays.

The work presented in this chapter has been published and can be found in [40], and [41]. A detailed explanation of the experiments, the data analysis and results are presented.

3.1 Introduction

The use of scintillation materials for the detection of ionising radiation by converting the energy loss into a light pulse is one of the most common and valuable techniques available in spectroscopy. It allows the detection of a wide range of radiations with energies that go from few keV up to hundreds of MeV.

Thallium-activated caesium iodide (CsI(Tl)) scintillation crystals have been used for the detection of several kinds of ionising radiation in many scientific and commercial applications ranging from experimental nuclear physics to studies of outdoor radiation environment [42, 43]. These crystals have one of the largest scintillation light yields (photons per unit energy deposited) of known scintillating materials and their relatively high density leads to a rather large cross-Section

for gamma-ray interactions. The relatively simple handling and low cost of CsI(Tl) crystals make them particularly suitable for large volume detectors.

One useful property of CsI(Tl) crystals is the existence of more than a single dominant process in their luminescent response. CsI(Tl) scintillation is characterised by multiple components whose intensity and decay time depend on the crystal temperature, ionisation density produced by the exciting particles and thallium doping concentration.

The CsI(Tl) scintillation characteristics are correlated with the signal pulse shape, which can be recorded and (digitally) analysed by using modern readout systems including fast digitisers. Thus, the use of digital pulse shape analysis applied to the CsI(Tl) detector signals represent an adequate approach to perform tasks such as correction of detector gain shifts induced by surrounding temperature changes and particle identification.

3.1.1 Temperature dependence

Like most inorganic scintillators, the scintillation light yield per MeV energy deposited in the CsI(Tl) crystal is known to be a function of temperature [44, 45]. In addition, the most commonly used photosensors, such as Photomultiplier Tubes (PMTs) and Avalanche Photo-Diodes (APDs), are intrinsically temperature dependent devices. Hence, any temperature change in the detector might cause a gain shift. For accurate energy measurements in gamma-ray spectroscopy using CsI(Tl) detectors, temperature variations have to be precisely monitored in order to correct possible detector gain shifts.

As an example, Figure 3.1 shows the gamma-ray energy spectra of a ^{22}Na radioactive source measured by using as detector a CsI(Tl) crystal coupled to a PMT (left frame) and to an APD (right frame) at different surrounding temperatures. The photopeak efficiency for the ^{22}Na gamma-lines remains constant, however, the effect of the temperature changes in the system gain is reflected by the position shift of the 511 keV and 1275 keV peak, respectively.

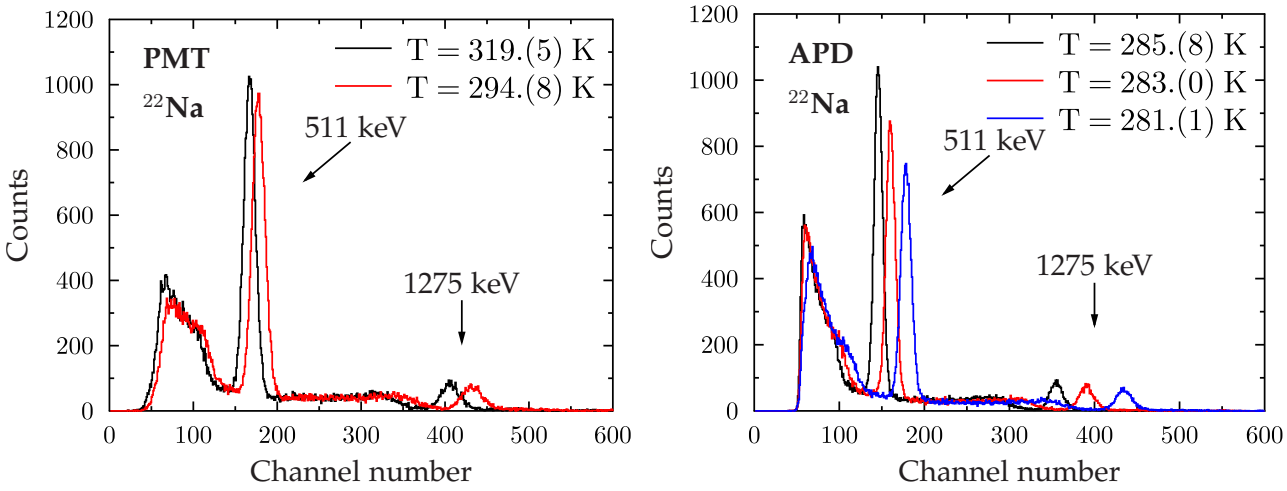

Figure 3.1: Left frame: Energy spectra measured at different temperatures using as detector a CsI(Tl) crystal coupled to a PMT sensor. The spectra are not calibrated to illustrate the detector temperature gain dependence. Right frame: Energy spectra measured at different temperatures using as detector a CsI(Tl) crystal coupled to a APD sensor.

An established technique for stabilising scintillation detectors consists in using radioactive reference sources. The scintillation signals from a known energy are used to evaluate the current detector gain and correct it if needed (e.g. [46]). The use of an auxiliary source, however reduces the spectroscopic sensitivity of the system and may be undesired for safety reasons. A similar technique for gain correction is based on a pulsed reference light source such as a Light-Emitting Diode (LED) (e.g. [47]). Though, this only accounts for effects of the photosensor (the crystal is transparent to visible light) and requires using extra hardware necessary to drive the LED, additionally LEDs are also temperature dependent. The most direct way to correct the temperature of the detector is using temperature sensors on the detector surface. Though, this method also requires extra hardware and thus adds more complexity to the system. Therefore, alternative gain correction methods are desired.

The CsI(Tl) scintillation characteristics have been found to have at least two relevant scintillation components (see Section 3.2.3 for detailed description of the CsI(Tl) scintillation characteristics). The decay time and relative intensity of those components were measured to be also dependent on the crystal temperature when excited by gamma-rays [48, 49]. Accordingly, the scintillation characteristics of CsI(Tl) and consequently the pulse shape of the detector signal are correlated to the temperature of the CsI(Tl) crystal.

It has been demonstrated that the temperature dependence of the CsI(Tl) scintillation yield for gamma rays does not depend on the energy of the incident gamma-rays [44]. Therefore, the temperature dependence of the absolute scintillation yield measured for a given gamma-ray energy should apply to all gamma-ray energies. Additionally, the decay times and relative intensity of the scintillation components of CsI(Tl) crystal were observed to remain nearly constant for gamma-ray energies above 80 keV [50]. For those energies the change of the pulse shape with the temperature can be considered independent of the absolute scintillation light yield. Therefore, the use of Pulse Shape Analysis (PSA) to classify the pulse shape, considering the actual internal temperature of the crystal, provides a mean to directly compensate for the gain shift due to the CsI(Tl) temperature dependent light yield. Assuming thermal equilibrium between the crystal and the temperature sensitive part of the photosensor, it also allows to correct the gain shift of the entire detector system.

A technique for gain stabilisation considering the scintillator temperature has already been presented in [51] in which the single light decay time of a NaI(Tl) scintillator coupled to a PMT is estimated. Then, using the decay time as temperature parameter, the authors perform gain stabilisation under changing the ambient temperature. Another method described in [52] uses an adaptive filtering approach to automatically deconvolute the information from the pulses using a temperature-dependent ansatz. Though, without discussing the stability of the method or providing resolution optimality, the authors show excellent results from a climate chamber test. Both articles show that the information contained in the pulse shape can be used to improve the stability of scintillator based detection systems.

In this work, a method that uses PSA to correct temperature-dependent gain shifts of CsI(Tl) detectors is presented. The suitability of the method is tested employing both a PMT and an APD photosensor to read out the crystal's light yield. PMTs are well established devices in light readout for calorimeters conferring a comprehensive base to study the effect of temperature changes on the pulse shape. On the other hand, APDs have started to be frequently used in connection with CsI(Tl) crystals, as their spectral response better matches the scintillator emission spectrum and

offers better quantum efficiency (see Section 3.2.4), which therefore yields a better overall energy resolution. However, the APD shows a very strong dependence on temperature compared to the PMT (compare Figure 3.1). In order to perform temperature gain correction, two differently defined quantities are proposed, that parametrise the principal pulse shape of the detector signals. The first quantity uses the ratio of integrals over two different parts of the signal, the second one considers the sampled signal as a multidimensional vector and by means of vector calculations measures the current pulse shape variations relative to a reference principal pulse shape. The correlation between the peak positions in the spectra is used to derive a correction factor that is then employed to correct the gain changes in a second dataset.

3.1.2 Particle ID

Particle IDentification (PID) is a fundamental task in many experimental setups. Since, in response to different ionising radiation, CsI(Tl) scintillation detectors yield light components whose amplitudes and decay times depend on the particle species [53], the use of PSA provides an appropriate approach for PID.

The results of various digital PID methods have been compared in [54], where good separation of gamma-rays and particles has been reported using CsI(Tl) crystals. A widely adopted method using PSA to achieve particle identification is the integration method (e.g. [33, 34, 55]). This method uses the integrals over two different regions to discriminate between particle species.

For best particle discrimination, many of the PID methods rely upon good tuning of their parameters. In the integration method for instance, the regions have to be adjusted by hand for each individual detector. Factors such as ageing and exposure to radiation might change the detector response over time. Also external factors such as temperature affect the pulse shape characteristics, requiring redefinition of the integration regions. Thus, calibration procedures which require regularly performed human supervision, are a hard task for large setups with many detectors or for detectors used in environments where the conditions might vary strongly. For this reason it is desirable to develop a procedure that performs PID calibration of a detector system with the least requirement of human supervision. The knowledge of the principal pulse shape for a given incident particle species and a given detector might be useful to optimise the pulse shape discrimination methods. The fuzzy c-means clustering algorithm commonly used for pattern recognition, provides a convenient way to find the principal pulse shapes associated to the different particle species. This method has already been proven to perform calibration for gamma-neutron discrimination in a fully automatic and unsupervised manner for liquid scintillator detectors [39]. In the present work the same method is applied to perform PID in CsI(Tl) crystal. The information obtained from the clustering is used to discriminate gamma-rays and protons; the results are compared with the integration method.

3.2 Experimental Details

Several experiments have been performed to obtain the data used to develop and demonstrate the methods proposed for temperature dependent gain correction and particle identification. These

experimental setups are explained in the following Section. Detailed information of the used photosensor characteristics and scintillation crystals is also given.

3.2.1 Temperature gain correction

To produce the experimental data, two setups were individually prepared employing the same CsI(Tl) crystal with the dimension of $15 \times 15 \times 30$ mm^3. Both setups are identical, differing only in the photosensor used to read out the crystal's scintillation light. A schematic drawing of both setups is illustrated in Figure 3.2. For the first setup— the PMT setup— the crystal was coupled to a Hamamatsu PMT with a photocathode of 15 mm diameter. A supply voltage of 1200 V was applied to the photomultiplier. For the second setup— the APD setup— the crystal was coupled to a Hamamatsu S8664 1010 APD photosensor [56, 57] with a large area of 10×10 mm^2. A Mesytec[1] MPRB-16 charge sensitive preamplifier, which also provides a stabilised bias voltage of 425 V, was used as read-out electronics for the APD. The signals from both detector systems were sampled using a Struck SIS3316[2] VME digitiser at a sampling frequency of 250 MSPS, a resolution of 14 bit and an input range of 5 V. Each one of the setups was employed separately and two measurements per setup were successively performed under induced temperature changes. The first measurement was used to develop the methods for temperature gain correction, while the second measurement was used to test the performance of the methods independent from the data used for calibration.

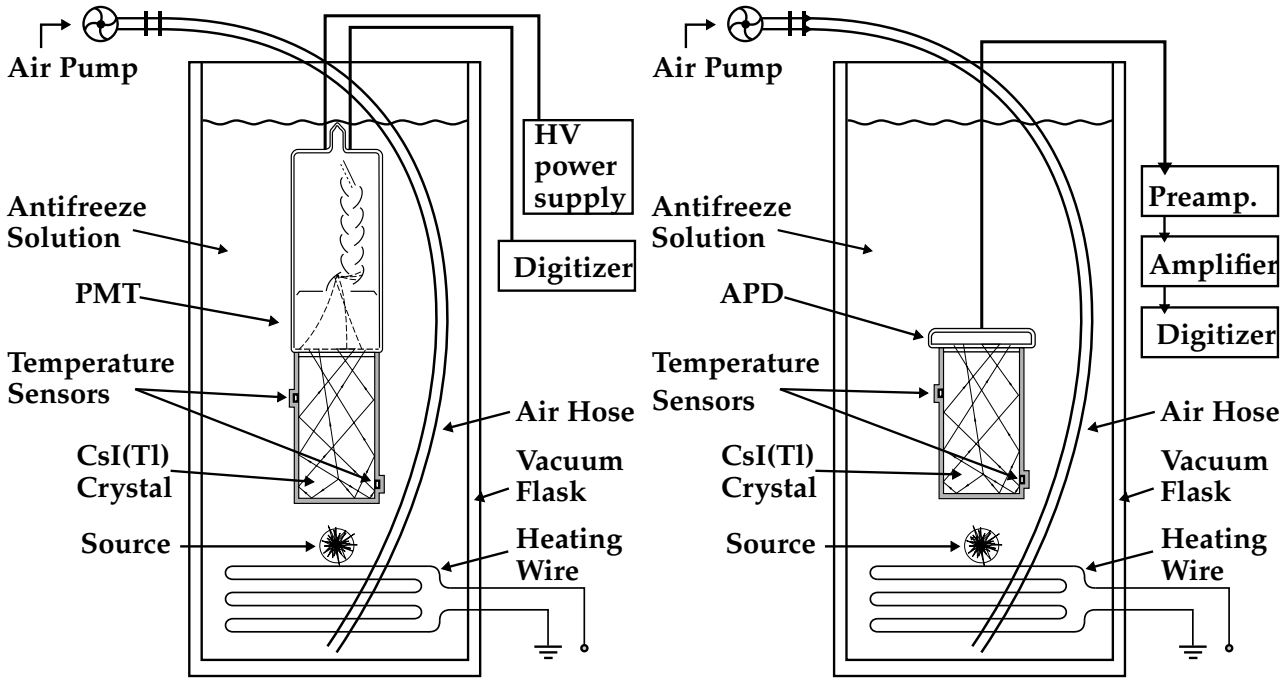

(a) PMT setup. **(b)** APD setup.

Figure 3.2: Schematic drawing of the two setups used to record the CsI(Tl) scintillation data at different temperatures. (a): Schematic drawing of the setup employing a PMT photosensor. (b): Schematic drawing of the setup employing a APD photosensor. The two setups differ only in the photosensor used and their required electronics.

[1]Mesytec — http://www.mesytec.com.
[2]Struck innovative systems — http://www.struck.de/sis3302.htm/

Apart from the detector and the respective readout electronics, both experiments were conducted in a similar way. The CsI(Tl) crystal was wrapped in a thin layer of reflective plastic to maximise the light collection and thus improve the energy resolution. One of the crystal's square surfaces (10×10 mm^2) was kept uncovered and was coupled to the photosensor with silicone grease to improve light transmission. The crystal was additionally wrapped in black electric tape to ensure light isolation and to attach two PT100 resistance thermometers (RTD) to the side surfaces of the crystal (one close to the bottom and another close to the top on the opposite side of the crystal, see Figure 3.2). The RTDs were read with an NI6217[3] analogue input module from National Instruments, which allowed to register and monitor the temperature with a precision better than 0.1 K while conducting the experiment. A ^{22}Na source was placed about 2 cm away from the crystal's front face on the opposite side of the photosensor. The photosensor, the crystal and the source were immersed in an antifreeze liquid solution contained inside a thermally insulated vacuum flask. A heating wire was placed at the bottom of the flask allowing to warm up the liquid in a controlled way.

For every experiment the liquid temperature started from a low value and was slowly increased in steps of approximately 1.5 K estimated by dissipating 3.6×10^3 J per step. For the experiments involving the PMT setup, a temperature range between 261.(6) K and 319.(5) K was covered. For the experiments involving the APD setup, a narrower temperature range from 276.(6) K to 307.(0) K was covered due to the APD strong gain dependence on temperature causing this detector to quickly saturate. While heating up the liquid, air was pumped into the liquid at the bottom of the flask forcing a turbulent convection to improve heat transfer and facilitate thermal uniformity[58]. The high heat transfer of the liquid (compared to the air) allowed to reach the equilibrium between the crystal and the liquid quickly within about 10 min. The temperature of the crystal was assumed to be the averaged value of the two RTDs and whenever the crystal temperature stabilised it was assumed to be in equilibrium with liquid temperature. A maximum temperature difference of ~0.4 K was registered between the two RTDs during the measurements.

The experimental data was taken in runs of 3 min duration after achieving thermal equilibrium, in which the temperature changes during data acquisition were observed to be less than 2×10^{-2} K/min and therefore considered to be constant. The Multi Branch System (MBS) data acquisition software was used to record to disk an amount of 80,000 traces, each consisting of 5000 and 8000 samples for the PMT and APD setup, respectively. Each trace was recorded upon an internal trigger of the digitiser, and the position of the pulse signal in the trace was set to have a clearance of 1500 samples between the trigger sample and the beginning of the trace.

3.2.2 Particle ID

The experimental data was taken during a beam time at the Munich Tandem-Accelerator (Maier-Leibnitz Laboratory (MLL), Garching)(see e.g. [59, 60]). The Tandem-Accelerator provided a proton beam with an energy of 24 MeV. The protons were shot on a 70 μm CD_2 target foil. The nuclear reactions inside the foil allowed to obtain simultaneously elastically scattered protons and gamma-rays from inelastically scattered protons. Both protons and gamma-rays were detected by a 8×4 array of CsI(Tl) scintillation detectors [61–63] placed at an angle of 37° with respect to the beamline.

[3]National Instruments — http://sine.ni.com/

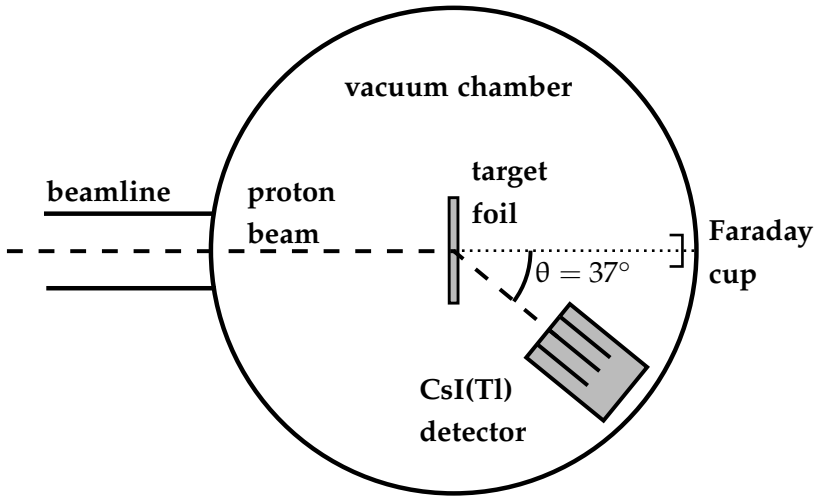

Figure 3.3: Schematic drawing of the detector setup at the MLL.

A schematic drawing of the detector setup at the MLL is illustrated in Figure 3.3. Each crystal was read out using a Hamamatsu S8664–1010 APD. The detector signals were obtained with a Mesytec MPRB-16 charge sensitive preamplifier optimised to the APD's high capacities, which also provided the bias voltage for the APDs. The detector signals were sampled by an Analogue to Digital Converter (ADC) on a FEBEX2 FPGA[4] board [64] at a sampling rate of 60 MSPS and resolution 12-bit. The measured count rate in a single crystal was of the order of 200 events per seconds resulting in a very small amount of piled-up events. The MBS data acquisition software was used to record to disk the signal waveforms with 2000 samples each.

3.2.3 CsI(Tl) scintillator properties

The CsI(Tl) scintillator material exhibits a property known as luminescence. When exposed to sources of energy, such as heat or radiation, the scintillator absorbs and reemits the energy in the form of visible light. The reemission occurs mainly immediately after absorption (i.e. within 10^{-8}s, roughly the time taken for atomic transitions). However, especially when exposed to strong radiation for a long time, CsI(Tl) scintillators show afterglow (phosphorescence) typically up to 5% of the total light yield after 3 ms [65].

CsI(Tl) scintillators have found extensive use in nuclear applications due to their low cost, easy availability and excellent properties. With a relatively high density (4.53g/cm^3) and atomic number (Z = 54) they provide a large cross-Section for gamma-rays and allow for more compact detector designs. CsI(Tl) is one of the brightest known scintillators with the highest conversion efficiency (64,000 photons/MeV) [66]. According to [49, 67], the intrinsic resolution of CsI(Tl) crystals for 662 keV photons at room temperature is around 4.8% and this value tends to worsen for lower energies and higher temperatures. Moreover, CsI(Tl) crystals have good plasticity, are easy to handle and are less hygroscopic compared to NaI(Tl) (often used in similar applications).

The CsI(Tl) light output intensity has been presented in a number of experimental works performed with gamma-rays and charged particles (e.g. [48, 65, 68, 69]). In all measurements two light components were found with significantly different decay times: A fast component with τ_{fast} =

[4]Field Programmable Gate Array.

0.6–0.9 μs and a slow component with τ_{slow} = 3.3–4 μs. In more recent publications [49, 50], an even slower tail component with $\tau_{tail} \simeq 16$ μs decay time (at room temperature) has been observed, which consists of around 22% of the integrated luminescence. Models of possible processes that lead to these CsI(Tl) decay components are well described in the literature [70–72]. In order to preserve a good resolution, the CsI(Tl) long scintillation decay time requires a long integration time of the charge-sensitive preamplifier of typically a few μs.

The CsI(Tl) scintillation characteristics depend on the Thallium concentration. While the decay times of CsI(Tl) are known to be independent of the thallium concentration upon excitation with gamma-rays [69], the light yield of CsI(Tl) (particularly the relative intensity of the $^{+}$Tl band transition) increases with the thallium concentration [73, 74]. The scintillation characteristics also depend on the crystal temperature and type of ionising particle, as already pointed out in Section 3.1.1 and 3.1.2.

After excitation by a gamma-ray or a particle, the fraction of energy deposited in the CsI(Tl) scintillator is released by the emission of photons following multiple Poisson processes. These processes determine both the rise time and the decay time of crystal scintillation characteristics. Assuming that the luminescent states of the CsI(Tl) are populated and depopulated by independent processes, the light output of a scintillation event, $L(t)$, can be described to a good approximation by a sum of exponential components [48, 68, 75, 76]:

$$\begin{aligned} L(t) &= \textstyle\sum_i \frac{h_j}{\tau_j} e^{-t/\tau_j} = \sum L_j e^{-t/\tau_j} \quad t \geqslant 0 \\ L(t) &= 0 \qquad\qquad\qquad\qquad\qquad\quad t < 0, \end{aligned} \tag{3.1}$$

where h_j, τ_j and L_j are the integrated luminescence, characteristic decay time constants, and initial intensity of the i-th exponential component. Because τ_{tail} is much longer compared to τ_{slow}, which makes the effects of the tail component in the pulse shape less noticeable, only the two fastest decay components are usually taken as relevant for the purpose of pulse shape analysis. The approximated model for the light output intensity becomes:

$$L(t) = \frac{h_f}{\tau_f} e^{-t/\tau_f} + \frac{h_s}{\tau_s} e^{-t/\tau_s} - \frac{h_r}{\tau_r} e^{-t/\tau_r}, \tag{3.2}$$

where the indexes f, s and r refer to the fast, slow and rise components of the scintillator's luminescent states. The CsI(Tl) emission spectrum concentrates mostly at the long wavelength region (with maximum emission at around 550 ns), which makes this material well-suited for APD photosensors, as it will be shown in the next Section. The emission spectrum of the crystal sample used in the present work, with a Thallium concentration of around 0.2 mol/%, is illustrated in Figure 3.4.

3.2.4 Photosensors

This Section gives a description of the photosensors used in the present work to read out the scintillation light of the CsI(Tl) crystal.

Photosensors are devices designed to convert low intensity scintillation light into an electrical signal. Generally this involves generating a detectable current signal proportional to the number of incident scintillation photons. The processes involved can be divided into three steps: conversion of

incident photons into electrons or electron-hole (e-h) pairs; multiplication of the primary electrons to a detectable level; collection of the electrons to form the signal. Not all the photons hitting the active area of the photosensor will produce an electron. The Quantum Efficiency (QE) is a quantity defined as the percentage of incident photons contributing to the emission of primary photoelectrons (and that reach the first multiplication stage). The QE is usually a strong function of the photon wavelength λ.

In applications involving low intensity signals, the PMT is generally used because it provides a very high gain (typically 10^6) and sufficient signal-to-noise ratio. This extremely sensitive device is capable to respond on very low light intensities and usually does not need further amplification of the anode signal. However, the use of PMTs has some disadvantages, such as sensitivity to magnetic fields, comparably low quantum efficiency[5] for input light signals and a rather high power consumption. Photodiodes (PDs), on the other hand, have very good quantum efficiency (close to 100%) in the visible and near red. A drawback of using PDs is that they have no internal gain and require preamplification to provide a large enough signal. In the field of experimental physics background noise may dominate over the signal. Signal carriers can be more than 10 times fewer than those of noise charge [77], which are either due to noise in the readout electronics or due to dark current in the detector.

The good characteristics of both PMT and PD are combined in the APD; it is a silicon photodiode with an internal gain [78] (typically 10–100 times or more). The APD exhibits excellent quantum efficiency (>80%), although when operated in linear mode, its gain is significantly smaller compared to a PMT. Because of the relatively small gain, a charge-sensitive preamplifier is needed, which decreases the very fast rise time of the APD (<2 ns). During the past two decades large area APDs operating as linear detectors have become available. These modern APDs, especially with reverse structure[6][79], can replace photomultipliers as a scintillation photon detector in high energy physics and in other applications. The energy resolution obtained with large area APDs is better or comparable to those obtained with a PMT [80, 81].

Many of the applications for which large area APDs are suitable for have until now mostly relied on PMTs. However, APDs offer a number of advantages over conventional photomultipliers. The most evident advantage is that it is a compact, monolithic photosensor and thus is usually useful in applications where the space is at premium, such as large detector arrays with high granularity. Traditional PMTs are relatively bulky, mechanically fragile glass tubes and sensitive to magnetic fields.

Besides a much higher quantum efficiency of the APD compared to a PMT, the APD quantum efficiency also spans a much broader wavelength range of its spectral response towards the infrared region (>60% between 390 and 930 nm). The spectral response of the APDs is therefore particularly advantageous for scintillation detection using CsI(Tl) crystal, which have significant light yield at longer wavelengths. While the peak sensitivity of typical PMT photocathodes is below λ = 500 nm, the APD spectral response fits much better to the CsI(Tl) emission spectra [56, 82]. Figure 3.4 shows the comparison between the spectral emission of a CsI(Tl) crystal and the spectral response of the PMT and APD devices used in the present work.

[5]For the PMT the quantum efficiency is mostly limited by light transmission through the semitransparent photocathode and the photoelectron escape probability from the photocathode.

[6]In reverse APDs the depletion is located in the front of the device.

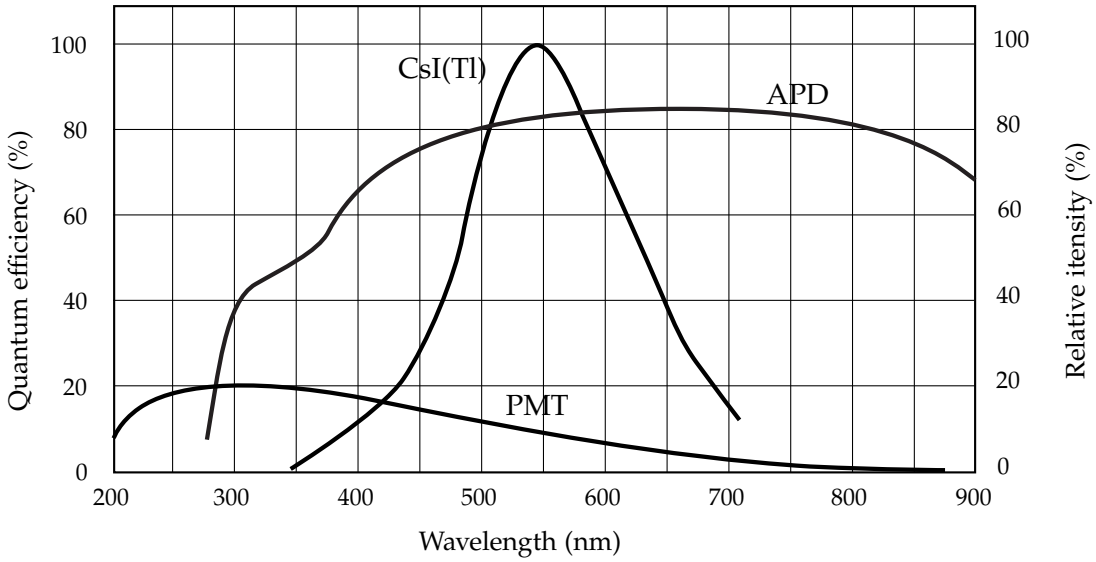

Figure 3.4: Emission spectrum of the CsI(Tl) scintillation crystal (from [83]), and quantum efficiency of the Hamamatsu R1464 PMT and of the Hamamatsu S8664–1010 APD used in the present studies.

Another advantage of APDs over to PMTs include less sensitivity to external magnetic fields, lower power consumption and a lower price due to its mass production potential.

PMT — operational principles

The simplified structure of a typical Photomultiplier Tube (PMT) is illustrated in Figure 3.5. A PMT is a vacuum tube (usually glass), consisting of a light input window, a photosensitive layer (photocathode), an electron multiplier structure (dynode) and an anode. The photocathode, exploiting the photoelectric effect, serves to convert the incident light photons entering the tube window into low-energy photoelectrons. The photoelectrons are accelerated and focused such as to strike on the first dynode where multiplication takes place by secondary emission effect. The secondary emission is repeated in the subsequent dynodes resulting in a bunch of electrons multiplied to 10^6 or more, which are at the end collected by the anode. The vacuum conditions inside the tube are required in order to efficiently multiply low energy electrons.

The general parameters of the PMT used in the present work are gathered in Table 3.1.

PMT pulse formation — modelling

For a PMT, the single electron response shape is mostly determined by the electron cascade multiplication that occurs in the dynode system. This process essentially obeys a Poisson distribution. The PMT response function for single photoelectrons can be fairly well reproduced by the response of a semi-Gaussian[7] shaping filter (CR-RC^4) ($\sigma \simeq 7$ ns) [84].

Following the interaction of radiation in the scintillator crystal, the arrival time of the scintillation photons at the photocathode can be represented by an exponentially distributed sequence of a given

[7] A semi-Gaussian shaper CR-RC^n of the n-th order is constituted by an approximated differentiator of time constant τ_{cte} followed by n approximated integrators of the same time constant τ_{cte}.

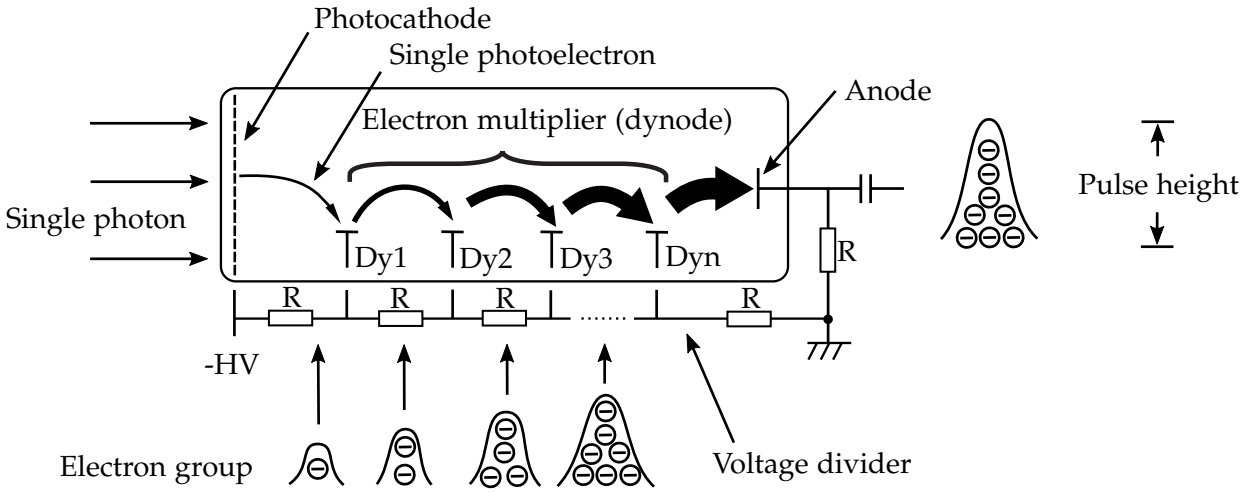

Figure 3.5: Schematic view of the multiplication process in a PMT device. The photoelectrons ejected from the photocathode are accelerated towards the first dynode (by a DC potential typically of 100 to 200 V), and undergo multiplication in the subsequent dynodes.

Table 3.1: Parameters of the Hamamatsu R1464 PMT used in the present work.

Useful size (diameter)	15 mm
Window	UV glass
Photocathode	Multialkali
Number of dynode stages	10
Anode dark current (HV = 1000V, temperature = 273 K)	10 nA
Spectral range	185 to 850 nm
Gain	10^6
Quantum efficiency (wavelength = 390 nm)	19%

number of "Diracs" (or "1"s). This exponential distribution is determined by the crystal scintillation characteristics. The scintillator and PMT's overall efficiency results in an attenuation of the number of photoelectrons emerging from the PMT photocathode. The simulated photoelectron arrival times at the cathode, selected from an exponential random distribution obtained from Equation 3.2, are depicted in Figure 3.6 (a), for two different numbers of photoelectrons.

To account for the amplification (through each dynode gain and number of dynodes) the height of the simulated single photoelectron PMT response was scaled by a Poisson distributed random factor. To account for the electron transit time spread, every Dirac representing the photon arrival times was delayed by a Gaussian distributed random value.

The typical PMT pulse shape, as it is measured as a voltage across the input resistance of the digitiser, is then obtained by convoluting the PMT single electron response function with the sequence of Diracs. Additive Gaussian noise was added to the signal in order to simulate the analogue noise, and down-sampling was done to match the digitiser frequency. Figure 3.6 (b) illustrates a simulated PMT signal containing 1500 photoelectrons.

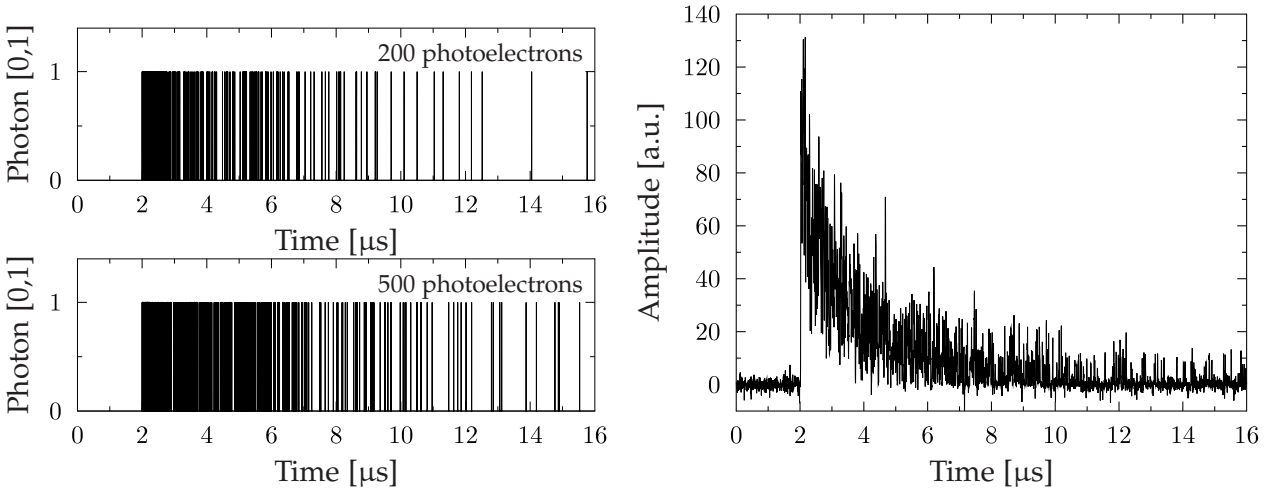

(a) Photoelectrons arrival times.

(b) Simulated PMT signal.

Figure 3.6: Simulated arrival times of 200 ((a),top) and 500 ((a),bottom) photoelectrons statistically distributed accordingly to CsI(Tl) scintillation characteristics as defined in Equation 3.2; the time constants τ_{rise} = 25 ns, τ_{fast} = 710 ns and τ_{slow} = 3260 ns were used. Together with a simulated CsI(Tl) scintillation signal (b) with additive white Gaussian noise; the signal includes 1500 photoelectrons.

APD — operational principles

The operation principle of an Avalanche Photo-Diode (APD) is based on the conversion of the energy deposited in the semiconductor bulk by each impinging photon into a cascade of moving carrier pairs. The simplified structure of a reverse type APD is illustrated in Figure 3.7. The APDs are strongly reverse biased photodiodes in which the junction electric field is large, creating a volume in the junction depleted of charge. The charge carriers entering the depletion volume are therefore accelerated in the electric field, acquiring enough energy to excite new carriers by the process of impact ionisation. The newly created carriers might create new ones, and so on. Thus, creating an electron avalanche towards the anode which is then detected in the preamplifier.

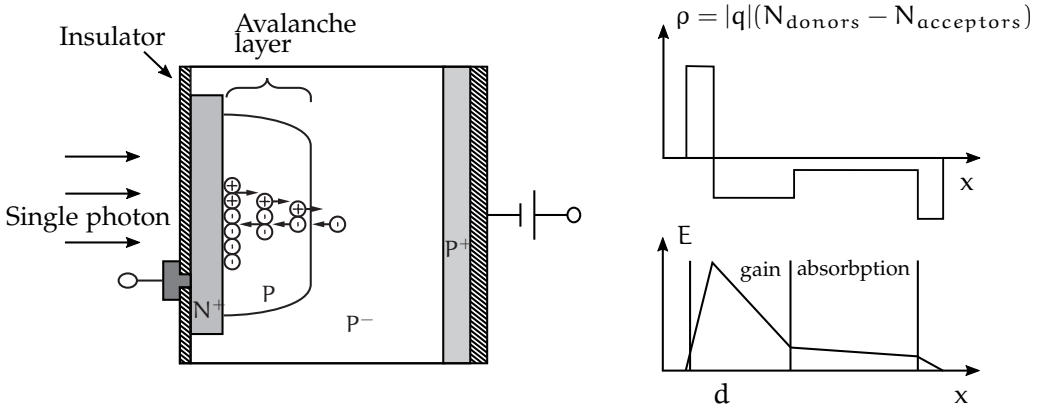

Figure 3.7: Sketch of the APD cross Section with doping (not to scale), shown on the left. The space charge region with a net charge provided by a doping density ρ of fixed ions (donors and acceptors) and a resulting electric field profile E, are show on the right.

The reverse type APDs are especially designed to be combined with scintillators. The high field multiplication region is located in the front end of the device (typically 5 μm from the surface [77]). Most of the light emitted by the scintillator is absorbed within the first 1–3 μm of the depletion layer. The generated electrons then undergo full multiplication. Since the thermal electrons do not amplify inside the device (dark current undergoes only hole multiplication), the APD reverse type has the advantage of reducing the dark noise contribution significantly.

The APD is capable of detecting low level light, however, it requires special care and handling such as the need for very stable reverse voltage and detailed consideration of its temperature dependent gain characteristics. The gain of the APD is expressed as an exponential function of bias voltage and temperature [85]. The change of the gain M with the bias voltage is described by

$$\frac{1}{M}\frac{dM}{dV} = 4.5\%/V \tag{3.3}$$

at the gain of 100. Because the avalanche multiplication is affected by the mean free path of the electrons between multiplication, which is temperature dependent, also the gain varies with temperature T and is (at the same gain of 100) approximated by

$$\frac{1}{M}\frac{dM}{dT} = -3.3\%/T. \tag{3.4}$$

The general parameters of the APD adopted for the present work are resumed in Table 3.2.

Table 3.2: Parameters of the Hamamatsu S8664–1010 APD used in the present work.

Active surface area	10×10 mm^2
Window	Epoxy resin
Package	Ceramic
Dark current: I_D(gain = 100, temperature = 273 K)	10–31 nA
Break-down voltage: V_{brk}(temperature = 273 K)	460 V
Bias voltage: V_G(temperature = 273 K)	425 V
Capacitance: C_{det}(gain = 100, temperature = 273 K)	270 pF
Type:	Reverse
Quantum efficiency (wavelength = 500–830 nm)	80%
Quantum efficiency (wavelength = 390–930 nm)	60%

APD pulse formation — modelling

As previously mentioned, for the APD, the photoelectron current created by the incident scintillation light is first passed through a charge-sensitive preamplifier before being digitised, to improve the signal to noise ratio. As the light detection process in the APD photosensor has no significant delay, the detector response function is mainly determined by the following preamplifier.

The response function of the charge-sensitive preamplifier, used for the present experimental setups, is an exponential function with a single decay time component τ_p. Since the fall time of the preamplifier is usually much larger than the time constants of the scintillator (to minimise the ballistic deficit and to get a maximum fraction of the signal), the preamplifier integrates the input signal

from the scintillator APD. The signal pulse shape $Q(t)$ at the charge-sensitive preamplifier output is described by the time domain convolution of the scintillator light output ($L(t)$) and preamplifier ($H(t)$) response functions:

$$Q(t) = L(t) * H(t) = \int_0^t L(t')H(t-t')dt' = \int_0^t [L(t)]\, e^{\frac{(t-t')T_s}{\tau_p}} dt', \tag{3.5}$$

where $L(t)$ is obtained according to Equation 3.2. After sampling by the digitiser, the time-discrete digital function $Q(t)$ becomes:

$$Q(k) = \sum_{k'=0}^{k} \left[\frac{h_f}{\tau_f} e^{-kT_s/\tau_f} + \frac{h_s}{\tau_s} e^{-kT_s/\tau_s} - \frac{h_r}{\tau_r} e^{-kT_s/\tau_r} \right] e^{\frac{(k-k')T_s}{\tau_p}}, \tag{3.6}$$

where T_s is the ADC sampling time. Figure 3.8 shows the simulation of a typical APD pulse shape at the preamplifier output. The scintillator light output distribution $L(k)$ was randomly populated with 1500 photons. Additive Gaussian noise was added to the signal in order to simulate the analogue noise. The exponential decay time of the preamplifier response function was estimated by fitting the recorded signal, see Section 3.3.2.

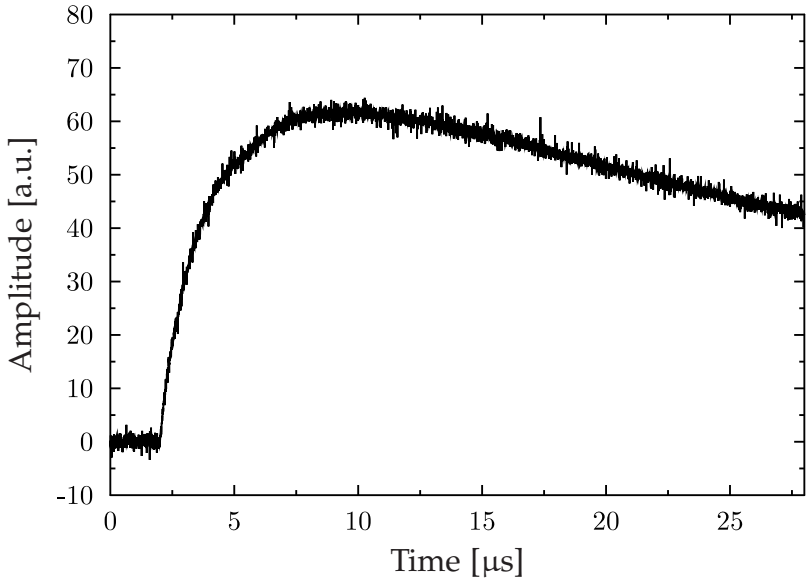

Figure 3.8: Simulation of a typical APD signal shape after passing through a charge sensitive preamplifier. The signal was obtained by convoluting the scintillator yield and the preamplifier single exponential response with a decay time of 40.6 μs. The scintillation characteristics were simulated by 1500 electrons randomly distributed according to Equation 3.2, in which the time constants τ_{rise} = 25 ns, τ_{fast} = 710 ns and τ_{slow} = 3260 ns were used.

3.3 Digital processing of CsI(Tl) detector signals

Before applying the PSA methods to perform the tasks of temperature gain correction and PID, some basic feature extraction operations are required. Every recorded raw signal was first prepared by performing baseline correction, noise reduction and time alignment. Piled-up or otherwise distorted signals were also removed from the dataset. The individual steps are described in the

following. Different sampling frequencies were used during the different experiments. Because the preparation steps were performed identically regardless of the sampling frequency, for simplicity, in the following all pulse signals are treated as if they were sampled at 250 MSPS.

At first, the baseline voltage is estimated by taking an average over the first 850 samples (3.4 μs) of the trace, where no signal is present, and then subtracted from the signal.

3.3.1 Trigger and time alignment

For timing and triggering a different approach was used regarding each of the APD and PMT detector systems.

PMT signals

The PMT provides a very fast response compared to the overall scintillation process in the CsI(Tl) crystal, which results in a very fast rise time of the signals. This fast rising time is correlated to the arriving of the first scintillation photons. Therefore, excellent timing can be achieved by sensing the first photons using a simple Leading Edge Trigger (LET).

The LET returns the sample number k_{LET} when the signal exceeds a given threshold. This sample number k_{LET} is then used as the pulse time-stamp for signal alignment. The threshold of LET was dynamically defined as 6 times the Root Mean Square (RMS) noise of the baseline. Because the threshold is set low enough to trigger on the first arriving photons, it also triggers on single spikes present in the trace (see Figure 3.9 at around 1800 ns), caused by thermal emission of electrons from the photocathode of remaining long tail luminescence of previous signals. Consequently, to avoid (recurrent) triggering on those single spikes, a calorimetric check is performed by evaluating the signal's amplitude upon applying a 60 samples wide moving average (MA_{60}) filter to smooth the raw signal. The raw and MA_{60} signals are illustrated in Figure 3.9. If the amplitude of the MA_{60} signal also exceeds the defined threshold in a 240 ns interval after k_{LET}, the LET is considered valid. Otherwise, k_{LET} is skipped and the process continues until a valid LET is found in the trace. The PMT signals were time shifted with respect to the LET so that $k_{LET} = 1500$ (corresponding to 6μs).

APD signals

The recorded APD signals are shaped by the characteristic response function of the charge sensitive preamplifier. The much slower rise time of these signals compared to the ADC sampling frequency makes LET sensitive to the signals' amplitude. Therefore, a Constant Fraction Discriminator (CFD) filter was used to obtain the pulse time-stamp independent of its amplitude. For better time alignment, before CFD timing, the APD raw signals were filtered by applying a Moving Binomial (MB) smoothing filter to remove the high frequency noise, improving the signal-to-noise ratio and reducing time-stamping jitters.

Representative MB and CFD signals are illustrated in Figure 3.10. The order of the MB filter was set as 375 samples (1.5 μs), corresponding to a cutoff at the half-transmission frequency of 3.4 MHz. The CFD filter was defined with a delay of 480 ns and a pulse-height fraction of 0.4, which was relevant to obtain the best possible time-stamp. The APD signals were shifted so that the CFD time-stamp was $k_{CFD} = 2200$ (8.8 μs). For trigger discrimination a threshold above remaining noise level was applied to the MB signal.

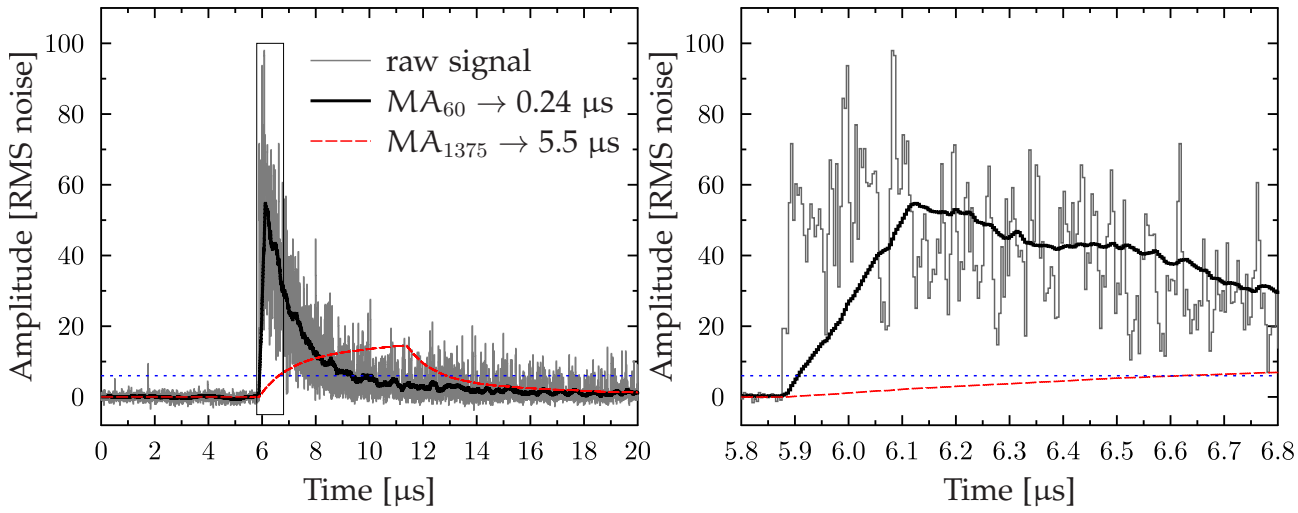

Figure 3.9: Typical PMT raw signal after baseline subtraction (thin solid nine) the resulting smoothed signal by applying the Moving Average (MA) filter 240 ns long (thick solid line) and the calorimetric signal by applying the MA filter 5.5 µs long (dashed line). The area indicated by the square in the left frame was zoomed in the right frame. The dotted line represents the LET threshold at 6 times the RMS noise of the baseline.

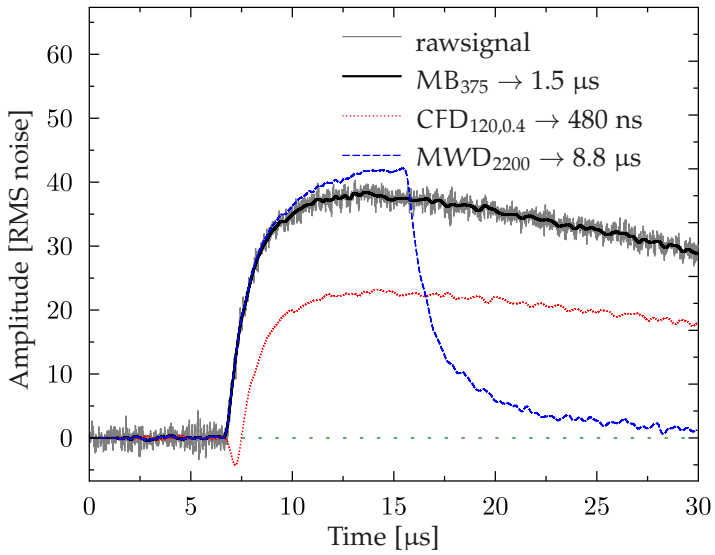

Figure 3.10: Typical APD raw signal passed trough the charge sensitive preamplifier (thin solid line) and after smoothing by applying the MB filter (thick solid line). Together with the result of the CFD (dashed-dotted line) and MWD (dashed line) filters applied to the smoothed APD signal.

3.3.2 Calorimetry

The energies of the PMT events were calculated by integrating the detectors current pulse signals. A MA filter was applied to compute the integration. The amplitude of the resulting MA signal is proportional to the raw signal area under the precedent N samples defined by the MA filter width. An MA width of N = 1375 samples (5.5 µs) was used to integrate the PMT raw signal. An example of an MA_{1375} calorimetric signal is shown in Figure 3.9. The maximum value reached by the MA

calorimetric signal was then used to obtain the histograms, as illustrated in Figure 3.1. The integral of the signal is proportional to the energy deposited in the detector.

In the case of the APD detector, the integration of the charge collected in the detector is carried out by the charge sensitive preamplifier. Since the signal's are digitised after the charge sensitive preamplifier, the energies of the APD events are proportional to the signals amplitude.

Though, changes in the pulse amplitude (ballistic deficit) might occur due to factors such as temperature, which affect the pulse shape and consequently the rise time of the integrated signals. To remove the dependence of the signal amplitude on the rise time, a Moving Window Deconvolution (MWD) filter was first applied. The energy is then determined by finding the signal maximum inside the MWD window. Because the signal maximum also contains the noise amplitude, creating a small average bias, the MWD filter was applied to the smoothed MB signal instead of the raw signal. The result is shown in Figure 3.10. The two parameters of the MWD filter, width of the moving window N and decay constant τ, had to be adjusted to the characteristics of the APD signal. The width of the moving window was set to 2200 samples (8.8 µs) in order to fully cover the signals rise time. The decay constant τ was set to match the exponential response function of the preamplifier, which was determined from a set of signals recorded with a length of 240 µs at room temperature. The value of τ = 40.5 µs was obtained by fitting a single exponential function to the trailing edge of the principal pulse shape of those signals. The long APD principal pulse shape signal and respective exponential fit are illustrated in Figure 3.11.

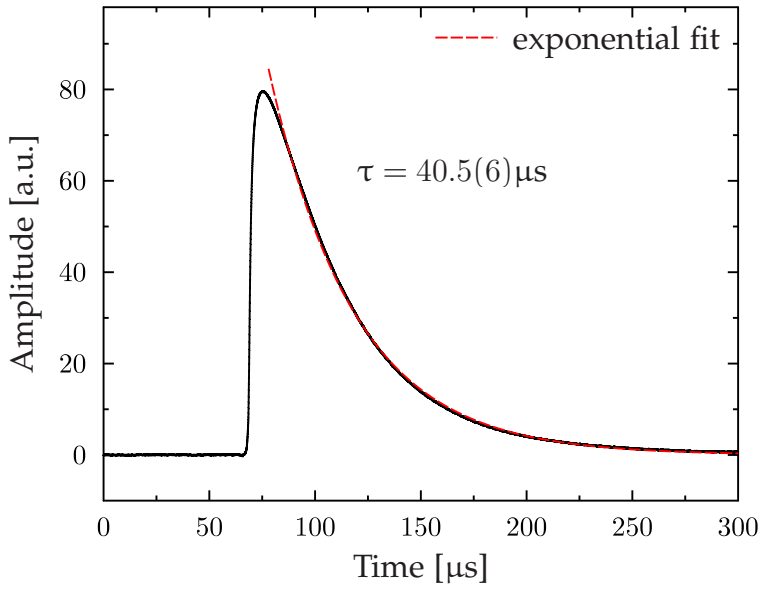

Figure 3.11: Exponential fit to the trailing edge of the principal pulse shape of APD signals recorded with a length of 240 µs. The measured decay constant was used to deconvolute the preamplifier response.

3.3.3 Pile-up rejection

Due to the stochastic nature of the radioactive emission process and relatively slow scintillation of CsI(Tl) crystals, a small fraction of the events appeared distorted due to pile-up, especially at higher count rates. Signals considered distorted due to pile-up were removed from the dataset before performing any kind of pulse shape analysis. To do so, every signal was simultaneously smoothed

and differentiated by applying a Bipolar Moving Average (BMA) filter. The width of the BMA filter was set to 60 samples (0.24 μs) for the PMT signals and to 200 samples (0.8 μs) for the APD signals. Figure 3.12 shows a pile-up example of the BMA signal for both the PMT (a) and the APD (b) detectors. The pile-up discrimination is accomplished by detecting a peak in the BMA signal a second time above the defined trigger threshold, within a hold-off time window characteristic of the signal decay time.

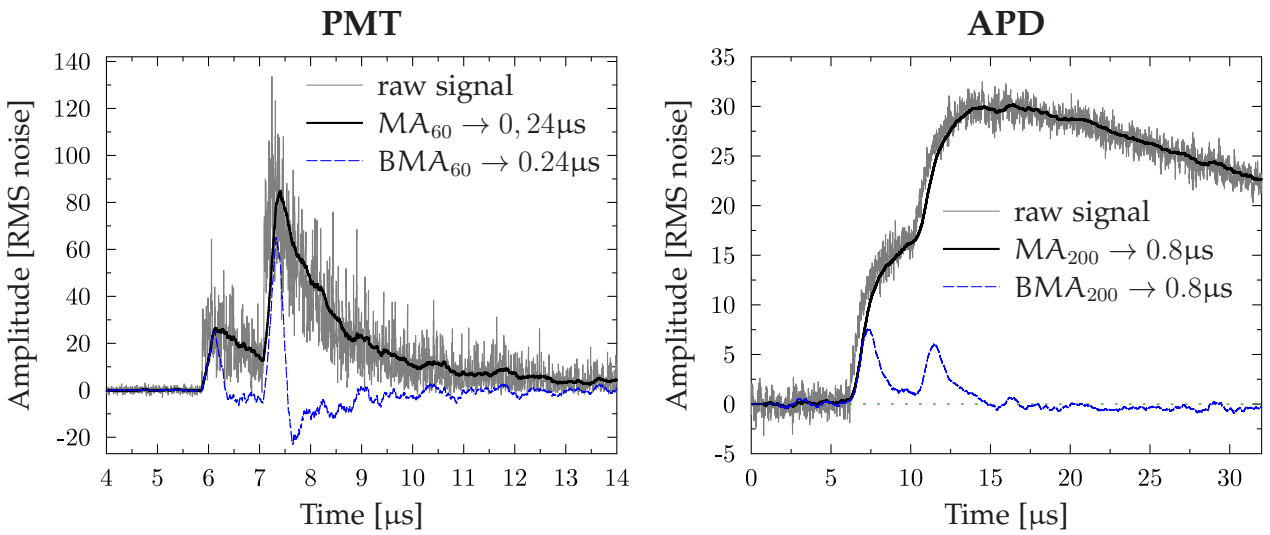

Figure 3.12: Two overlapping signals in a pile-up case (thin solid line), for the PMT (a) and the APD (b) detectors, together with the resulting signals after applying the MA (thick solid line) and the BMA (dashed line) filters.

Additionally, PMT signals that the baseline RMS noise was larger than 2σ of the noise distribution of a representative dataset were considered distorted, mainly due to the contribution of the CsI(Tl) long scintillation tail of previews signals.

Following these procedures, in total about 9% of the recorded PMT signals and 14% of the recorded APD signals were considered distorted and were removed from the dataset.

3.3.4 Principal pulse shape

As referred in Section 2.4.1, the pulse shape of single signals is often not a well-defined observable due to the presence of noise and the photon arrival statistics in the scintillation of the CsI(Tl) crystal. This is especially true for photosensors with a fast response such as the PMT. The pulse shape fluctuations of a PMT raw signal are shown in the zoomed area of Figure 3.9, and an APD raw signal is illustrated in Figure 3.10. Therefore, the Principal Pulse Shape (PPS) of a large number of time aligned signals was calculated (using the prescription of 2.4.1) to visualise and analyse the signals pulse shape.

Considering the temperature gain correction experiment, this process was repeated for every temperature dataset. The amplitude of the signals was previously normalised to such that the calorimetric value is equal to unity. Thus, the amplitude of the PPS signal at a constant temperature is invariant regardless of the number of pulses from different energy events present in it. Figure 3.13 illustrates the PPS of 40,000 PMT and the APD gamma-ray signals recorded at three different temperatures. The higher the temperature, the higher the maximum amplitude and lower the decay

time. In the following Section the PPS is employed to derive a shape parameter correlated with temperature.

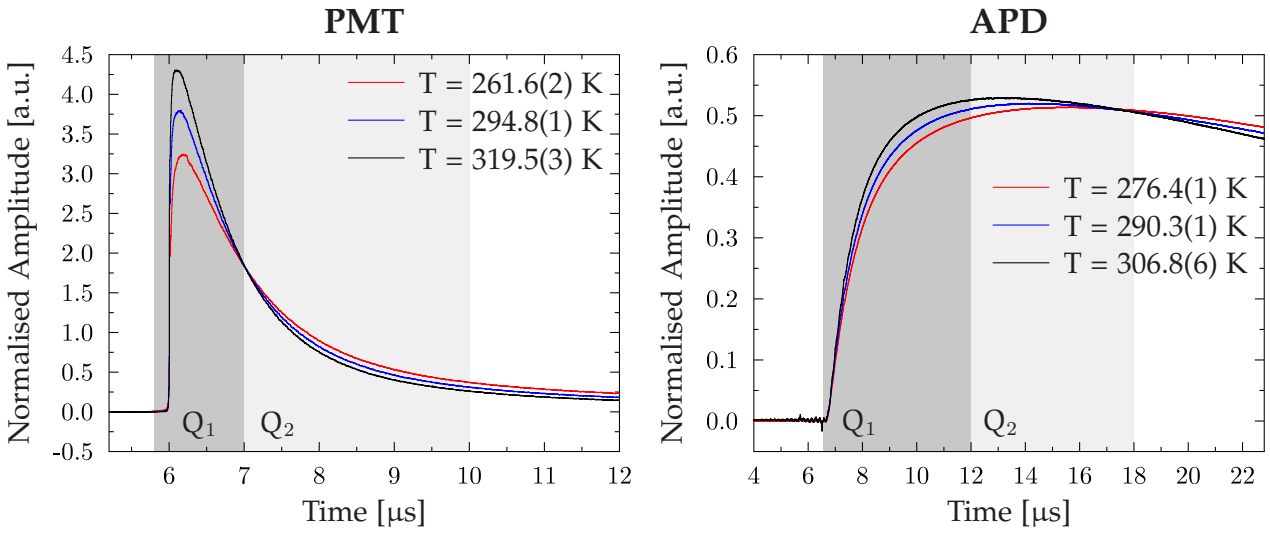

Figure 3.13: PPS calculated by averaging 40,000 signals at three different temperatures. The grey shaded areas mark integration limits used in the integration method. Left frame: PPS obtained using PMT data. Right frame: PPS obtained using APD data.

For the particle ID experiment, more than one particle species and consequently more than one "family" of pulse shapes is present in the dataset, the overall PPS obtained by averaging every signal does not serve as representative pulse shape for any particular particle species. Although, the overall PPS can be used as a reference pulse shape to discriminate individual signals (see Section 3.4.1). The drawback is that the peak positions and widths of each species distribution are not known beforehand.

On the other hand, if the PPS of a particular particle species is required, it is the aim of the fuzzy c-means algorithm to find and group the different pulse shape families. The PPS for each particle species are therefore obtained from cluster centroids returned by the fuzzy clustering process (see Section 2.4.3).

3.4 Temperature gain correction

The following Section presents the methods derived to correlate the pulse shape changes with temperature. These methods were employed to correct the temperature dependence of the detector gain, using the experimental data after being processed as described in Section 3.3.

3.4.1 Pulse shape definitions

In order to correct the temperature gain effects, three methods to derive a parameter based on the pulse shape were proposed. These pulse shape parameters are monotonously correlated with the crystal temperature and can be used to compensate for gain shifts in the detector system. The first method consists of taking the integral over different parts of the signal, which is a common procedure in various pulse shape discrimination approaches (Integration method). The second and third method use the PPS and by means of vector operations compare the PPS of a given dataset to

a reference PPS. While the second method exploits the distance between vectors, the third method exploits the angle between two vectors.

Integration method

It can be observed in Figure 3.13 that the (overall) decay time of the PPS decreases as the temperature increases. Thus, in principle, the decay components may serve as a pulse shape parameter. Though, fitting a function to the pulse characteristics is a rather exhaustive approach. A very simple approach, which is often applied for pulse shape discrimination, is to use the ratio of integrals over different parts of the signal pulse. The differences in the decay time can, therefore, be interpreted as differences in the integral over parts of the signal. The ratio of two integrals

$$\frac{Q_2}{Q_1} = \frac{\sum_{k=a_2}^{b_2} S(k)}{\sum_{k=a_1}^{b_1} S(k)} \tag{3.7}$$

over the regions $[a_1,b_1]$ and $[a_2,b_2]$ was taken to make the value independent of the total integral, and therefore independent of the energy. The distribution of Q_2/Q_1 ratios illustrated in Figure 3.14 shows that for a given temperature it is in fact largely independent of the energy.

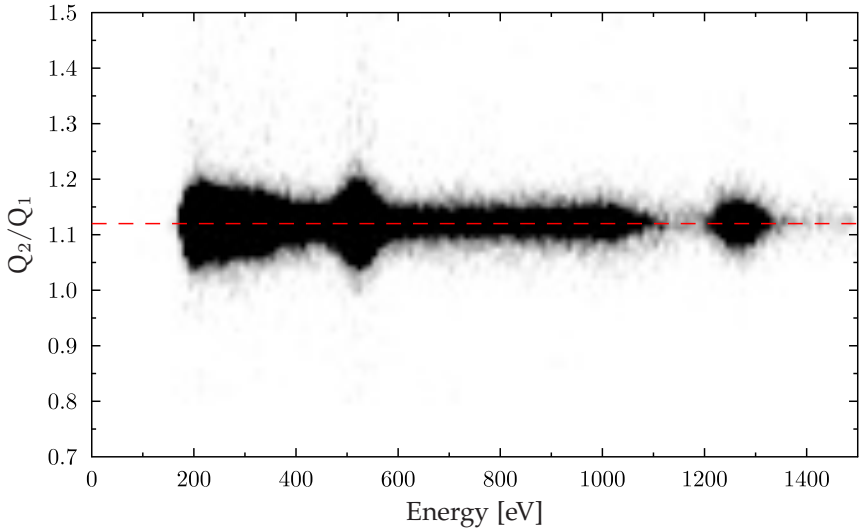

Figure 3.14: Two dimensional distribution of the Q_2/Q_1 ratios as function of the energy from the data recorded at constant temperature.

Normally, to optimise the sensitivity of the Q_2/Q_1 ratio to the changes in the pulse shape, the integration limits have to be adjusted manually to the shape characteristics of the detector pulse signal. The integration limits were chosen so that they cover the regions where the PPS changes with temperature are larger and both regions (Q_1 and Q_2) have identical integrals. The chosen integration regions for the PMT and APD signal are represented in Figure 3.13 by the grey shaded areas.

Figure 3.15 illustrates the histograms of Q_2/Q_1 ratios of single signals both for the PMT and APD detectors at three different temperatures, where each histogram consists of 40,000 entries. Because the pulse shape of individual signals is not well defined, the spread in the Q_2/Q_1 distribution is larger compared to the difference of the peak position at different temperatures; the peak width is

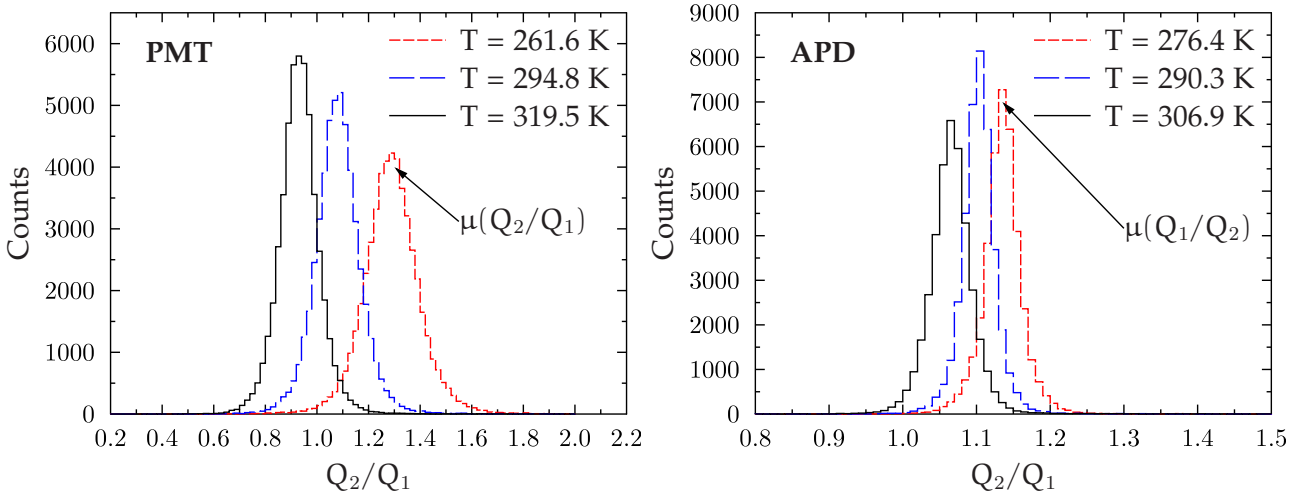

Figure 3.15: Histograms of Q_2/Q_1 ratios of single signals recorded at three different temperatures. Left frame: PMT. Right frame: APD. Each histogram consists of 40,000 entries. Note the different scale for the APD and for the PMT.

a measure of the uncertainty of individual Q_2/Q_1 ratio calculations. Nevertheless, the temperature is usually a slowly changing parameter compared to the rate of incoming events, and so, it is not necessary to determine the pulse shape from single signals. The mean value $\mu(Q_2/Q_1)$ of a set of pulses is therefore sufficient to determine the current pulse shape. The value of $\mu(Q_2/Q_1)$ was estimated by calculating the centre of gravity of the Q_2/Q_1 ratios histogram. Figure 3.16 illustrates the results of $\mu(Q_2/Q_1)$ calculated for all datasets as function of the corresponding temperature. The correlation shows enough precision and dependence of Q_2/Q_1 in order to discriminate even small temperature differences, both for the PMT and APD detectors.

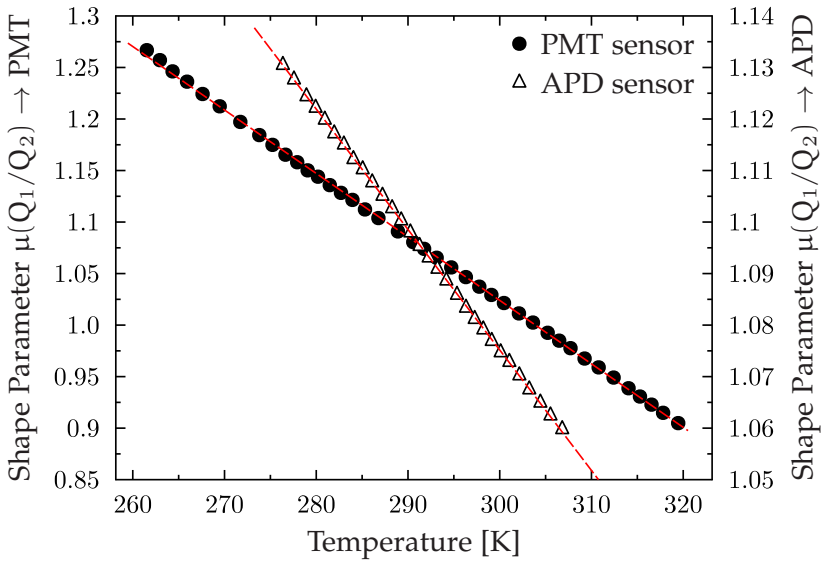

Figure 3.16: The $\mu(Q_2/Q_1)$ calculated from the centre of gravity of the Q_2/Q_1, registered in the scintillator temperature range from 261.6 K to 319.5 using the PMT sensor and in the temperature range from 276.6 to 307 using the APD sensor.

Angle method

As it has already been mentioned in Section 3.2.3, variations in the pulse shape characteristics across different detectors are expected to occur, due to factors such as possible variations in the crystal Thallium concentration (affecting the scintillation characteristics) or due to photosensor-to-photosensor response variations. Varying the Thallium concentration may manifest in differences in temperature dependence of the pulse shape. Since in the integration method the integration limits may have to be tuned to the detector signal characteristics in order to optimise the sensitivity, an approach to quantify the pulse shape changes without the need for manual calibration brings advantages when dealing with large detector arrays containing many CsI(Tl) detectors.

Interpreting the signals as high-dimensional vectors, the information about the amplitude is carried by the vector length while the information about the pulse shape is carried by the vector direction (compare Section 2.4.3). Taking this into consideration, the angle θ between the PPS $\bar{S}_{cur}$ calculated at the current temperature and a PPS $\bar{S}_{ref}$ of a reference temperature can therefore be used as a shape parameter:

$$\theta(\bar{S}_{cur}, \bar{S}_{ref}) = \cos^{-1}\left(\frac{\bar{S}_{cur} \cdot \bar{S}_{ref}}{\|\bar{S}_{cur}\| \cdot \|\bar{S}_{ref}\|}\right). \tag{3.8}$$

For this method, instead of calculating the angle using the full length of the recorded traces, the PPS were cropped to contain a fewer number of samples covering just the relevant pulse region. The PMT PPS were cropped so that 1000 samples (4µs) after k_{LET} were retained, and the APD PPS were cropped so that 125 samples before and 2625 samples after k_{CFD} (a final length of 11µs) were retained. The correlation between the shape parameter $\theta(\bar{S}_{cur}, \bar{S}_{ref})$ and the temperature for both the PMT and the APD detector systems are illustrated in Figure 3.17. Here, $\bar{S}_{ref}$ was set to be the PPS $\bar{S}_{cur}$ recorded at the temperature $T = 319.2$ K and $T = 307.9$ K for the PMT and APD, respectively. The choice of which $\bar{S}_{ref}$ is used as the reference PPS has no influence on the dependence of θ on T. However, for $\theta(T)$ to be an injective function, which is more convenient for further gain corrections, it requires the $\bar{S}_{ref}$ to be recorded at a temperature outside (or at the edge of) the operating range.

Distance method

Another vectorial approach as an alternative to directly measure the angle, is the notion of distance between two signals to distinguish their shapes, which has been proven to be suitable for particle discrimination. Thus, a metric is defined using the Euclidean distance

$$D(\bar{S}_{cur}, \bar{S}_{ref}) = \|\bar{S}_{cur} - \bar{S}_{ref}\| \tag{3.9}$$

between the current PPS $\bar{S}_{cur}$ and the reference PPS $\bar{S}_{ref}$. Since the vector length is influenced by the signal amplitude, the distance approach relies strongly on good normalisation of the signals when producing the PPS $\bar{S}_{cur}$ and $\bar{S}_{ref}$, in order to avoid any energy dependence. Fulfilling the normalisation requirement, the magnitude of the PPS vector can be considered constant for a given temperature. The distance $D(\bar{S}_{cur}, \bar{S}_{ref})$ is then correlated to the opening angle between the $\bar{S}_{cur}$ and $\bar{S}_{ref}$ and so the distance method represents an alternative to the angle method for classifying the pulse shape.

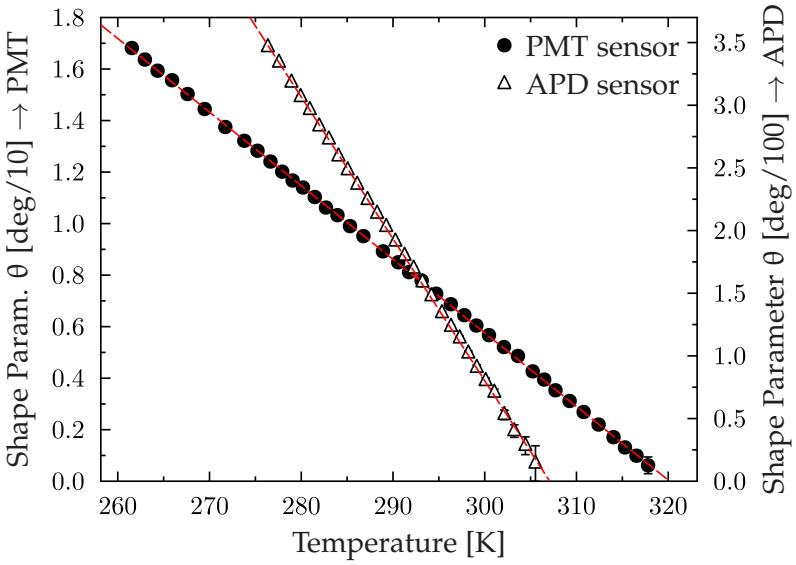

Figure 3.17: Shape parameter $\theta(\bar{S}_{cur}, \bar{S}_{ref})$ plotted versus the temperature. The PPS were calculated from the same signal sets as the $\mu(Q_2/Q_1)$ parameter in Figure 3.16. Note the different scales for the PMT and APD.

Figure 3.18 illustrates the distance $D(\bar{S}_{cur}, \bar{S}_{ref})$ as function of the temperature for both the PMT and APD detector systems. Analogously to the angle method, the $\bar{S}_{ref}$ was set to the PPS $\bar{S}_{cur}$ recorded at the highest temperature. Also, the same cropping procedure was adopted to reduce their number of samples.

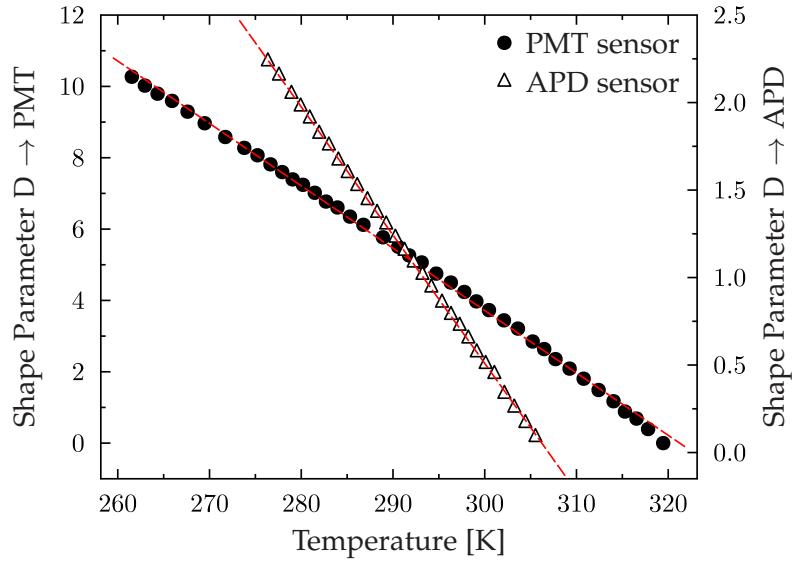

Figure 3.18: Shape parameter $D(\bar{S}_{cur}, \bar{S}_{ref})$ plotted versus the temperature. The PPS were calculated from the same signal sets as the $\mu(Q_2/Q_1)$ parameter in Figure 3.16. Note the different scales for the PMT and APD.

In order to test the energy dependence of the angle and the distance method, the energy spectrum was divided into five energy regions. Then, calculating the PPS for each energy region, both the θ and D parameters were obtained using these PPS with respect to a fixed reference for different temperature datasets. The result of these measurements is illustrated in Figure 3.19, in which

the PPS obtained for the highest energy region of the lowest represented temperature was used as reference. It can be observed that all parameters increase as the temperature raises. However, some scatter is present in the shape parameter across the different energy regions for each temperature dataset, especially at the lower energy regions. This effect tends also to be stronger for the APD detector system. Possible reasons for this energy scattering of the parameters within a constant temperature set are an insufficient number of signals from each energy region to create reliable PPS, a decrease of the signal-to-noise ratio of the signals at lower energy regions or an effect in the pulse shape due to full-energy versus Compton events.

When considering the full available dataset from each temperature measurement, rather smooth and monotonic dependence on temperature was observed in all three pulse shape parameters presented here. This dependence is also stronger than the deviations with the energy regions. Therefore, regarding this condition, the shape parameters indeed serve to determine the current pulse shape and hence can be used as a "thermometer"of the crystal interior to correct gain shifts due to temperature variations.

3.4.2 System gain correction

In the following, the pulse shape parameters defined in Section 3.4.1 were employed to correct the detector gain drifts induced by changes in the ambient temperature.

While the changes of the pulse parameter with the temperature are mainly due to the scintillator temperature variations, the changes in the peak position also include the influence of the temperature on the gain of the PMT and APD photosensors. By assuming a good thermal equilibrium between the photosensor and the crystal via a straight mechanical contact, the overall detector gain and thus the peak positions were considered to be correlated to the changes of the pulse shape parameter.

In order to determine evolution of the system gain drifts, the 511 keV and 1275 keV peak-positions P in the ^{22}Na spectrum were calculated via fitting a Gaussian function to the spectrum peaks from each temperature dataset. The relative peak position $RP = P/P_0$ was defined to describe how much the gain changes relative to a reference peak position P_0. Figure 3.20 illustrates the RP as function of the temperature from both the PMT and the APD detector systems. The value of P_0 was set to be the peak position at the reference temperature $T_0 = 293.2$ K. An overall gain drift of the order of 6% and 74% was observed relative to the maximum gain value registered when using the PMT and APD detectors, respectively. As expected the temperature dependence of the APD sensor is much stronger than for the PMT.

The pulse shape parameters implicitly contain information of the current gain of the system, composed of the scintillator light output and the photosensor gain. Thus, rather than actually determining the scintillator temperature, the correlation between P and a given shape parameter λ (with λ representing either the $\mu(Q_2/Q_1)$, θ or D), can be employed to directly compensate for the detector gain drifts. Once $P(\lambda)$ is known, one can construct the correction factor

$$C(\lambda) = \frac{1}{2}\left(\frac{P_{511}(T_0)}{P_{511}(\lambda)} + \frac{P_{1275}(T_0)}{P_{1275}(\lambda)}\right), \tag{3.10}$$

where $P_{511}(T_0)$ and $P_{1275}(T_0)$ are the reference peak positions of the ^{22}Na gamma-rays at the temperature T_0, and T_0 a suitable reference temperature. The mean relative position of both ^{22}Na

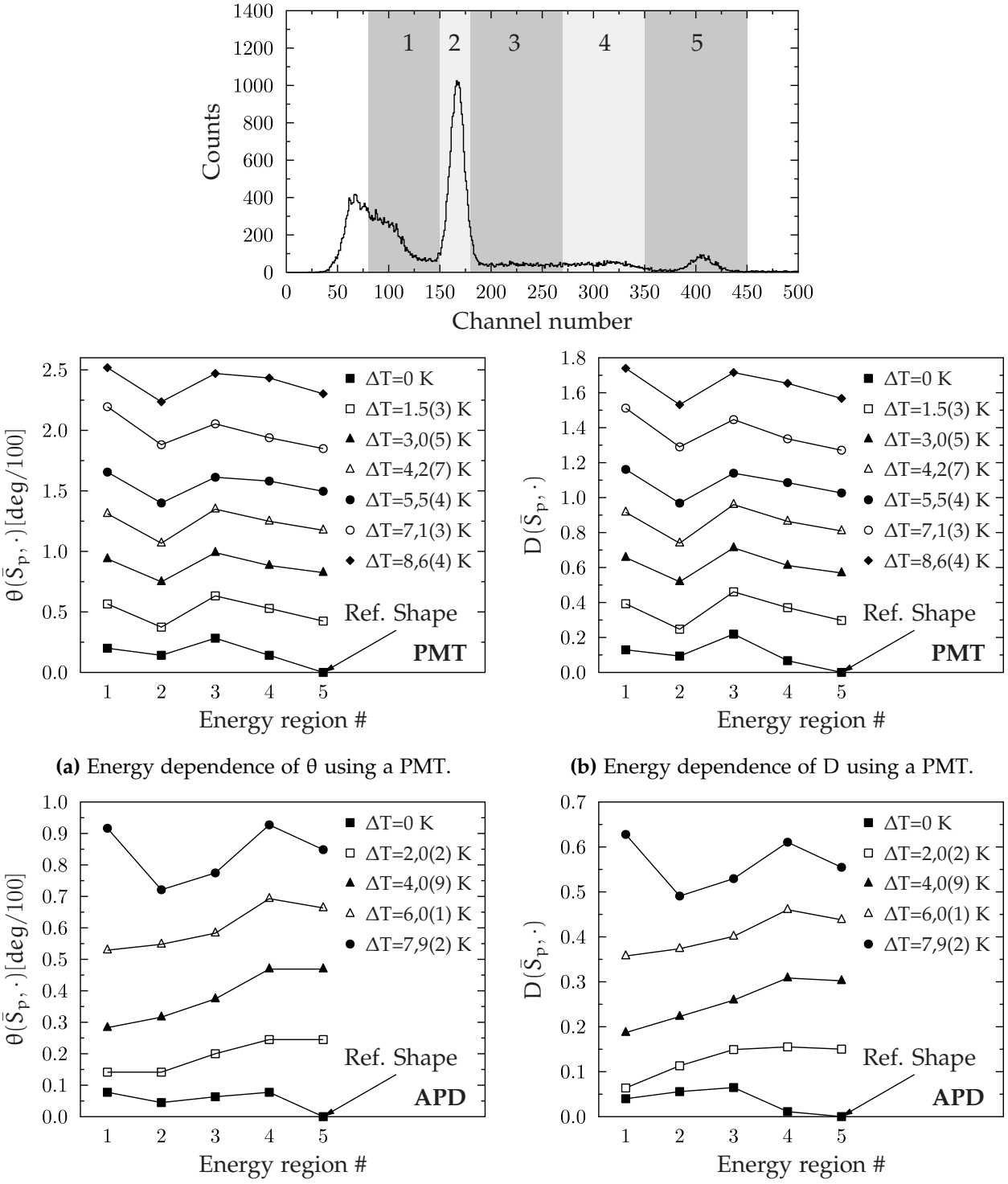

(a) Energy dependence of θ using a PMT.

(b) Energy dependence of D using a PMT.

(c) Energy dependence of θ using a APD.

(d) Energy dependence of D using a APD.

Figure 3.19: Energy dependence of the D and θ parameters across different temperature datasets. The grey shades in the top frame delimit the five energy regions from which the PPS was obtained to the calculated shape parameters illustrated in the frames below. For all cases the PPS at the lowest temperature and the highest energy was used as reference.

gamma-ray peaks was used to minimise the error. The correction factor $C(\lambda)$ shifts the $P(\lambda)$ to $P(T_0)$, therefore corrects the measured calorimetric value CV, representing the gamma energy E, for the

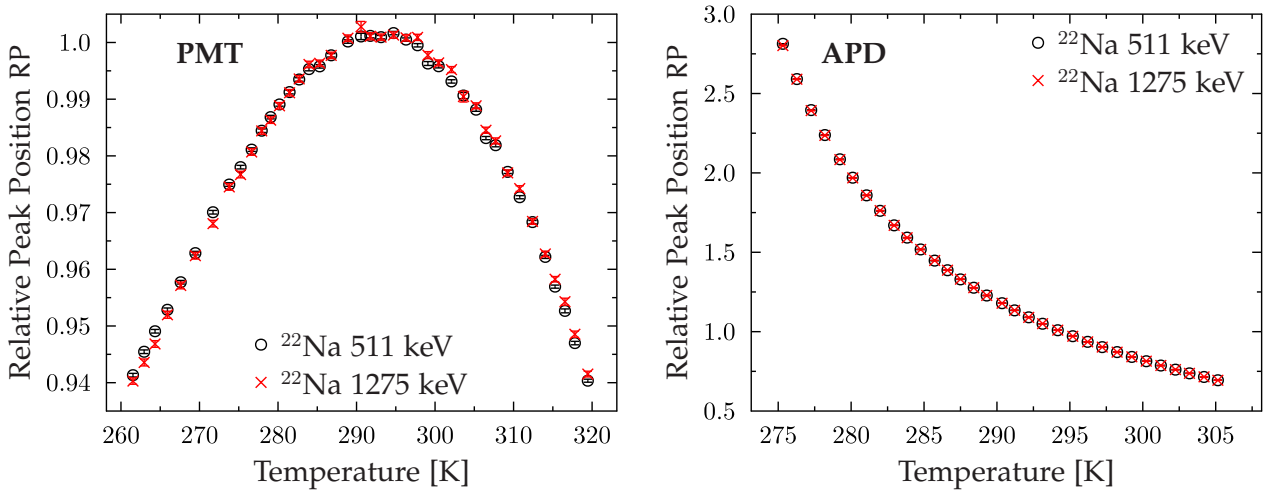

Figure 3.20: Relative peak position with respect to the position at 293.2 K, of the ^{22}Na gamma-ray peaks, as function of temperature. Left frame: PMT. Right frame: APD. Note the different scales.

gain shifts caused by varying temperatures. $C(\lambda)$ was then applied as a multiplier on the CV value of individual pulses: The new parameter

$$E = C(\lambda) \cdot CV \tag{3.11}$$

represents the gamma-ray energy independent of λ, and consequently independent of the detector temperature, if $P(\lambda)$ is a reproducible and well defined correlation in the temperature range of interest. The pulse shape parameters $\mu(Q_2/Q_1)$, θ and D show very similar dependence on temperature. Apart from their scale, the correlations of the relative peak position RP and correction factor C versus one of the parameters (represented by λ) remain somewhat invariant upon considering a different shape parameter λ. Considering that, in the following only the parameter D was taken to demonstrate the feasibility of the correction method. The correlation of RP versus the parameter D along with the corresponding correction factor C according to equation 3.10, are illustrated in Figure 3.21 for the PMT case and in Figure 3.22 for the APD case. In both cases the reference temperature was fixed to T_0 = 293.2 K. In order to obtain a continuous function of the correction factor, the correlation $C(D)$ obtained with the PMT detector was fitted with a third order polynomial (see Figure 3.21), while the correlation $C(D)$ obtained with the APD detector was fitted with a second order polynomial (see Figure 3.22).

In order to demonstrate the method, a second independent dataset was taken with both detector systems in a similar temperature region. While the correction factor $C(\lambda)$ was determined from the first dataset, the events from the second dataset were corrected employing Equation 3.11 to produce the temperature corrected Energy E. Note that the correction factor $C(\lambda)$ is the continuous fitted function, rather than the correlated data points itself or some sort of lookup-table. Figure 3.23 shows the relative peak position of the second dataset as function of the temperature, similarly to that shown in Figure 3.20, after applying the gain shift corrections. The results show that for both detector systems the variations of the relative peak position after correction are reduced down to the order of 1%, which is well below the intrinsic resolution and therefore sufficient for correcting the temperature effects. The typical calorimetric value CV and gain corrected (E) energy spectra,

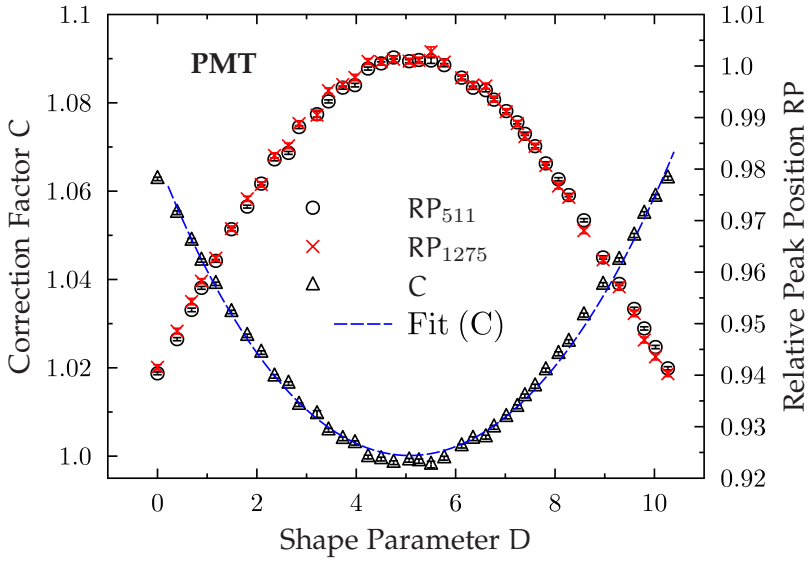

Figure 3.21: Correlation of the relative peak position RP and corresponding correction factor C with the shape parameter D, for the PMT case. The reference peak position $P(T_0)$ was fixed at T_0 = 293.2 K.

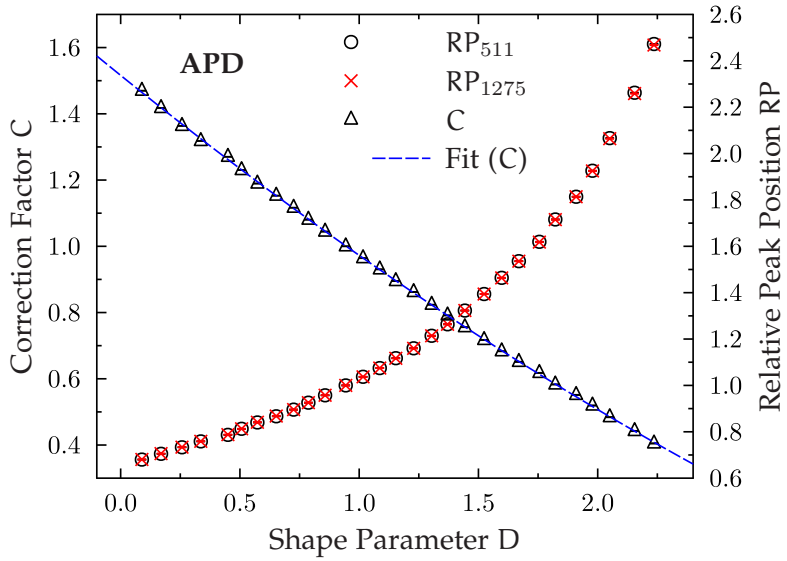

Figure 3.22: Correlation of the relative peak position RP and corresponding correction factor C with the shape parameter D, for the APD case. The reference peak position $P(T_0)$ was fixed at T_0 = 293.2 K.

considering the overall data recorded in the total temperature range from the second dataset, are illustrated in Figure 3.24 for the PMT detector and in Figure 3.25 for the APD detector.

Concerning the PMT detector, the gain variations due the changes in the scintillation yield of the crystal are comparable to the effects of the PMT gain itself. It can be observed in the left frame of Figure 3.20, that the correlation RP(T) reaches a maximum around 293 K and then repeats the gain values; the total gain drift is approximately 6% in the covered temperature range. Figure 3.24 shows that in the case of the PMT, despite the relatively wide temperature range, the peak structure of the ^{22}Na source is preserved in the CV spectrum, with a relative resolution of 66 keV and 115 keV

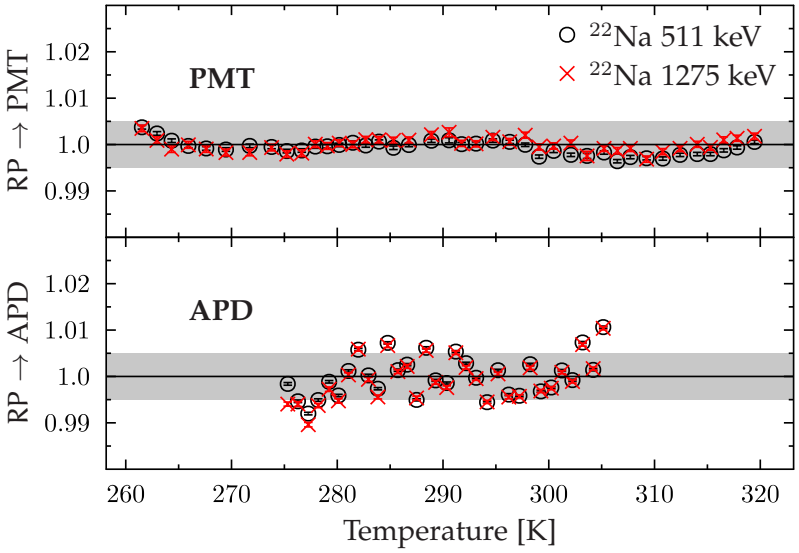

Figure 3.23: The relative peak position RP as function of temperature using a dataset from a different measurement, after applying gain shift correction. The RP was corrected with respect to the position at 293.2 K. The grey shaded area delimits a region of 0.5% deviation from the reference peak position, which is small compared to the typical energy resolution of about 7%. Upper frame: PMT case. Lower frame: APD case.

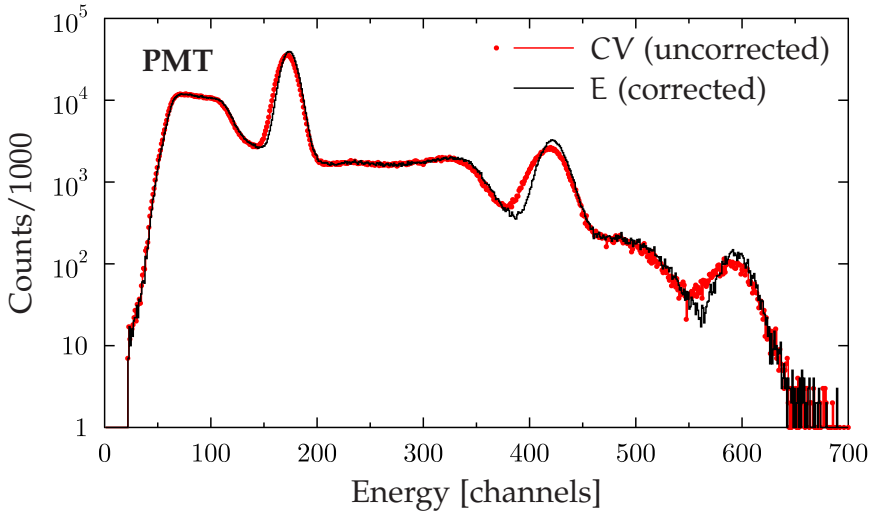

Figure 3.24: Calorimetric value CV and corrected E energy spectra for the PMT detector data.

for the 511 keV and 1275 keV peaks, respectively. After applying the correction, a relative resolution improvement of the order of 24% was obtained in the spectrum E (see Figure 3.24).

On the other hand, in the APD detector the process of light conversion in the photosensor is strongly dependent on temperature (as mentioned in Section 3.2.4), which overwhelms the effects of the light yield variations of the CsI(Tl) crystal relative to the overall detector gain. The uncorrected ^{22}Na spectrum, illustrated in Figure 3.25, shows a smearing out of the ^{22}Na peaks due to strong gain shifts. Nevertheless, a dramatic recovery of the ^{22}Na spectrum was achieved in the corrected spectrum (E) when applying the method described above. Since the shape parameter is not affected

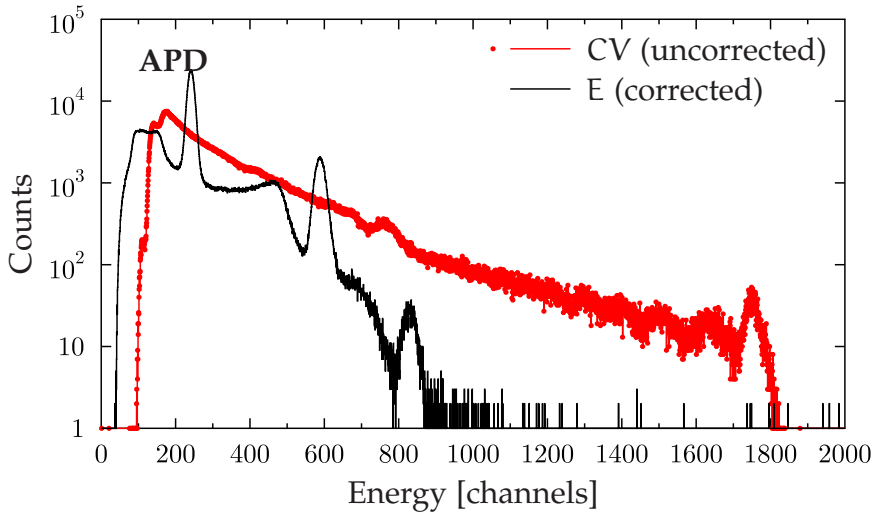

Figure 3.25: Calorimetric value CV and corrected E energy spectra for APD detector data.

by the photosensor gain drifts, the fact that the energy spectrum resolution is restored is evidence for a good thermal equilibrium between the crystal and the APD.

The energy resolution achieved when employing the different previously defined shape parameters considering both the PMT and APD detector systems is summarised in Table 3.3.

Table 3.3: Energy resolution of ^{22}Na spectra after being corrected employing the different pulse shape parameters.

Shape Parameter	Detector type	Energy resolution (FWHM)	
		at 511 keV	at 1275 keV
Reference[1]:	PMT	11.1(8) %	7.2(1) %
Integration ratio	PMT	11.2(5) %	7.3(1) %
Angle θ	PMT	11.2(7) %	7.3(4) %
Distance D	PMT	11.2(7) %	7.3(3) %
Reference[2]:	APD	10.6(9) %	6.5(2) %
Integration ratio	APD	11.3(1) %	6.9(3) %
Angle θ	APD	11.3(9) %	7.0(1) %
Distance D	APD	11.3(8) %	6.9(9) %

[1,2]Spectra measured at constant temperature.

3.5 Particle ID

In the following Section, two PSA methods for achieving Particle IDentification (PID) using scintillation CsI(Tl) crystals are presented. The first method is the integration method, that was already employed in the previous Section to quantify the effect of temperature changes on the pulse shape. The second method uses fuzzy c-means clustering a clustering algorithm to determine the PPS for

each particle species present in the dataset[8]. The results from the clustering process are then combined with two discrimination approaches, that interpret the signals as vectors, to assign the individual signals to the different particle species. The performance of both discrimination approaches are compared to the performance of the integration method.

The present results were obtained using the signals of two neighbouring detector crystals near the centre of the 8×4 array. Because the results of the clustering method tend to deteriorate when the number of signals from each particle species are too different from each other [39], the energy range from 2 MeV to 10 MeV was selected. This energy region is illustrated in Figure 3.26 and contains a comparable number of signals from both species. The signals with energy outside this region were removed from the dataset.

The PID histograms further illustrated in this Section show the results of different investigated methods for two detectors. This allows to compare the effects of different detector responses. To measure how well each method separates the two particle species, a figure-of-merit (FOM) is given in the respective PID histograms. The FOM is defined as

$$\mathrm{FOM} = \frac{|\mu_1 - \mu_2|}{\sigma_1 + \sigma_2} \tag{3.12}$$

where μ_1, μ_2 and σ_1, σ_2 are the means and standard deviations of Gaussian distributions fitted to the peaks of each PID histogram.

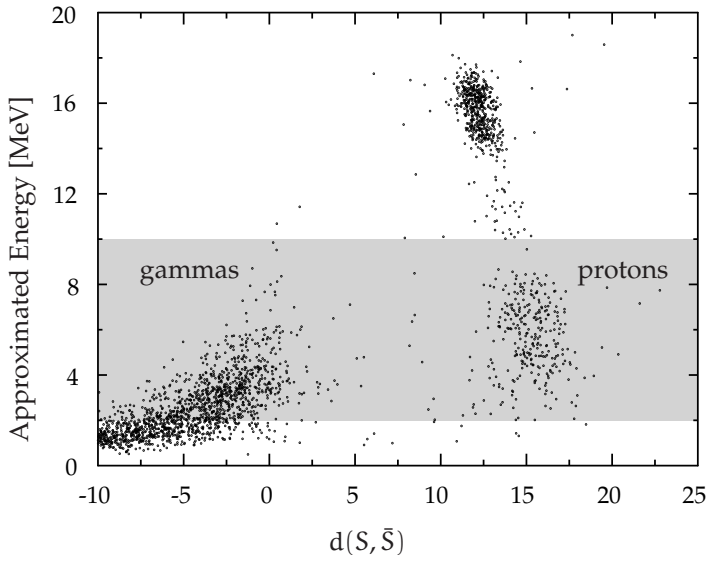

Figure 3.26: Energy of proton and gamma particles deposited in the detector plotted versus the distance d to the overall PPS of the full set (see Section 3.5.2). The distance measure separates well both particle species. The grey shaded region between 2 MeV and 10 MeV delimits the region selected to contain a sufficient number of signals from each particle species.

[8]The data used in this Section was produced using the setup described in Section 3.2.2.

3.5.1 Integration method

As different particle species have different pulse shapes due to distinct processes induced in the scintillator, the integral over different parts of the signal differs also for different particle species. The ratio Q_1/Q_2 over two different non-overlapping regions, as defined in Equation 3.7, was taken to make the value independent of the total integral and therefore suitable for particle identification. The integration limits adopted for the signals of a CsI(Tl) detector with NaI APD readout are illustrated in Figure 3.27, together with the typical normalised (single signal) shape of a proton and gamma induced signals. The areas were set to cover the rising edge region of the signal, which is strongly affected by the difference in the interaction process ionising densities of the two particles.

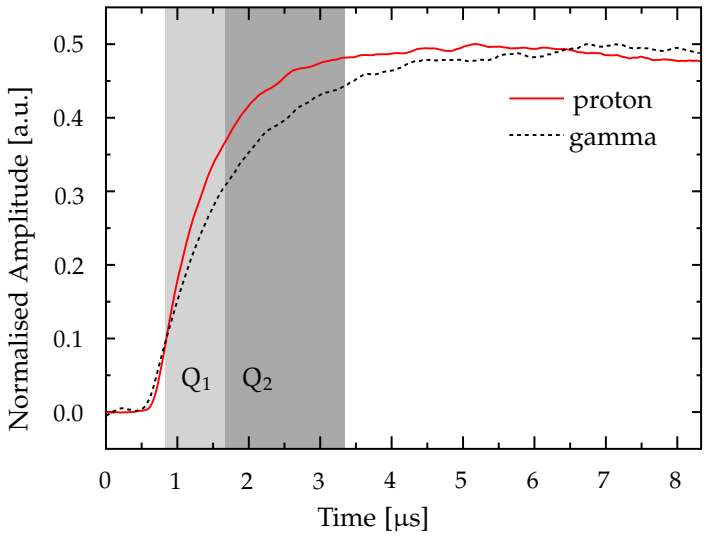

Figure 3.27: Typical single signal shapes, after being normalised and noise filtered, for protons and gamma-rays of a CsI(Tl) crystal readout by an APD photosensor. The grey shaded areas delimit the integration regions used in the integration method.

When producing the histograms of the Q_1/Q_2 ratios, each particle species produces a peak at their characteristic Q_1/Q_2 ratio mean value. Cuts can then be applied to distinguish the different particles. In general for good identification results, the integration limits have to be adjusted to the detector signal characteristics. Figure 3.28 illustrates the Q_1/Q_2 histograms for two different detectors calculated using the limits defined in Figure 3.27. The peaks in the two histograms have different positions when comparing the same particle species for the two detectors. These positions cannot be predicted beforehand and have to be determined by manual intervention or by fitting procedure. The FOM for the two detectors is also given in Figure 3.28. The value for Detector 1 is significantly smaller due to its wide proton peak in the histogram.

3.5.2 Fuzzy clustering

In the fuzzy clustering method, particle identification is achieved by comparing the detector signals with the PPS (i.e. prototype signals obtained from the clusters centroid) of each particle species. These PPSs do not need to be constructed manually, but can be automatically derived from a mixed dataset containing a large enough number of signals representing the different particle species. In

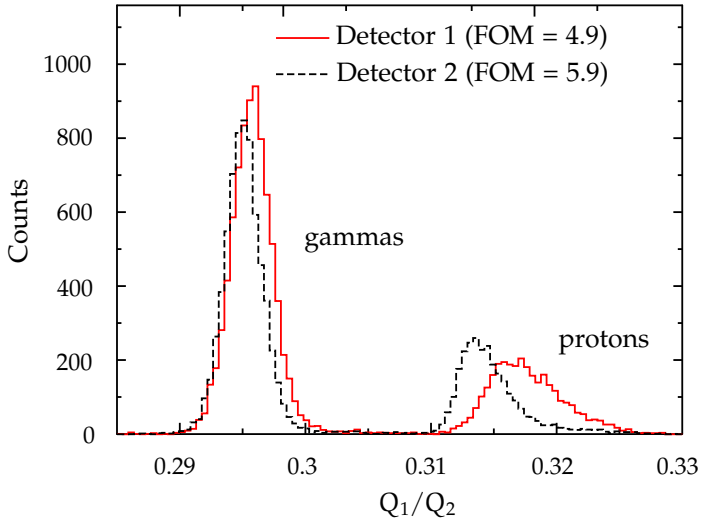

Figure 3.28: Histogram of Q_1/Q_2 ratios from a dataset containing proton and gamma induced signals, for two different detectors. The peaks are well separated, but due to different characteristics of the pulse shape for the two detectors their positions differ slightly in both detectors.

the present work only two particle species were detected, gammas and protons, which reduces the clustering algorithm to the two cluster case. representing the gammas and protons respectively. The fuzzy clustering method can be interpreted as a two step procedure, with the derivation of the PPS as a first step and the assignment of the individual signals to particle species as a second step.

To perform the first step, the fuzzy c-means algorithm was applied to the dataset. A more detailed explanation of the fuzzy c-means algorithm has been given in Section 2.4.3.3. This algorithm returns the PPS $\bar{S}_j$, determined by the cluster centroids, for each particle species and the matrix of membership values u_{ij} designating the degree of membership of every signal S_i to each cluster $\bar{S}_j$. As a second step, the clustering results ($\bar{S}_j$ and u_{ij}) were used to distinguish the signals from the different particle species.

In principle, the degree values of membership can be used themselves to perform particle identification. Although, the peaks in the distribution of these values are strongly non-Gaussian and have different positions depending on the fuzziness parameter m [39], which makes this approach difficult to compare with the results of other PID methods. Therefore, different ways for achieving particle identification using the results from the clustering process are preferable. In the following two discrimination approaches to perform particle identification are presented: One approach uses the concept of the distance between pulse shapes. The second approach makes use of the clustering information to determine a weighting vector characteristic of each pair of particle species, that by means of a scalar product with the detector signal is used to assign a discrimination value to every signal from the dataset.

Distance approach

The notion of distance between two signals can be used to perform particle identification in a similar way as shown before in the case of the temperature correction. After normalising the individual signals, to remove the dependence of their amplitude on the energy, the distance between two signal

pulses is only sensitive to the difference in their shapes. Therefore, a discrimination value based on the distance between the shape of individual signals S and the PPS $\bar{S}_{1,2}$ of one of the particle species can be calculated to distinguish the different particle species. The most natural choice to calculate the distance between two vectors would be the Euclidean distance, as it was employed in Section 3.4.1 to discriminate PPS at different temperatures. However, single signals contain noise that accumulate when calculating the Euclidean distance, which might significantly increase the distance between otherwise similar signals. In order to circumvent this problem, an alternative distance measure is defined as

$$d(S, \bar{S}_j) = \sum_{k=0}^{L} (S(k) - \bar{S}_j(k)), \tag{3.13}$$

which allows for the noise contribution to cancel among the different samples. The parameter L refers to the length of the signal in samples. For the distance approach the recorded signals were cropped so that only L=500 samples (8.33 µs) are retained and the signals begin 50 samples (0.83 µs) before t_0 determined via CFD timing (Figure 3.27 shows two cropped traces). The distance d was then calculated to obtain a discrimination value for each single signal. In order to normalise these discrimination values also the distance between the PPS of each pair of particle species, $d(\bar{S}_1, \bar{S}_2)$, can be calculated. This is advantageous because both species can be assigned with the values zero and one, respectively:

$$\hat{d}(S, \bar{S}_1) = \frac{d(S, \bar{S}_1)}{d(\bar{S}_1, \bar{S}_2)}. \tag{3.14}$$

Figure 3.29 illustrates the normalised distance $\hat{d}$ histograms for the same dataset as in Figure 3.28. As expected, the peak positions corresponding to the protons and gamma-rays are situated around zero and one, respectively. The peak positions are also identical for both detectors, even though the pulse shapes of the two detectors are slightly different. This leads to different distributions in the Q_1/Q_2 histograms (see Figure 3.28). Compared to the integration method the FOM is identical, however the distance approach does not require prior knowledge of the pulse shape characteristics and has the advantage of having fixed peak positions in the PID histogram. Therefore the distance method is better suited for unsupervised calibration of large detector arrays with many channels.

One particular property of defining the distance d in such manner, is that the distance between three signals are closely linked:

$$d(S_1, S_2) = \sum_{k=0}^{L} (S_1(k) - S_2(k)) \tag{3.15}$$

$$= \sum_{k=0}^{L} (S_1(k) - S_3(k) + S_3(k) - S_2(k)) \tag{3.16}$$

$$= d(S_1, S_3) + d(S_3, S_2). \tag{3.17}$$

The choice of a different reference signal to calculate the discrimination values only results in a constant shift of their histogram peaks. Exploiting this property, one can circumvent the need of performing clustering in the two-species case. The overall PPS $\bar{S}$ (i.e. considering the all dataset)

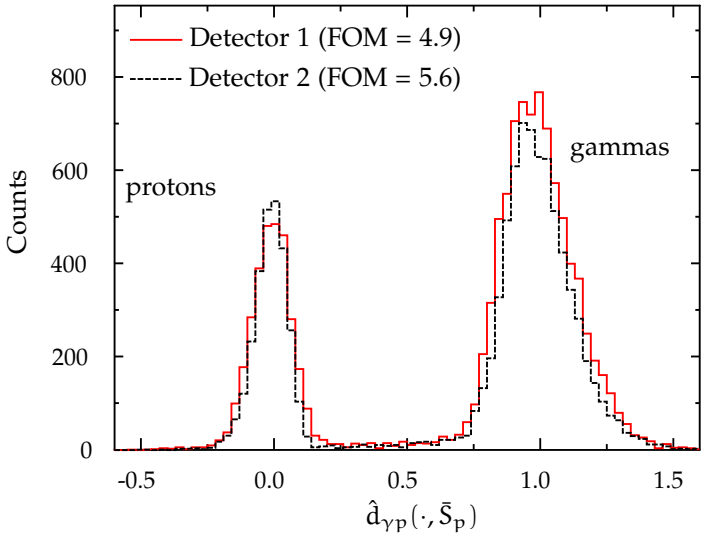

Figure 3.29: Histogram of the normalised distance $\hat{d}$ to the proton PPS $\bar{S}_p$. The distance $d(\bar{S}_\gamma, \bar{S}_p)$ between gamma and proton PPS were used as normalisation value. The position of proton and gamma peaks are situated around the distribution values of 0 and 1 respectively and are identical for both detectors.

can be used instead of determining the PPS for each particle species. Additionally, no care has to be taken regarding strong asymmetries in the number of each particle species present in the dataset. The result of this approach is illustrated in Figure 3.26 and was used in order to select the energy region over which the clustering method was performed. It shows that the distance measure separates both particles well. The disadvantage is that, compared to using clustering PPS as reference signal, in this approach the peaks positions and widths can no longer be known beforehand.

Weighted integration approach

Instead of performing the distance approach, the results from the clustering algorithm can be employed to calculate statistical quantities that, based on linear discriminant analysis, are used to determine a "linear classifier" [86]. A linear classifier achieves particle identification by making a classification decision based on the value of a linear combination of the signal characteristics.

In order to obtain good discrimination of the signals from the different particle species, a measure of the standard deviation for each cluster is required to quantify the difference between their PPS, when determining a linear classifier. Using the matrix of membership values u_{ij} and cluster centroids $\bar{S}_j$, the within-cluster scatter per sample k can be calculated as:

$$\Delta_j^2(k) = \frac{1}{U_j} \sum_{i=1}^{N} u_{ij} (S_i(k) - \bar{S}_j(k))^2, \tag{3.18}$$

with the total cluster size $U_j = \sum_{i=1}^{N} u_{ij}$. Thus, $\frac{\Delta_1^2 + \Delta_2^2}{N}$ is an estimate of the variance of the dataset, and $\Delta_1^2 + \Delta_2^2$ is the total within-cluster scatter of the signals. The information obtained from the clustering facilitates the use of an improved integration method. Rather than having to set the integration regions by hand, the prototype signals $\bar{S}_j$ and Δ_j^2 can be used to calculate a

vector of weights (i.e. a linear classifier) aiming at the largest difference where the PPS of the two particle species under consideration differ the most with respect to their variance Δ_j^2. As there is a considerable scatter inside each cluster, the widths of both signal distributions have to be taken into account. A vector of weights

$$W = \frac{\bar{S}_1 - \bar{S}_2}{\Delta_1^2 + \Delta_2^2}. \tag{3.19}$$

is then obtained by relating the difference between the two PPS $\bar{S}_1$ and $\bar{S}_2$ to the total within-cluster scatter $\Delta_1^2+\Delta_2^2$. Figure 3.30 illustrates the vector of weights W calculated for the two detectors. It is obvious, that the results for the two detectors are different, which shows the adaptive nature of this unsupervised procedure.

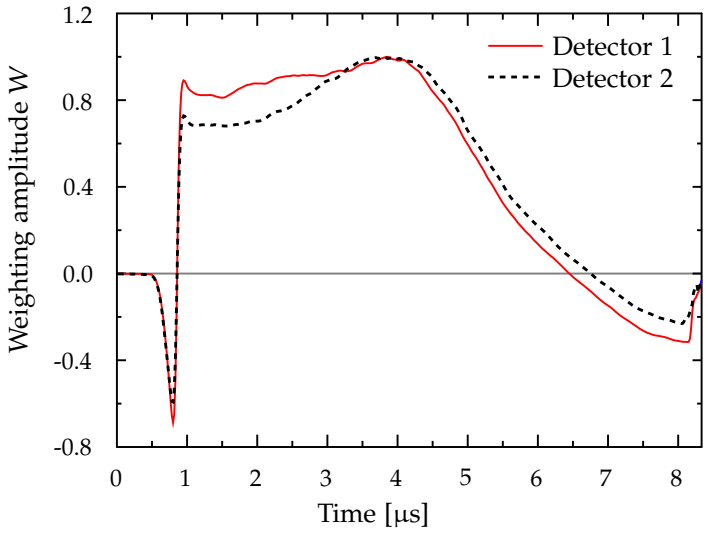

Figure 3.30: Plot of the weighting values obtained from Equation 3.19 for two detectors. The weighting values emphasise the signal regions where the PPS of the two particle species differ the most.

By calculating the scalar product between the signals $S(k)$ and the vector of weights $W(k)$, a discrimination value for each pair of particle species

$$\alpha(S) = S^T W = \sum_{k=0}^{L} S(k)W(k), \tag{3.20}$$

with L being the length of the cropped signals in samples, can be assigned to each signal from the dataset. This step can be interpreted as a weighted integration, in which the regions where the signals are more similar contribute less. Note that in contrast to the integration method (Q_1/Q_2), every signal had to be previously normalised to remove energy dependence. The discrimination value α can also be calculated for the PPS of each particle species. Thus, the discrimination values can be normalised so that a value of zero and one is assigned to both particle species PPS respectively:

$$\hat{\alpha}(S) = \frac{\alpha(S) - \alpha(\bar{S}_1)}{\alpha(\bar{S}_1) - \alpha(\bar{S}_2)}. \tag{3.21}$$

By definition, the peak positions in the discrimination value histogram corresponding to the PPS of the two particle species are now $\hat{\alpha}(\bar{S}_1) = 0$ and $\hat{\alpha}(\bar{S}_2) = 1$. Figure 3.31 illustrates the histogram of

the normalised discrimination values $\hat{\alpha}_{ij}$, where the peaks situated around the positions zero and one correspond to the protons and the gamma-rays, respectively. The distribution peak positions and peak widths are also similar for both detectors. Compared to the distance approach the FOM has improved, which was expected since the weights vector explicitly focuses on the regions of largest distance between the clusters, taking statistical fluctuations into account. This shows that the approach of defining a vector of weights without prior knowledge of the pulse shape characteristics gives good results.

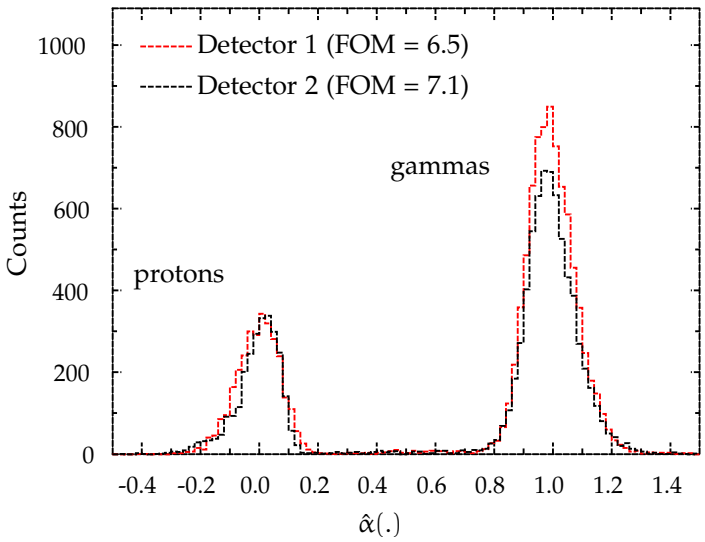

Figure 3.31: Histogram of the normalised discrimination values $\hat{\alpha}_{ij}$ for both detectors, obtained using the weighted integration approach. The values were calculated from the same dataset in Figure 3.28 and in Figure 3.29. The proton and gamma peaks are situated near zero and one respectively, and are identical for both detectors.

The procedure to obtain the discrimination values can be interpreted as a special case of the Fisher's linear discriminant method for vanishing covariance between sampling points, described in [38]. Because the signals were initially filtered to reduce the noise, which leads to significant correlation between neighbouring sampling points, this assumption is not rigorously true. However, the results provided an excellent way to distinguish the two particle species in an unsupervised fashion.

Chapter 4

Performance studies of the Active-Target detector for the R^3B setup

The following chapter presents the functionality tests of the Active-Target (AcTar) prototype for the R^3B (Reactions with Relativistic Radioactive Beams) setup. This detector is an ionisation chamber designed and built for studying elastic and inelastic scattering of light to heavy nuclei on helium and proton targets. As a proof of principle, a ^{58}Ni beam at 700 MeV/u was impinging on a He-H_2 (3%) target mixture.

The preliminary results obtained during the in-beam experimental test are presented. The detector data was fully recorded in a raw format of signals wave form. All the useful information was extracted in post-processing digital signal analysis. Deeper analysis, including the information of other detector systems involved, are still required for physical conclusions.

4.1 Introduction

Reaction and structure studies of exotic nuclei pose unique experimental challenges, which emerge both from the constraints imposed by the production of such nuclei and from tools required to explore their properties. Exotic nuclei are typically produced with low intensities, which demand for a detection system with very high efficiency. Moreover, the information on the nuclear structure is more promptly extracted using nuclear reactions where one of the participants exhibits a relatively simple structure, e.g. ^{1}H and ^{4}He. A promising solution for such experimental challenges is the use of an active-target detector.

The AcTar is a relatively novel gaseous ionisation detector concept, in which the gaseous target is no longer the inert material, but also constitutes the recoil detection medium. This allows to efficiently detect very slow recoil particles in scattering reactions at low momentum transfer, without the need for the recoil particle to leave the thick target. Compared to conventional solid targets, the AcTar detector allows the use of much thicker targets increasing the luminosity without loss of resolution. Different target thicknesses are achieved by controlling the filled gas pressure.

Gas detectors provide a most unique way for identification and good resolution of low energy recoil particles together with high efficiency. The working principle of such detectors is commonly characterised as Charge Projection Chamber analogous to the Time Projection Chamber (TPC) used in particle physics experiments.

The concept of the AcTar prototype is an advanced version of the IKAR detector [8, 87] developed at PNPI[1] and successfully used in experiments [9, 88] with radioactive ion beams (Radioactive Ion Beam (RIB)) in inverse kinematics for measuring the elastic scattering cross Sections at high energies (1 GeV/u) of light nuclei at GSI Helmholtzzentrum für Schwerionenforschung GmbH (GSI). The AcTar is mostly meant to be used in inverse kinematics, filled with target gas composed of ^{1}H, ^{2}H and ^{4}He, either pure or mixed with standard detection gases such as C_4H_{10}. The recoil gas particles have very low energy with the most important centre-of-mass angles occurring at near zero degree in elastic and quasielastic reactions.

A similar detector concept, the MAYA[11] detector, was recently built at the GANIL[2] facility, where it has been used to measure different types of direct reactions at low energies (< 50 MeV/u). Although this detector has proven the feasibility of the active target concept, it has limited dynamic range, position and multi-track resolution.

In the present work the AcTar detector has been subject of test as integral part of a complex beam experimental setup with the objective of investigating its suitability for the construction of the ionisation chambers for the R^{3}B project. The main aim of the experiment was to prove the possibility of reliable detection of recoiling particles in scattering reactions with a 700 MeV/u ^{58}Ni beam. Although that for a physical case lower beam energies (< 300 MeV) would be more suitable to study ^{58}Ni nuclei with AcTar, higher energies were used to allow the beam reach through the target with enough intensity so other detectors could also be tested in parallel.

The modern readout system of the AcTar detector, which includes fast digitisers, has made the fully recorded track information of the recoil particles available. The information of the recoil particles, such as kinetic energy and recoil angle, was extracted by applying different methods for digital signal analysis. The functionality and design of the new detector AcTar will be explained in detail in the following. The preliminary results in attempting to calibrate the detector together with the detection of the scattering reaction products are also presented. The results show, that it is possible to detect and isolate from inelastic scattering events.

The data obtained during the test experiment turn out to be of importance for the construction of an ionising chamber suitable for the R^{3}B project. It is the first time that an active-target of this type has successfully been tested with a ion beam heavier than carbon.

The present analysis are preliminary and involve only data acquired with AcTar, showing the principle functionalities of this detector. The aim of the experimental setup was to study the feasibly and performance of such kind of detector with the use of an heavy ion beam. Further analysis are necessary for the study of physical case studies, which will require an extended calibration of the other detectors involved in the experiment.

[1] The Petersburg Nuclear Physics Institute
[2] Grand Accélérateur National d'Ions Lourds

4.2 Experimental setup

The experiment was performed at the radioactive-beam facility of GSI Darmstadt. A primary ^{58}Ni beam was extracted from the heavy-ion synchrotron (SIS) at an energy of 700 MeV/u. The beam intensity was around 5×10^3 s^{-1} with a duty factor of ~25% – 50%.

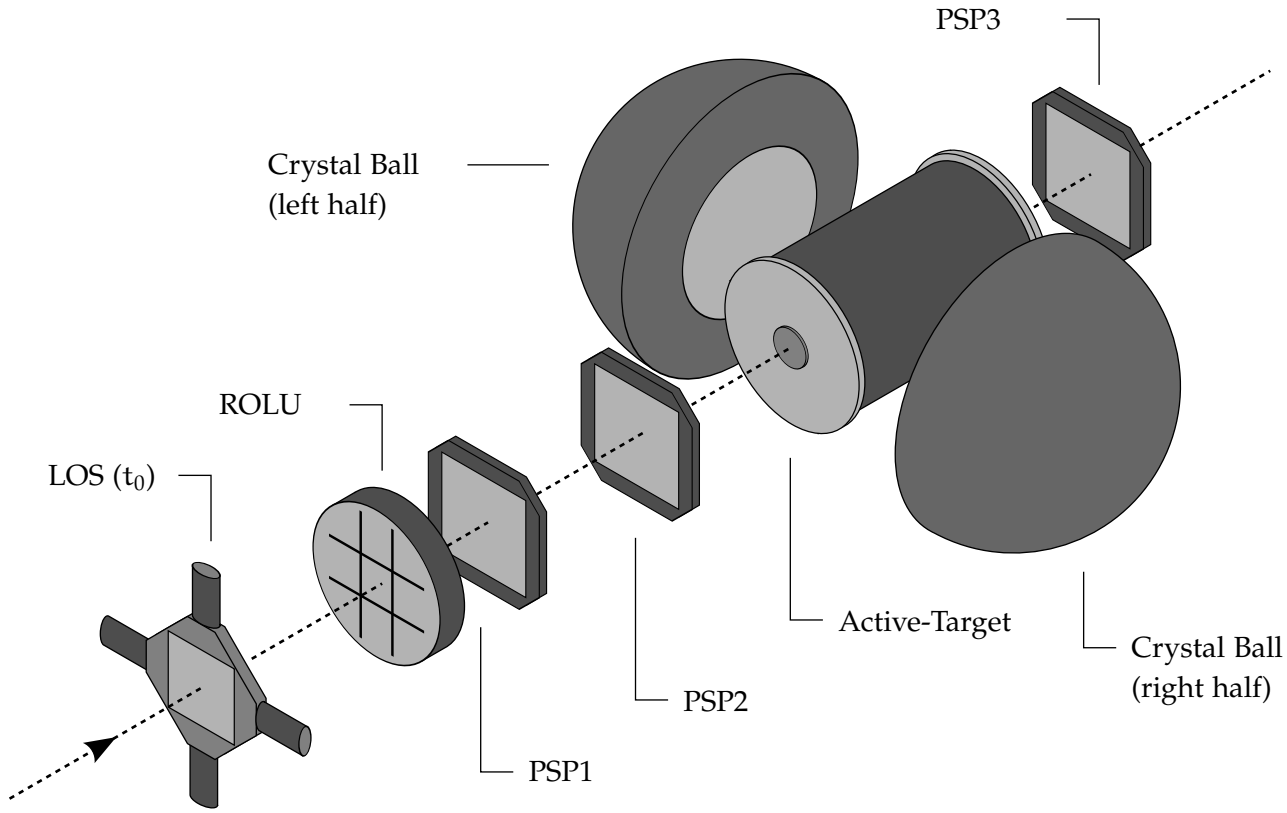

Figure 4.1: Schematic view of the setup for testing the AcTar prototype using alpha elastic scattering on ^{58}Ni nuclei in inverse kinematics. The AcTar serves simultaneously as a gas target and a detector for the recoil alpha particles. The forward spectrometer consisting of three position sensitive silicon pin diodes (PSP1–PSP3) determine the scattering angle of the beam particle in the target. The scintillation counters (LOS and ROLU) were used for triggering and time reference for the ion passing through the setup.

The schematic representation of the detectors arrangement for the scattering reaction experiment is illustrated in Figure 4.1. The main constituent in this setup is the AcTar, a cylindrically shaped stainless steel gas detector with a diameter of 30 cm and a length of 60 cm. The detector was filled with helium-hydrogen gas mixture containing 3% hydrogen (pure helium cannot withstand the necessary high voltage). For estimating the optimal conditions to detect the recoil particles of different energies, three different operating gas pressures of 10, 5 and 2 bar were adopted during the experiment. Projectile beam particles interact with the gas particles in the AcTar, which serves at the same time as a target and a recoil particle (proton- and alpha particles) detector. The recoil particles registered in the AcTar were measured in coincidence with the scattered ions. With the purpose of determining the track of the incoming and outgoing ions, three tracking detectors were used (position sensitive pin diodes (PSP1-PSP3)). A plastic scintillator was used to provide a fast trigger signal to mark the event start and for time-of-flight measurements. A squared aperture scintillator

(ROLU) was used to limit the accepted beam size, rejecting projectiles that entered the AcTar outside the area of 4×4 mm^2 in a square centred in the central axis. The Crystal Ball (XB) calorimeter was used to detect the emitted gamma rays following the ^{58}Ni inelastic scattering. However, due to the geometrical incompatibility, it was not possible to fully close together both halves of the XB detector in order to cover the full solid angle (see Figure 4.1).

4.2.1 Operating principle and design of the active-target detector

Ionisation detectors constitute one of the oldest and widely used devices developed for radiation detection. The active-target detector is fundamentally a gaseous ionisation detector. This type of detectors is based on the direct collection of the ionisation ions and electrons created in the gas by the passage of radiation.

When a charged particle such as a proton, electron or alpha particle, move through a gaseous medium it loses kinetic energy through collisions with the gas creating ionised atoms along its path. The kinetic energy of the charged particles is lost to ionisation of the surrounding gas via multiple Coulomb interactions [89]. After ionisation of a neutral atom, the resulting free electron and positive ion are called an *electron-ion pair*.

The electron-ion pairs can be created either through direct interaction with the incident charged particle or by a secondary process in which a fraction of the particles kinetic energy is first transferred to a *delta-electron* (or delta-ray). Delta-electrons are energetic electrons which receive enough momentum impulse that after having left its parent atom, they still have sufficient kinetic energy to produce further ions. Delta electrons appear as branches in the primary particle track. These branches will appear near the start of the primary track, where more energy is transferred to the electron.

After the passage of an ionising particle through the gas, the presence of an externally applied electric field avoids the rapid recombination of electron-ion pairs, resulting in the electrons and ions to drift apart towards the outer electrodes. As the charges move in the electric field, they generate an induced current in the electrodes of the ionising chamber that reduces the chamber applied voltage from its equilibrium[3]. A voltage appears then across the anode-cathode load resistance with equal amount by which the high-voltage has dropped. The further from the electrodes the ionisation occurs the longer is the drift time. Since the induced current is generated from the moment the drifting charges are created, the pulse amplitude depends on the location of the primary ionisation. The dependence of the pulse amplitude on the interaction position in the chamber can be removed by installing a Frisch grid [90, 91]. The grid divides the chamber volume into two volumes, in which all the radiation interactions are confined to the volume between the grid and the cathode (see Figure 4.3). The potential of the grid is kept at an intermediate value between the anode and cathode and the grid should be as transparent as possible to electrons. By measuring the signal voltage at the load resistor between the grid and the anode, only when the drifting electrons pass through the grid towards the anode the signal begins to build across the load resistor. Because all electrons now have to pass through the same potential difference between grid and anode, which contribute equally to the pulse formation, the pulse amplitude becomes independent of the position of the primary ionisation and is proportional to the number of electron-ion pairs created along

[3]Equilibrium voltage is the voltage that appears across the ionising chamber in the absence of any ionising charge.

the track of the ionising particle. The electric signal resulting from the drifting charges provides information on the energy of the ionising particle propagating through the detector medium.

Independently of the detailed mechanism involved in the ionisation process, the practical quantity of interest is the number of ion pairs produced along the track path of the radiation. The mechanisms by which the incident particle loses energy in the gas do not always produce ion pairs. There are mechanisms such as excitation processes where electrons are elevated to a higher bound state without being completely removed. Therefore, the value of the energy dissipated by the incident particle (W-Value) is higher than the ionisation energy and is in principle expected to depend on the type of radiation and its energy. However, empirical observation [92] has shown that W-values are remarkably constant for many gases (including H and He). Assuming that the W-Value is constant (for a given type of radiation), the energy deposited in the detection medium is therefore proportional to the number of ion pairs produced and can be determined if the corresponding measurement of ion pairs is performed.

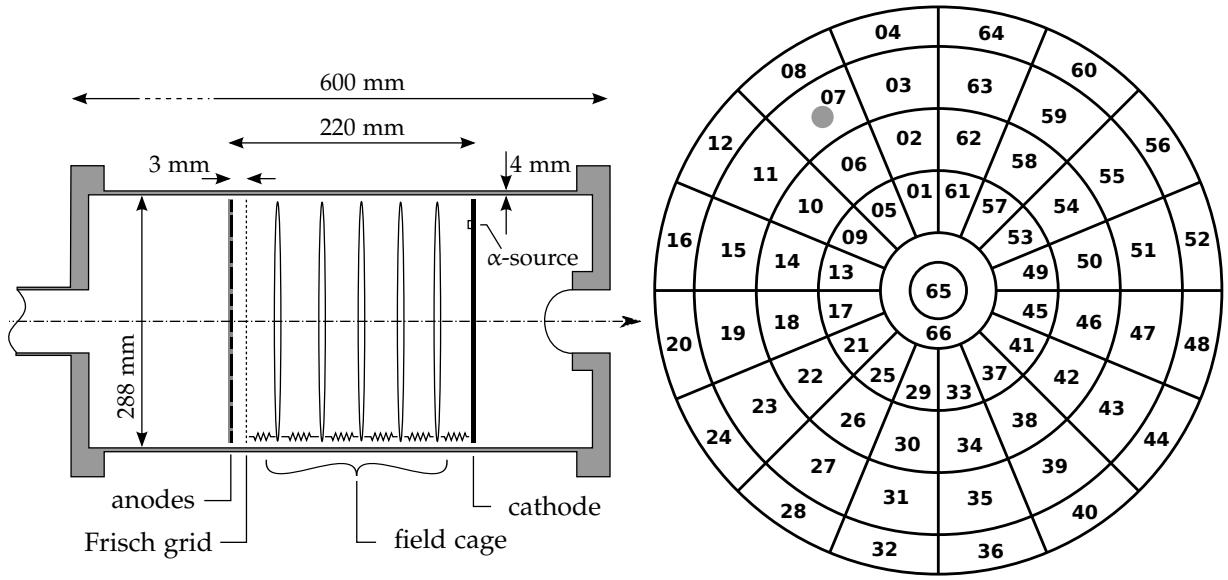

Figure 4.2: Structural representation (not to scale) of the AcTar ionising chamber (Left). Schematic view of the AcTar anode pattern (right). The projection of the alpha-source position in the anode is indicated by the grey dot.

The AcTar detector, schematically illustrated in Figure 4.2 (left), consists of a single axial ionisation chamber with the electric field aligned with the beam direction and with a 2π azimuth's angle acceptance for detection of the recoil target particles. The windows at the entrance and at the exit of the AcTar chamber, which coincide with the beam line, are made of thin Beryllium foils for minimisation of multiple Coulomb scattering and are shaped as semi-spherical shells in order to safely withstand the high operating pressures. The distance between cathode and anode is 22 cm and the distance between the Frisch grid and anode is 3 mm. A cage with voltage dividers constituted of five guard rings placed equidistantly between the cathode and the grid and with the same diameter of the electrodes was used to improve the uniformity of the electric field near the fringe region on the edge of the ionisation chamber.

The pattern layout of the AcTar anode is shown schematically in Figure 4.2. The AcTar anode cell structure consists of five rings and a central circle, see their dimensions in Table 4.1. The four outer

rings are segmented in 16 sectors each, all constituting a total of 66 anode cells. The segmentation of the rings in sectors is intended to reduce the influence of the delta-electrons, i.e. if a delta-electron acquires enough energy to reach the outer rings. The fact that the rings are sectioned in equiangular sectors reduces the probability of pile-up.

Table 4.1: Radial dimension of the AcTar anode rings.

Anode ring #	A0	A1	A2	A3	A4	A5
Outer radius [mm]	10	20	42	64	86	100

For the purpose of energy calibration a reference energy deposited in the AcTar was continuously measured with a low-activity (<10 Bq) ^{241}Am alpha-source, E_α = 5486 keV, placed on the cathode surface in the position facing the centre of cell #07.

When a scattering reaction occurs in the AcTar, a recoil particle is emitted radially with a certain angle relative to the beam direction. Figure 4.3 illustrates a typical scattering event. The projectile nuclei (^{58}Ni) elastically scattered at small angles ($\theta < 1.5°$) pass the AcTar exit window and the corresponding recoil tracks of the emitted alpha particles are almost parallel to the electrode planes. Hence, the recoil particles deposit full energy in the AcTar when their tracks are shorter than the radius of the chamber electrodes. Note that the recoil particle is faster (e.g. alpha particles with kinetic energy of 5 MeV travel at 15 ~ m/μs) compared to the drift velocity of the electrons. As a result the electrons reach the grid with the same relative time difference that they were created. This property is the basis of the recoil angle calculations as it will further be explained in Section 4.5.3.

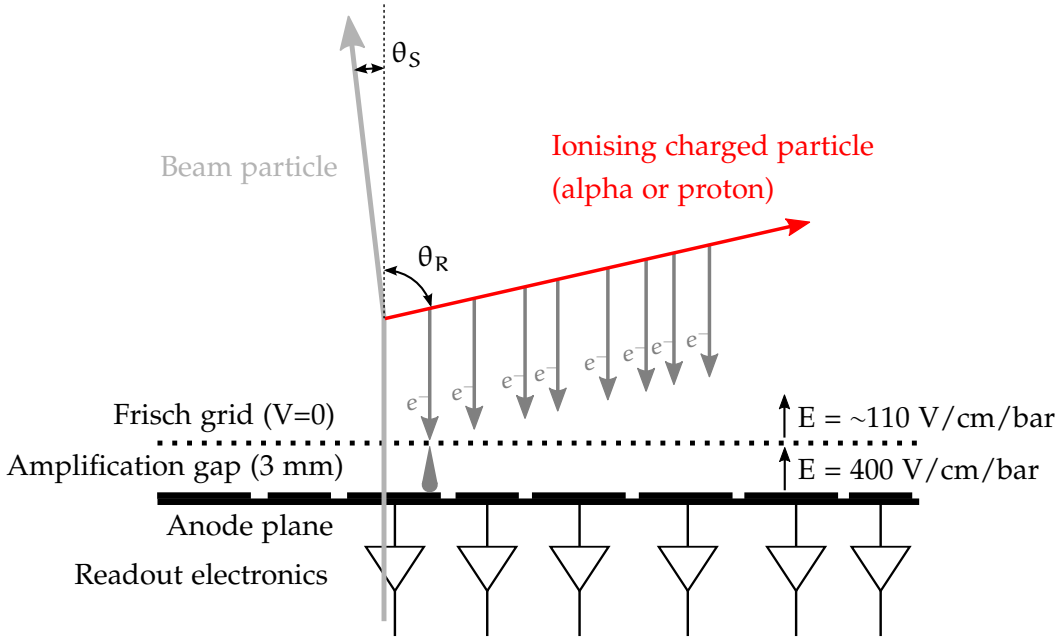

Figure 4.3: Schematic representation of an AcTar scattering event. The electrons produced along the straight track of the fast recoil particle drift at constant velocity towards the Frisch grid keeping the angle profile of the recoil. The current signal is only detected in the anode after the electrons reached the Frisch grid. Note the different electric fields (E) separated by the grid.

The high operating pressure allows to achieve reasonable target thickness and ensures total absorption of the recoil particle energy inside the active volume. On the other hand, the precision of

the recoil angle (θ_r) measurements tend to improve with longer recoil paths. Therefore, in order to retain the particle in the active volume and still have relatively long recoil range, several operating pressures are required to cover different recoil energy ranges.

Depending on the operating pressure (2, 5 or 10 bar) the voltage applied to the anode and cathode was adjusted according to the values of Table 4.2, in order to keep the AcTar electric field proportional to the operating pressure with approximately 110 $Vcm^{-1}bar^{-1}$ between cathode and grid, and 400 $Vcm^{-1}bar^{-1}$ between grid and anode (see Figure 4.3). The grid potential was kept at ground level (0 V). Consequently, the total drift time of the electrons in the chamber was the same for the three operating pressures at around 60 μs.

Table 4.2: Anode and cathode applied voltage.

Pressure	Cathode potential	Anode potential
2 bar	-5 kV	250 V
5 bar	-12kV	600 V
10 bar	-24 kV	1200 V

The signal from all 66 AcTar channels were preamplified and filtered with a 5^{th} order low-pass Bessel filter. The preamplifier output was directly coupled to a set of 16 channels Struck[4] SIS3316 Flash-ADC (FADC) digitisers for parallel read-out and acquisition of the anode signals induced by the drifting electrons. The SIS3316 digitisers have 14 bit resolution and were operated at 25 MSPS (40 ns interval between sampling points).

The AcTar electric field was employed using high-voltage Heinzinger power supply[5] modules. The voltage values in this modules can be set via serial communication, in which a NI[6] CompactRIO control system was implemented to establish a back-end interface for high-voltage modules. The reading of 5 temperature sensors and one pressure sensor was also performed by CompactRIO modules. A slow control interface written in LabVIEW allowed to remotely control high-voltage, as well as, monitor and log the temperature and pressure during the experiment. For additional information on the AcTar slow control refer to Appendix B.2.

4.2.2 Trigger logic and data acquisition

The AcTar detector had implemented its own dedicated Data AcQuisition (DAQ) system, whereas the event correlation with the other detector systems in the experimental setup was performed using a synchronised clock that provided time stamping for posterior event matching.

Since during the present experiment (S438 experimental setup) the beam intensity was about 5 kHz, whereas the event rate of scattering particles in the AcTar was in the order of 10^2 Hz, the data acquisition system was configured to register only those scattering events. Moreover, the time between successive beam particles had to be controlled in order to reduce pile-up events due to the long electron drift time in the ionising chamber, making the AcTar the slowest detector in the setup. To meet these requirements, the trigger logic was comprised of different trigger levels.

[4]Struck GmbH – http://www.struck.de/
[5]Heinzinger electronic GmbH – http://www.heinzinger.com/
[6]National Instruments – http://www.ni.com/

Figure 4.4 shows the diagram of the logic implemented to trigger an event registration in the AcTar DAQ. The trigger of each individual AcTar anode cell was produced in the digitisers while processing the event data stream. The SIS3316 digitiser implements a trapezoidal Finite Impulse Response (FIR) filter which provides a trigger signal for each FADC channel. The trigger threshold of each channel was programmed to be as low as possible without triggering on the baseline noise. An OR gate was applied to the trigger of the 64 AcTar segmented ring channels, i.e. from all cells excluding the two inner most cells, to provide a single trigger acknowledging the detection of a recoil particle (recoil trigger). This trigger, however is not correlated with the arrival time of the beam particle since a scattering reaction can occur at any $z-$position in the AcTar active medium.

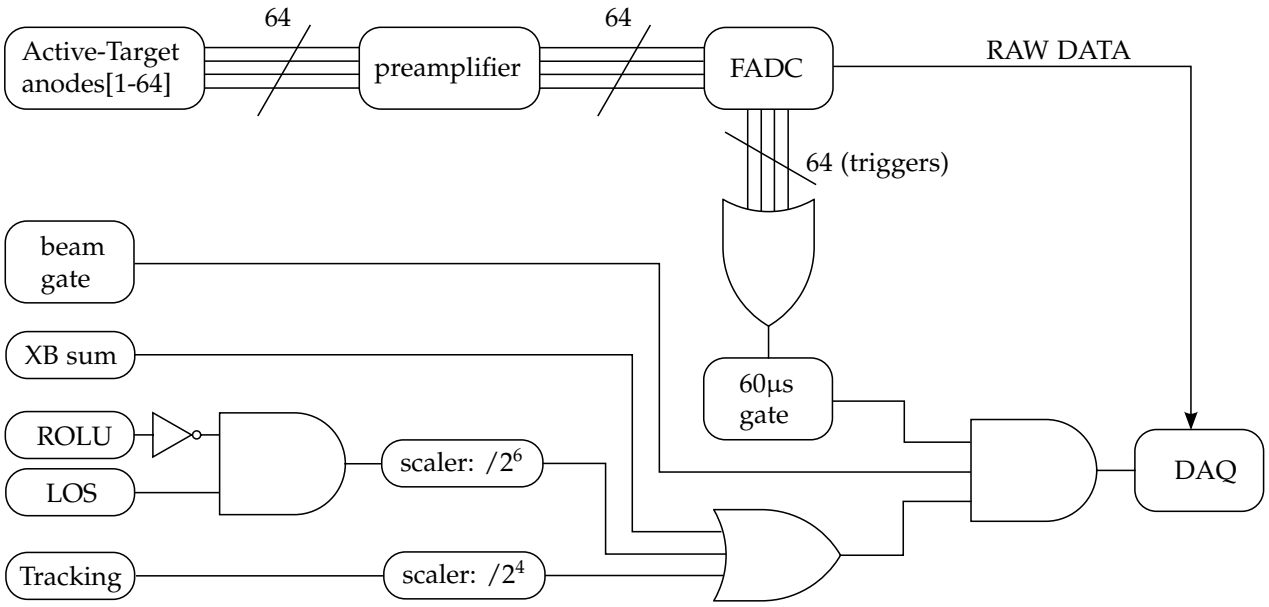

Figure 4.4: Trigger logic scheme of the AcTar setup. This configuration allows to detect in coincidence the occurrence of a scattering reaction and favourable beam particle. If the trigger condition if fulfilled the DAQ records the FADC signal traces with the time reference of the LOS trigger.

For further kinematic measurements it is important that the AcTar signal from each channel is recorded with reference to the arrival time of the beam particle. To do so, a second trigger level (beam trigger) was generated to provide a time reference for the beam particle and acknowledge its validity. The beam trigger is obtained from the LOS detector in anti-coincidence with the ROLU alone or in coincidence with tracking detectors (Tracking) or crystal ball sum (XB sum), see Figure 4.4. The "Tracking" signal indicates that the beam particle traversed all tracking detectors, and the "XB sum" indicates the detection of gamma radiation anywhere in the crystal ball detector. Downscale factors were implemented in some of the signals with higher rate to attenuate their contribution in the overall event rate. The "beam gate" determines the beam spill duty time (onspill or offspill). In order to have the AcTar DAQ record data from the digitisers, the coincidence condition between the beam trigger, beam gate and recoil trigger must be fulfilled. The recoil trigger is previously stretched by the maximum AcTar electron drift time (60 μs) creating a recoil gate and the beam trigger is delayed by the same quantity to ensure that the triggers coincide regardless of the $z-$position (i.e. position along the beam direction) in the cathode-grid space where scattering has occurred. If the coincidence is fulfilled, every channel is recorded in 82 μs long traces covering

8 μs before and 74 μs after the first LOS trigger. Any occurrence of further LOS triggers during the trace recording period constitute the multiplicity of beam particles per event, which can later be used to discriminate pile-up events. After being digitised the AcTar signals are recorded using the Multi-Branch System (MBS) from GSI, which is used to control the dedicated DAQ. The data is recorded on an event by event basis to produce binary List Mode Data (LMD).

Software

Unpacker — The recorded LMD files from the DAQ contain the collected raw data in a very compact and unmodified form, which is in most cases unsuitable for direct processing. An unpacking (or sorting) program is required to produce easily accessible data files in a standard format that allows the use of analysis frameworks to process these data. In the present work the configurable UCESB unpacker [93] was used and configured to specifically match the data format of the LMD files. With this unpacker the files are then sorted and converted to files containing ROOT *trees*, which represent the experimental data for each recorded event in a single *entry* in the tree. The raw traces from each detector channel are represented by *branches* in the tree with a descriptive name assigned by the unpacker. The LMD data is unpacked only once to the ROOT data format, and any analysis or calibration is then performed based on these files.

Online analysis and histogramming — The ability to quickly unpack, analyse, and visualise the currently accumulated data during the recording phase of the experiment is a valuable asset. It allows for monitoring of the data quality, for prompt detection of anomalies in the detector system and for feedback while tuning the control variables during the experiment. As mentioned above, the unpacking is handled by the UCESB unpacker, which besides reading from the already stored data can also read directly from a network stream provided by the data acquisition system. The reading, analysis and visualisation of the data is performed using the Active-Target Online Monitoring and Analysis Tool (ATOMAT), a Graphical User Interface (GUI) program written in ROOT. ATOMAT updates its content automatically leading to a near–realtime (i.e. with a delay associated to the unpacker processing time) view of the data. For more detailed information on ATOMAT refer to Appendix B.1.

4.3 Interaction of charged particles with matter

When a charged particle moves through a neutral medium it will interact electromagnetically with both the electrons and nuclei of the material. These interactions cause a continuous energy loss of the charged particle, which is decelerated from its initial energy E, and to be possibly stopped inside the material. The electromagnetic interactions with the nuclei occur as Rutherford scattering and are seen as small (only occasionally large) changes in the propagation directions. On the other hand, the mechanisms of Coulomb scattering with the negative charge cloud of atomic electrons of the medium are far more frequent and are seen as a fairly steady loss of kinetic energy. The energy transferred to the medium can be low, to only excite atoms and molecules, or high enough to produce ionisation. In the case of the AcTar only the ion-pairs resulting from the ionisation process are detected.

The value of the differential ratio $-dE/dx$ along the particle track defines the specific energy loss (also called "rate" of energy loss). For particles with a given charge state, the specific energy loss increases as the velocity decreases. The expression for the specific energy loss is known as the Bethe-Bloch formula [94, 95] and for an incoming particle of mass $M \gg m_e$ it is written

$$-\frac{dE}{dx} = \frac{4\pi e^4 z^2}{m_e v^2}\frac{N_0 \rho}{A} B, \tag{4.1}$$

where the factor B is not constant but varies slowly with energy in a logarithmic manner and is calculated as

$$B \equiv Z\left[\ln\left(\frac{2m_e v^2}{I}\right) - \ln\left(1-\frac{v^2}{c^2}\right) - \frac{v^2}{c^2}\right] - C_K. \tag{4.2}$$

In these expressions, z and v are respectively the atomic number and velocity of the primary particle, N_0 is the Avogadro number, e is the electronic charge and m_e is the electron rest mass. ρ, A and Z are respectively the density, atomic weight and (average) atomic number of the absorber medium atoms. The parameter I is the average ionisation and excitation potential of the absorber medium and C_K is the correction term for the partial screening of the nuclear charge by inner (K-shell) electrons at low kinetic energies (shell correction term).

The penetration depth of the primary particle, also referred as range R, can be calculated as

$$R(T) = \int_T^0 \left(-\frac{dE}{dx}\right)^{-1} dE, \tag{4.3}$$

where T is the particles kinetic energy. The range of alpha particles was calculated for three different operating pressures using SRIM[7] [96]. The results of the simulation are illustrated in Figure 4.5 for energies between 0 and 10 MeV. Considering the dimensions of the AcTar ionising chamber, it can be seen that at lower pressures (2bar) the particles with energies above 5 MeV tend to leave the active volume before stopping, and therefore only a part of its energy can be detected.

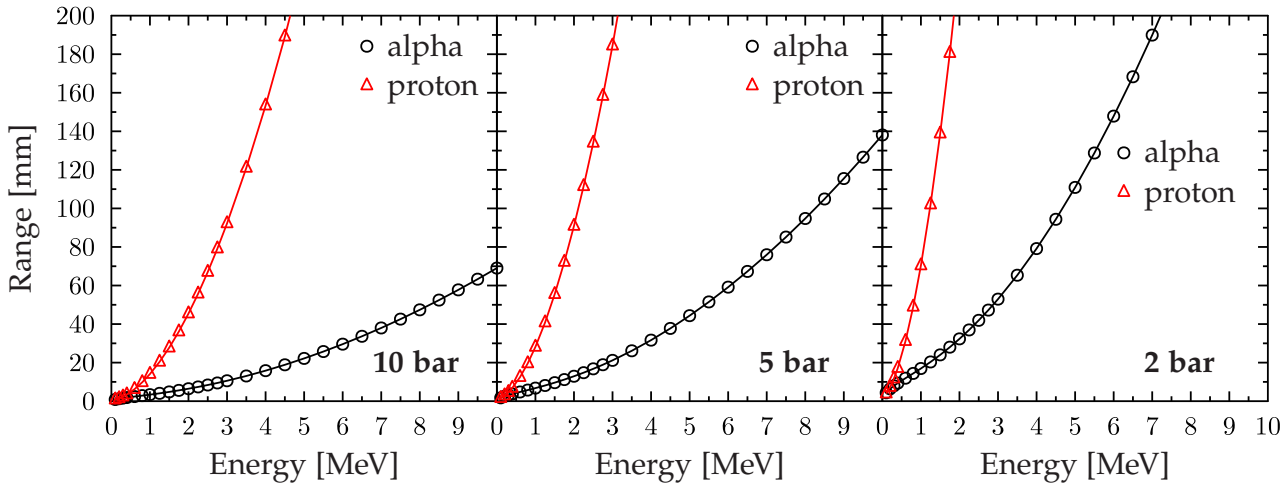

Figure 4.5: Simulation of the penetration depth as a function of energy for recoil particles in a helium-hydrogen gas (3%) mixture for three different pressures. The calculations were performed using SRIM.

[7] SRIM – The Stopping and Range of Ions in Matter.

4.4 Characteristic relations of elastic/inelastic scattering in inverse kinematics

This Section addresses the general features of elastic and inelastic reactions when studied in inverse kinematics. Unlike in normal kinematics experiments in which the Centre-of-Mass (CM) frame is almost at rest in the laboratory frame, in inverse kinematics the CM frame moves at nearly the beam velocity, since the target is much lighter compared to the projectile. Measured in the CM, taking in account the conservation of momentum, the velocities of the two particles after collision must be in inverse proportion to their masses (see Figure 4.6).

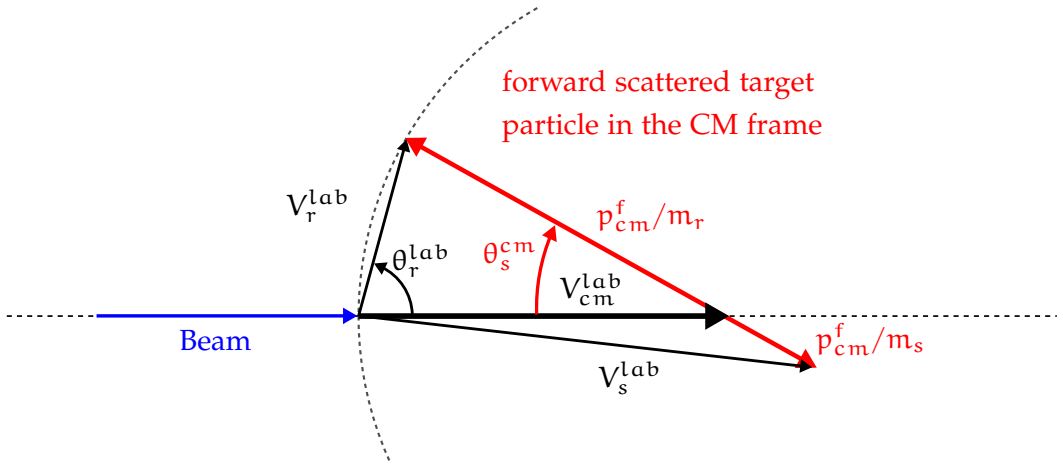

Figure 4.6: Velocity diagram for elastic scattering in inverse kinematics. The picture is strictly classical, using the Galilean addition of velocities. The picture shows that the light target particle (recoil) emerges just forward 90° for small CM scattering angles.

The two body kinematics for elastic/inelastic scattering reactions connects the scattering angle in the laboratory frame with the recoil energy:

$$T_r^{lab} = \sqrt{p_r^2 + m_r^2} - m_r, \tag{4.4}$$

with the recoil momentum p_r being:

$$p_r = \frac{\sqrt{p_{cm}^{f,2} + m_r^2}\cos\theta_r \sinh\phi \pm \cosh\phi\sqrt{p_{cm}^{f,2} - m_r^2\sin^2\theta_r \sinh^2\phi}}{1 + \sin^2\theta_r \sinh^2\phi} \tag{4.5}$$

where p_{cm}^f is the momentum of the centre-of-mass after collision, m_r is the mass of the recoil particle and ϕ is the centre-of-mass rapidity. The detailed derivation of kinematical relations in inverse reactions, as for the present scenario, is explained in the Appendix A.

Figure 4.7 illustrates the kinetic energy of the recoiled target nuclei as function of the scattering angle in the laboratory frame for the scattering process in inverse kinematics. An example is shown for elastic and inelastic scattering on alpha particles of ^{58}Ni nuclei at 700 MeV/u. The maximum kinetic energy imparted to the recoiled alpha particle is ~8656 MeV, and the maximum angle of the scattered ^{58}Ni nucleus is 4°.

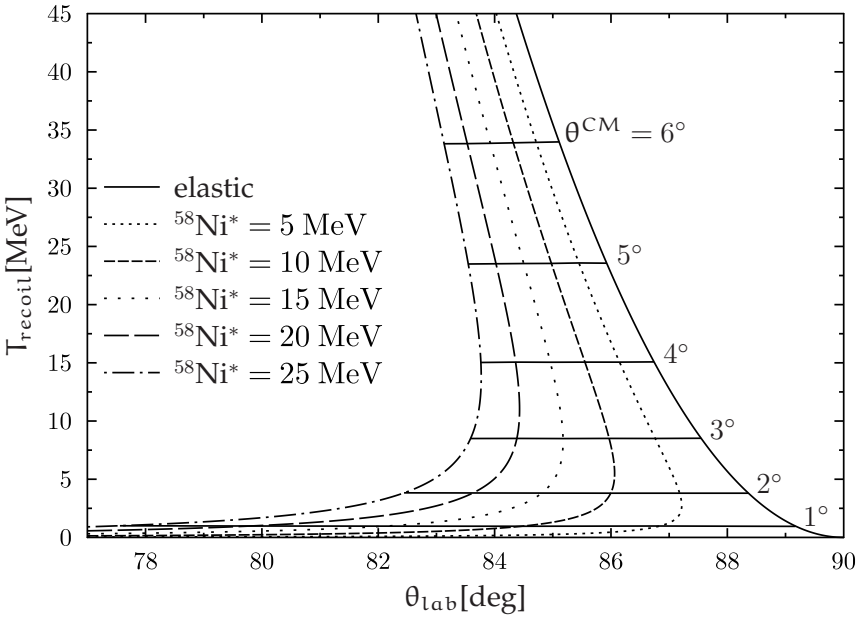

Figure 4.7: Kinetic energy as function of the scattering angle in the laboratory frame of recoiling ^{4}He target nuclei for elastic and inelastic scattering events. The curve was derived from Equation 4.5 for an incoming beam energy of $T_p = 700$ MeV/u. Centre-of-mass angles θ^{CM} are indicated in the curve.

4.5 In-beam test measurements

In the AcTar, the post-reaction information on the recoil particle is obtained by analysing the pulse shape and drift time of signals induced in the anode cells. The method of recording the AcTar signal traces from the FADC used in the current work, has permitted to determine the recoil energy T_r, the recoil scattering angle θ_r and the vertex position (i.e. the longitudinal z-coordinate at the AcTar where the scattering reaction occurred) in offline analysis. The FADC raw data was previously prepared before further feature extraction. The baseline was estimated, in a first approximation, by averaging the value of the first 200 samples (8 μs) of each anode trace, where no signal is present, and then subtracted from the signal. A smoothing procedure was applied to the raw signals for improving the signal-to-noise ratio by filtering the high frequency noise component of the signal using a Moving Binomial (MB) filter. The MB filter was set to 20 samples (0.8 μs) wide, corresponding to ~1.5 MHz half-transmission cutoff frequency.

Figure 4.8 (left) illustrates a typical recoil alpha pulse from a given AcTar ring cell. The τ_b and τ_e points were calculated following a peak searching algorithm using the Moving Gradient (MG) filter. These points correspond respectively to the samples in which of the maximum slope tangent of the signal rising and trailing edge intercepts the baseline. In order to compensate for low-frequency baseline oscillation and baseline pull-down following the signals, the baseline level was recalculated by averaging over 300 samples (12 μs) preceding τ_b and 300 samples following τ_e. For further calculation the location of the τ_b sampling point in each anode FADC trace will be used as the signal time reference sample to determine the z-coordinate of the recoil particle in the cathode-grid space.

Since the distance between grid and anode is relatively small, variations in the signal width along the recoil particle path, which are related to the electron drift time in that region, are also

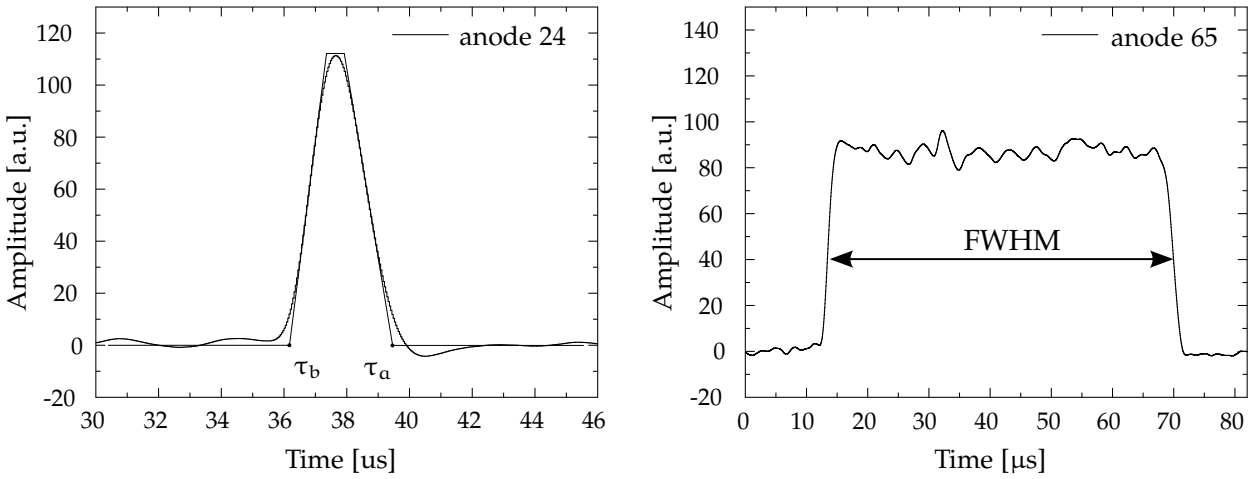

Figure 4.8: Example for measured current signal from a ring anode (left) and central anode (right), as recorded by the FADC. Smoothing and baseline subtraction were applied to raw signals. The value τ_b denotes the beginning of the pulse and is used to determine the z-coordinate position of the recoil particle in units of electron drift time, τ_e denotes the end of the pulse. The FWHM of the central anode signal (right) is equivalent to the total electron drift time in the cathode-grid space. The given signal corresponds to the common shape of a non scattered event.

small (< 1.5 μs for large recoil angles). This results in a constant width of the signal from anodes with a same length, as can be noticed in the example event illustrated in Figure 4.9a of a recoil alpha particle as registered in the AcTar. The signal's characteristic width in the FADC trace is related to the scattering angle and constitutes an important selection criterion in the process of identifying recoil particle pulses.

4.5.1 Energy measurement of recoil particles

In order to determine the energy of the recoil particle T_r, or its energy loss ΔT_r in case it leaves the active volume, the amount of energy collected in each anode cell was measured by performing an integration to the induced charge in the region between τ_b and τ_e delimiting the pulse, see Figure 4.8. The value of the integration was calculated by applying the moving integration filter, as referred in Section 2.2.1, which is later calibrated into an energy value.

As previously mentioned in Section 4.2.2, an event that occurred in the AcTar is recorded whenever the trigger logic condition is fulfilled. In order to identify the anode cells in which energy has been deposited by the recoil particles, a trigger was applied to the signals of every AcTar anode cell. The threshold of these triggers was dynamically adjusted based on the Root Mean Square (RMS) noise value of the signal's first 200 samples (where usually no signal is present) of each FADC channel. On a regular noise level of the AcTar system, the trigger threshold corresponded to a minimum detectable energy of approximately 200 keV per anode cell. For the inner two anode cells (number 65 and 66), the beam particle occasionally propagates across both of these volumes due to scattered or unfocused beam. In such cases it is simple to treat the two inner anode cells as one by adding their signals together, see Figure 4.9c. The energy is then calculated by integrating the recoil pulse above the baseline redefined as the plateau of the beam signal.

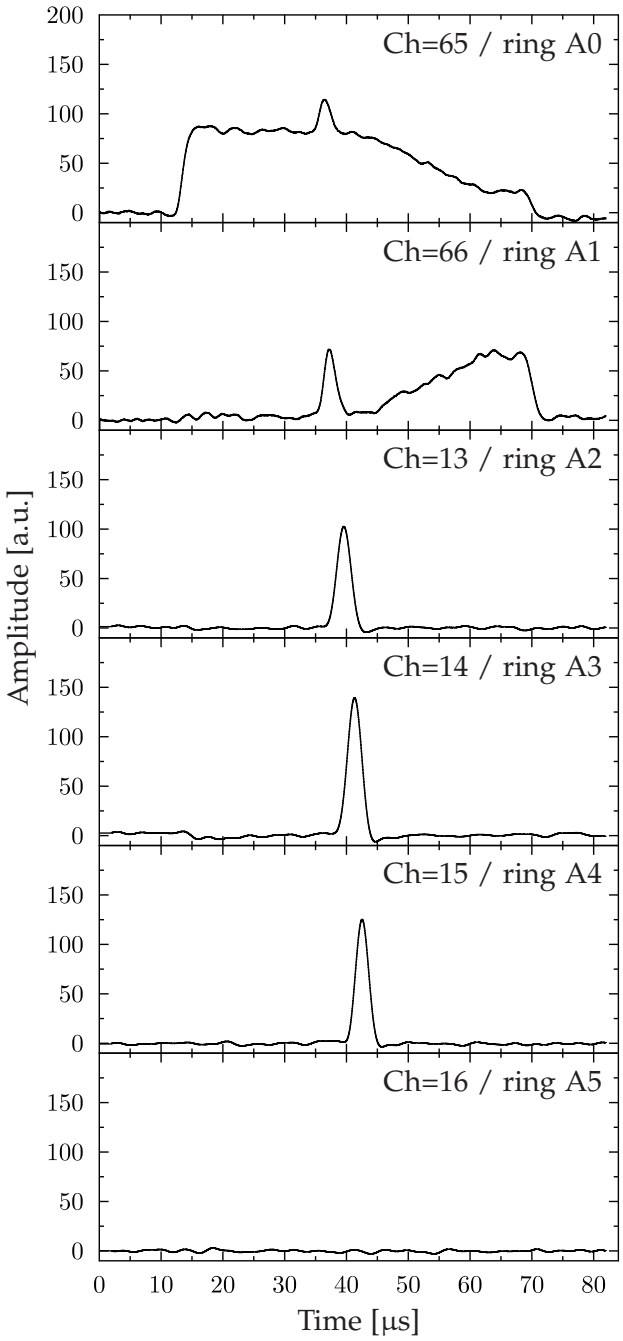

(a) Anode signal traces.

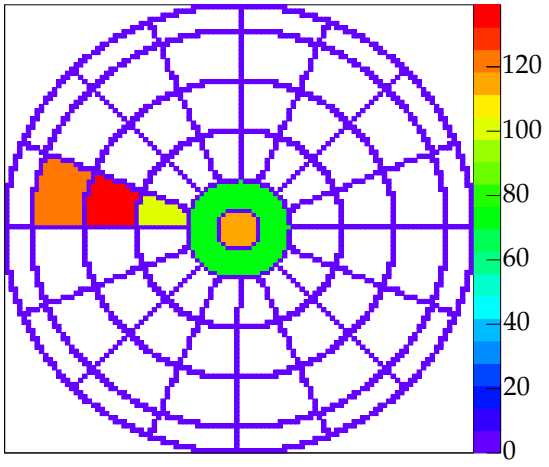

(b) Schematic representation of the triggered anodes. The colour map indicates the amplitude of the signals from (a).

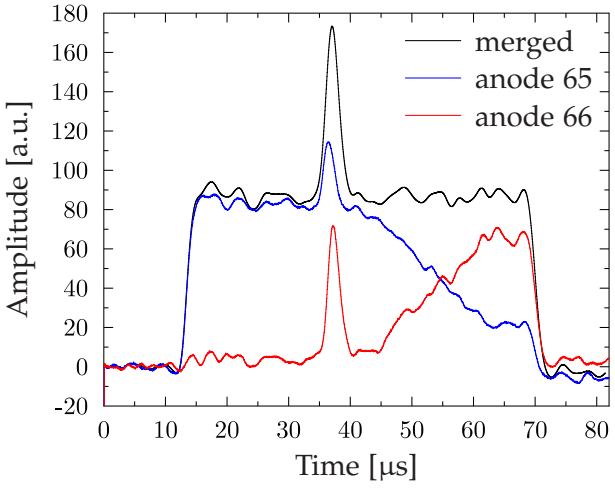

(c) Merging of the two inner most anodes.

Figure 4.9: Typical AcTar event. The time difference between the arrival time of the anode signals from the different rings (a) allows calculating the recoil angle. In the illustrated example the alpha particle was measured at ~ 75° at 5 bar operating pressure. The AcTar anode schematic representation (b) shows the range and azimuth direction of the recoil particle. In (c), the two most inner anodes are merged to reconstruct the shape of the current signal induced by the beam particle.

The triggering of the AcTar anode rings was processed sector wise, i.e. each of the sectors were processed independently, rather than having the energy of all triggered anode cells summed-up per event. This way, in case of pile-up due to delta-electrons produced by the projectile or due to event multiplicity greater than one, the angle and energy of the recoil can still be recovered if the pile-up

does not occur in the same sector. In the example illustrated in Figure 4.9b the recoil particle is emitted radially from the central anode cell and deposits energy along of a single sector, which schematically represented by the coloured cells. The non-triggered ring A5 gives a upper limit to the path length of the recoil particle.

The integral of the anode signals depends on the recoil energy T_r. Figure 4.10 shows the calculated partition of the energy loss by the recoil particles along the regions covered by the anode rings as a function of the recoil particle energy T_r. The values of ΔT_r were calculated using the energy-range curves, assuming a narrow beam aligned along the centre of the chamber axis. The relations between the integrals of the anode ring signals can be used to help separating the elastic events. For instance, in the recoil energy range $T_r \leqslant 2.9$ MeV only two innermost anode ring cells, A0 and A1, measure the total energy of the alpha particle. For $T_r > 2.9$ MeV up to $T_r = 8.3$ MeV the alpha particle energy is fully measured within the AcTar active volume, the value of T_r is just equal to the sum S of the energy loss in the anode rings A2 to A5. For higher energies, in which the radial projection of recoil particle track exceeds the AcTar anode radius, the signals of the anode rings correspond to the respective partial energy losses ΔE in the active volume and the value of T_r can be determined from S. This corresponds to the region after S reaches its maximum in Figure 4.10.

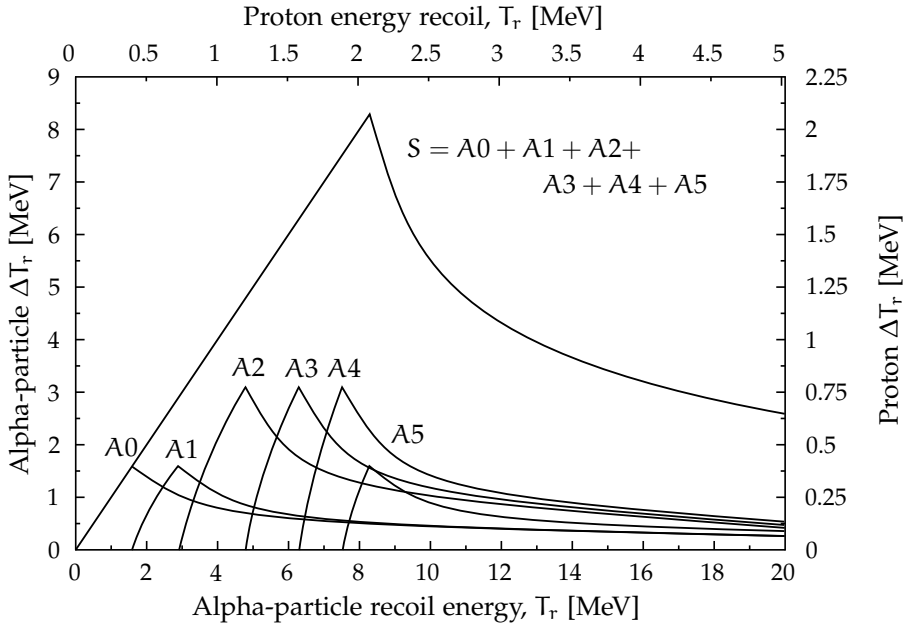

Figure 4.10: Calculated partition of the energy losses of the recoil particles in the volume of the chamber anode rings $A(0-5)$. The calculations were made considering the elastic scattering of ^{58}Ni projectiles with the energy of 700 MeV/u; the beam was considered infinitely thin and to be at the centre of the AcTar; chamber pressure of 5 bar.

The calibration of the integrated signals in the FADC spectra in terms of recoil alpha particles energy was achieved using the signals from the calibration alpha-source implanted in the AcTar cathode. These signals were registered and analysed in a similar way as the recoil signals to preserve a direct correlation. It should be noted that the energy and amplitude of the signals in the AcTar are not proportional to each other as the shape of the signals vary with the angle of the recoil particle. For instance the alpha particles emitted from the source, which always have the same energy, produce signals with different amplitudes as they are emitted isotropically.

In order to measure the energy of the alpha particles emitted from the calibration source their events needed to be discriminated among all events. For the data recorded at 10 bar and 5 bar operating pressure, a trigger mask was used to only allow alpha particles that were emitted in forward direction, triggering exclusively on cell #07. This is the simplest way to obtain an alpha spectrum clean of recoil events or any noise that might randomly trigger another channels. However this process revealed to be unsuitable at lower operating pressure (2 bar), where the maximum energy registered in the alpha spectrum was rather low compared to the alpha peak position, suggesting that the alpha particles from the source do not reach their full range in the AcTar extent (although it doesn't agree with SRIM simulations in Figure 4.5). The full energy of the alpha particle could be reconstructed when allowing to sum up the energy of neighbouring cells to an extent of at least 2 cells from number #07 (i.e. for alpha particles emitted at forward angles $> 20°$ from the source). Figure 4.11 shows the energy spectra of the alpha source, E_α = 5486 keV, obtained for the three different operating gas pressures.

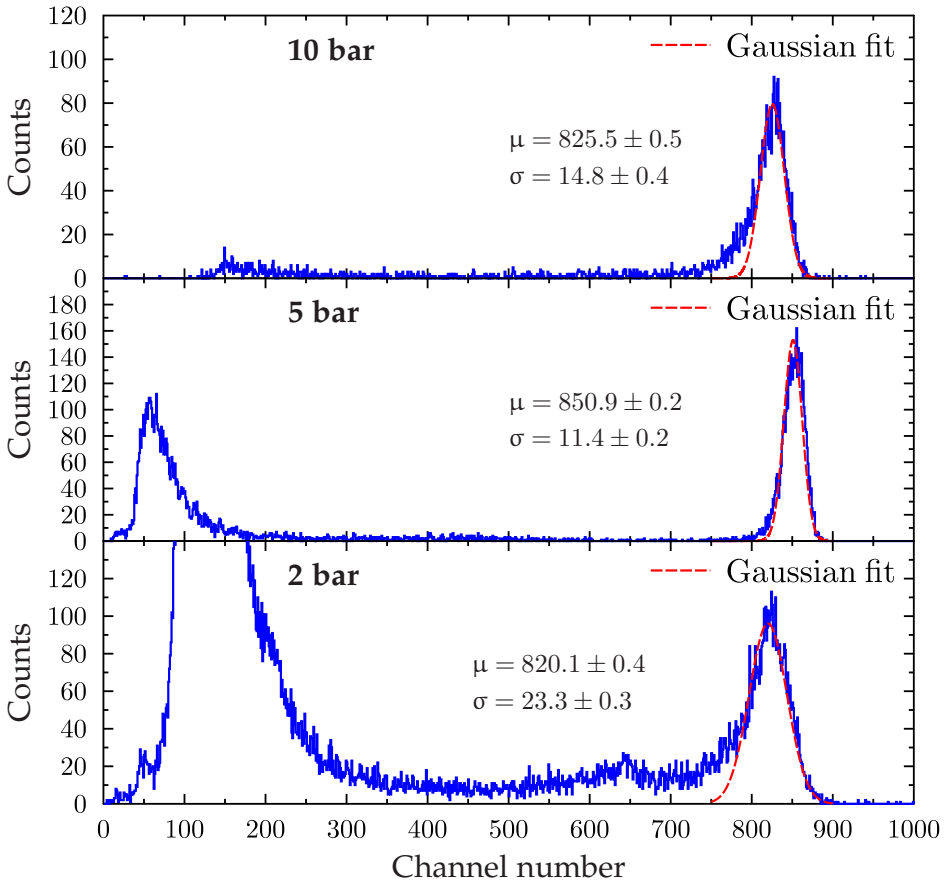

Figure 4.11: Energy histogram of the ^{241}Am source implemented in the AcTar cathode for calibration use measured at three operating pressures. The ^{241}Am source has an alpha-line with energy E_α = 5486 keV. The Gaussian fit was used to determine the energy mean value.

For the current analysis it has been considered that the charge in the anodes is in good approximation a linear function of the recoil energy in the whole energy range and that this function goes through zero of the coordinate system. In order to estimate the energy resolution ΔE the energy

spectra of the AcTar alpha-source, shown in Figure 4.11 were fitted with a Gaussian function, to obtain the following result: $\Delta E \leqslant 226$ keV for 10 bar, $\Delta E \leqslant 169$ keV for 5 bar and $\Delta E \leqslant 358$ keV for 2 bar operating pressure.

The obtained resolution is significantly lower compared to what is expected for this detector. This has partially to do with the fact that the source is not fully exposed on the electrode surface, but safely held under a fine enclosure. Therefore, slight energy attenuations are expected as the alpha particles leave the source. The amount of attenuation may also differ with the emission angle relatively to the surface normal. The energy value of the detected alpha particles is consequently lower than the value emitted by the source. Below, in Section 4.6 the results will be confronted with the energy-range simulations to estimate the energy of the alpha particles emitted in the forward direction.

An alternative approach for energy calibration would be to use the kinematic relations to calculate the recoil energy from the measured scattering angle of the beam particle. However the calibrated data from the tracking devices are not currently obtained.

When using alpha sources to calibrate proton energies, there is a small energy dependent difference between the amount of ionisation produced by alpha and proton particles of the same energy, as described in [97, 98], that has to be considered. However this correction was not implemented since there were correction variables, such as the adhesion of the electrons and the limit of transparency of the grid, which were not known to this point of the analysis. Consequently all particles have been calibrated with the same factor.

4.5.2 Flash-ADC calibration in terms of AcTar geometry

An important element in the data analysis is the calibration of the FADC recorded traces in terms of the geometrical extension of the active volume of the AcTar ionising chamber. Given that the central anode is aligned with the beam line, the beam particles crossing the ionising chamber also produce a signal in this anode. For the beam energies of the present experiment the rate of energy loss in the medium is fairly constant. This creates a homogeneous current signal (and consequently of constant amplitude) during the period the beam particle travels between the grid and the cathode. Figure 4.8 (right) illustrates the shape of the current induced in the central anode, convoluted with the response function of the preamplifier electronics, for an event where no scattering reaction has occurred. By analysing the edges of multiple averaged signals from the central anode, the sampling-points in the recorded FADC trace can be deduced which correspond to the sample in time when the electron produced at the cathode and grid positions arrive at the anode. These cathode and grid sampling-points are the same for all AcTar cells since the FADC channels are all synchronised and their cable lengths are the same. Their difference, i.e. the width of the central anode cell signal, is equivalent to the total electron drift time T_{drift}. The T_{drift} relates to the precisely known cathode-grid geometric distance of d = 217 mm and can be used to calibrate FADC traces in geometrical units. Figure 4.12 shows the histogram of the Full Width Half Maximum (FWHM) of the central anode signals. Each one of the plots correspond to a different pressure of the ionising gas in the chamber. The high voltage values for each pressure were adjusted so that the electron drift times remain similar (see Table 4.2).

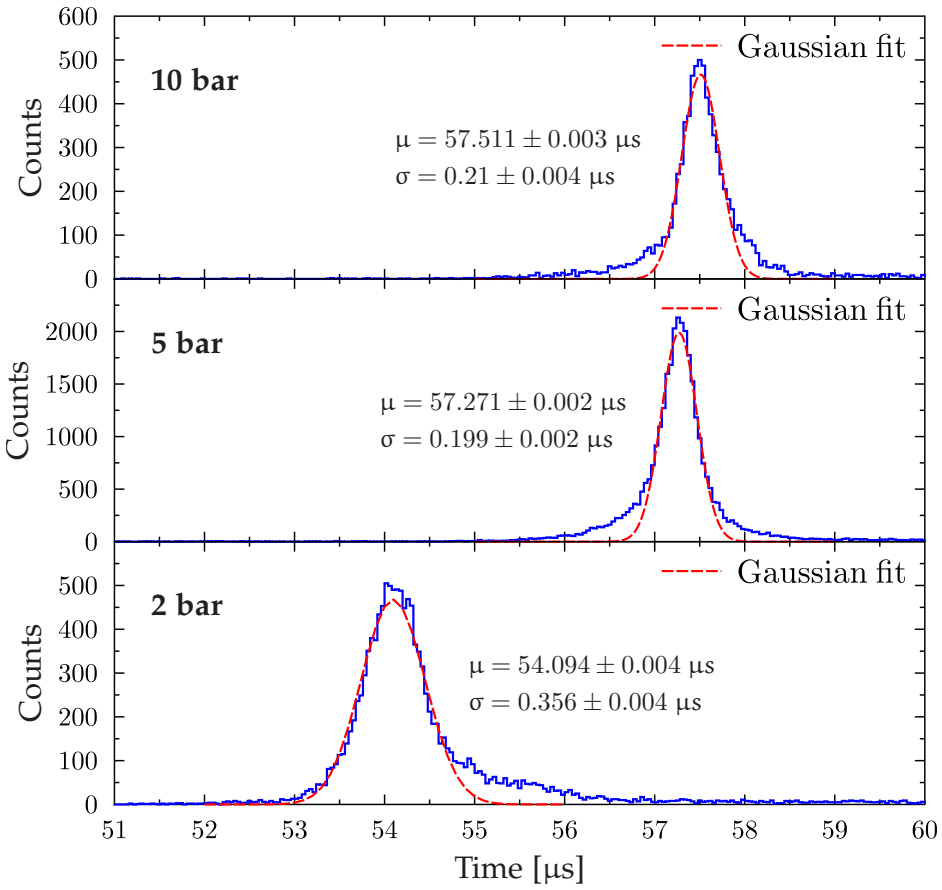

Figure 4.12: Histogram of the total electron drift time between the grid and cathode of the AcTar ionising chamber, measured at three different pressures. The Gaussian fit was used to determine the distribution mean value.

By using the calibration total electron drift time (T_{drift}) and the distance (d = 217 mm) between cathode and grid in the ionising chamber, the drift velocity of the electrons in the chamber can directly be obtained as:

$$V_{drift} = \frac{d}{T_{drift}}. \tag{4.6}$$

For each of the operating pressures 10 bar, 5 bar and 2 bar a mean electron drift velocity of $V^{10bar}_{drift} = 3773 \pm 0.6\ ms^{-1}$, $V^{5bar}_{drift} = 3789 \pm 0.5\ ms^{-1}$ and $V^{2bar}_{drift} = 4012 \pm 0.7\ ms^{-1}$ was respectively obtained. These drift velocities agree well with the data form [99] for the same reduced electric field strength of: $E/p = 0.147$ V/(cm mm-Hg) for the 10 and 5 bar case; $E/p = 0.153$ V/(cm mm-Hg) for the 2 bar case.

The precise calibration of the FADC time scale is required not only to determine the vertex position where the reaction occurred, but also to determine the effective target length (ΔL), that can be chosen to be smaller than the distance d between cathode and grid. This permits to remove the scattering events from the analysis, which may occur in the vicinity of the cathode and grid from the interaction of the beam particles with the electrodes material (this phenomenon will be further investigated in Section 4.6).

4.5.3 Angular measurement of recoil particles with the AcTar detector

In the AcTar the angular information is obtained by analysing the time-stamp in the FADC trace of the signals induced in the anodes. Figure 4.9 illustrates an example of a scattered event registered in the AcTar for a measured recoil alpha particle. Note the shift in time between the pulse signals from the anode cells along the path of the recoil particle in the example recoil event shown in Figure 4.9a.

By using the signals arrival time reference τ_b, the alpha recoil angle can be reconstructed from the arrival time difference $\Delta\tau_z$ between the pulses. Knowing the electron drift time V_{drift}, the longitudinal component ΔZ, i.e. the Z-axis projection (with Z being the beam direction) of the recoil particle track between anode rings, can be calculated as:

$$\Delta Z = V_{drift} \cdot \overline{\Delta\tau_z}. \tag{4.7}$$

Depending on the range of the recoil particle, $\overline{\Delta\tau_Z}$ is calculated averaging the arrival time difference between signals from all triggered neighbouring anode rings in the range A2 to A5. The anode ring A1 was not used for angular measurements due to its proximity to the beam line, which subjects this anode ring to higher noise levels and occasional interception of scattered or unfocused beam particle (see Figure 4.9c).

The width of the AcTar anode rings is precisely defined, see Table 4.1, and gives information for the radial component of the recoil track, i.e. the projection in the anode plane. Using both, the longitudinal ΔZ and radial ΔR projection components to define the direction of the recoil particle, the recoil angle θ_r relative to the beam direction can simply be calculated as follows:

$$\theta_r = \arctan\left(\frac{\Delta R}{\Delta Z}\right). \tag{4.8}$$

Figure 4.13 (left) shows the 2-dimensional correlation of the arrival times difference between the signals from anodes A2 and A3 ($\Delta\tau_z(A2 \rightarrow A3)$) versus the difference between the signals from anodes A3 and A4 ($\Delta\tau_z(A3 \rightarrow A4)$), the time difference for those pairs of anode rings is expected to be identical since they have the same width, ΔR = 22 mm. The spread of this correlation can be used to estimate the angular resolution. The value of $\Delta\tau_z$ characterises the recoil angle θ_r. As an example, the histogram of Figure 4.13 (right) shows the number of scattered particles as a function of $\Delta\tau_z(A3 \rightarrow A4)$ for the interval $240 \leqslant \Delta\tau_z(A2 \rightarrow A3) < 280$ ns. By fitting a Gaussian function to this histogram it computes a resolution of $1.31 \pm 0.1^\circ$. One should note that calculating the recoil angle from only two neighbouring rings constitute the worst resolution case, the longer the range of the recoil particles the more anode rings are triggered, consequently improving the angular resolution.

The example event illustrated in Figure 4.9 corresponds to an calculated recoil angle of $\theta_r \approx 75^\circ$.

4.6 Selection of recoil events

Besides elastic and inelastic scattering events, there are sorts of other events such as false events due to random coincidences, alpha particles from the calibration source and scattering of beam particles form the electrodes and grid in the AcTar which contribute to the background. The first step in selecting the recoil events was to eliminate events corresponding to the alpha-source. Therefore,

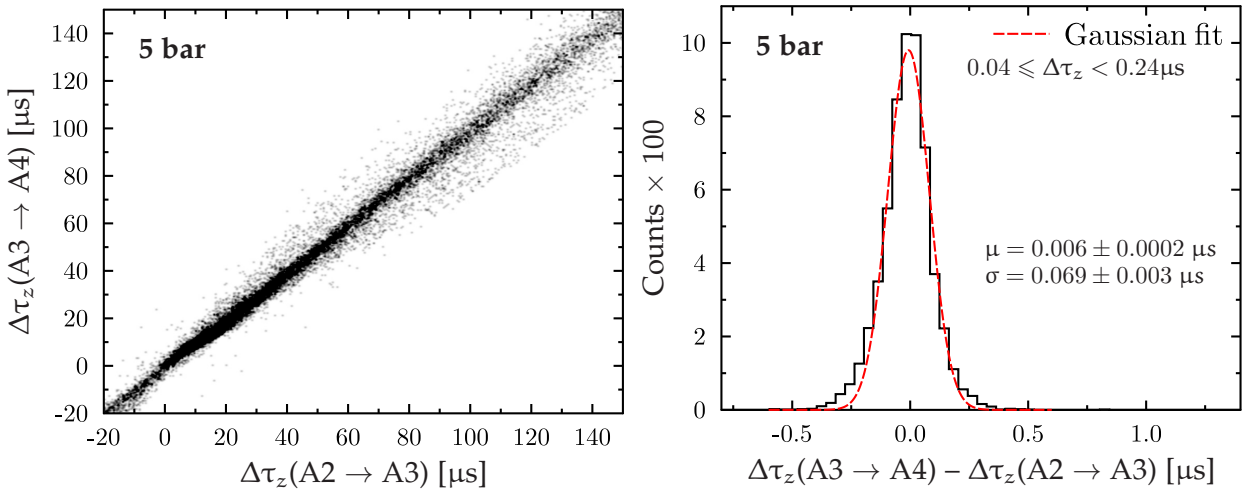

Figure 4.13: (left) Correlation of the arrival times difference of the signals from anodes A3 and A4 ($\Delta\tau_z$(A3 → A4)) versus the arrival times difference of the signals from anodes A2 and A3 ($\Delta\tau_z$(A3 → A4)), $\Delta\tau_z$ is related to the recoil angle. (right) Distribution of events as a function of the time difference between $\Delta\tau_z$(A3 → A4) and $\Delta\tau_z$(A2 → A3) for a given interval of $\Delta\tau_z \in [0.04, 0.24[$. Operating pressure of 5 bar; 1 channel = 40 ns.

events with origin in the anode cell #07 (i.e. cell #07 registers the earliest pulse from all triggered cells) are discarded. It is assumed that alphas emitted from the source always deposit energy in this cell. Secondly, the events range was set to minimum in order to be able to calculate the recoil angle, where only recoil particles reaching anode A3 were considered. A large fraction of background events can be eliminated by defining discriminating limits based on the two-dimensional correlation between the onset time of the recoiled particles as they are detected in the anode ring A2 and the calculated recoil angle (according to Equation 4.8). An example is shown in Figure 4.14 considering the data recorded at the operating pressure of 5 bar. As referred in Section 4.2.2, the FADC time spectra are fixed with relation to the LOS signal (beam trigger), therefore the time scale of the anode cells and in particular of ring A2 are tightly related to the z-coordinate where the scattering reaction has occurred in the AcTar chamber. One can then observe a large concentration of events in the AcTar regions in the vicinity of the grid and cathode respectively located at around 15.5 μs and 72 μs. On the grid end of the AcTar chamber this large concentration of events result from scattering particles that might have interacted with the anode or grid material. Such events were eliminated by choosing a slightly smaller effective target length ΔL, covering the AcTar active volume from 20 μs on. On the cathode end of the AcTar, the large concentration of events is registered at backward angles ($\theta_r > 90°$) that results from recoil particles which interact with the cathode material. The fact that many of the backward recoil events are registered along the whole AcTar volume rather than only in the vicinity of the cathode is due to overlapping of events with multiplicity higher than one or due to random coincidences. All the recoil particles exceeding $\theta_r > 90°$ were removed from the dataset.

Furthermore, particles scattered at small forward angles or in which the measured recoil angle was considerably discrepant when comparing the angle calculated using the kinematic relation with the measured energy (see Section 4.4), were also discarded.

To help distinguishing the true elastic-scattering events, windows can be placed on the two-dimensional correlation plots of the measured recoil particle energies for consecutive anode rings.

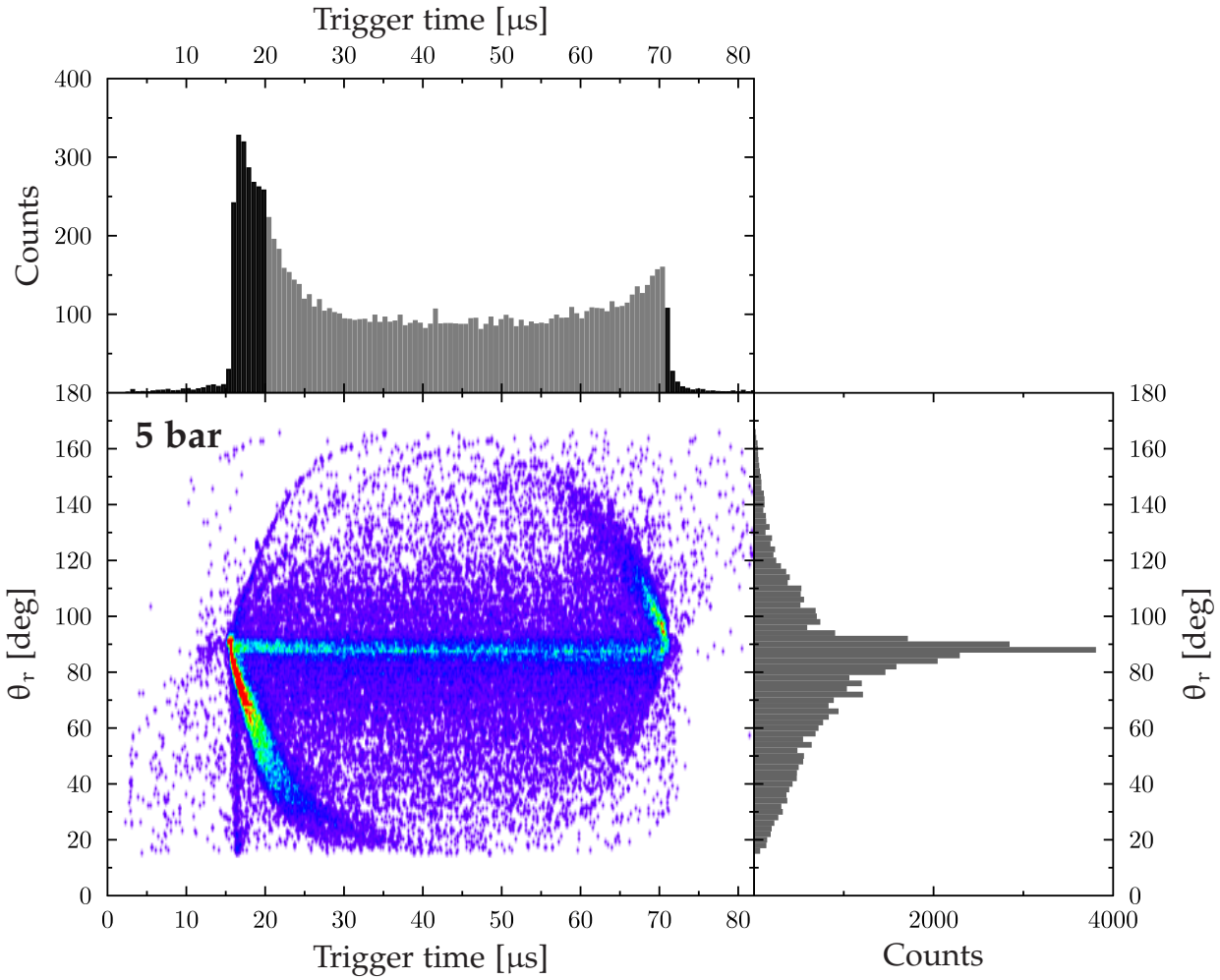

Figure 4.14: Correlation histogram of the recoil particles arrival time at the anode ring A2 versus the calculated recoil angle accordingly to Equation 4.8. The data correspond to recoil events registered in the AcTar for the case of 5 bar operating pressure. The anode and cathode sit respectively at the trigger times of ~15 μs and ~70 μs (see text for more details). The darker regions in the top histogram mark the discarded events when redefining the AcTar active volume length.

As example, Figure 4.15 illustrates the energy correlations of two different ring pairs: A3/A2 and A3/(A2+3), A4/A3 and A4/(A3+A4). The example data corresponds to the case of ^{58}Ni projectiles scattering in the AcTar gas mixture at a pressure of 5 bar. Figures 4.15(a) and (d) show the correlations A3/A2 and A4/A3 before event selection. The regions 1, 2, 3 referred in Figures 4.15(b), 4.15(c), 4.15(e) and 4.15(f) correspond to the regions of increasing energy T_r illustrated in Figure 4.10. For these events the partition of the recoil energies ΔT_r deduced from each of the anode rings, must agree with the calculated energy-range relations. As predicted the elastic scattering events group together forming a characteristic triangular shape pattern. These plots can therefore be used to discriminate background that falls outside the region containing elastic scattering events. The distribution of events in region 1 corresponds to the recoil particles that do not stop in the volume confined by the ring pair under consideration. The branch of region 2 contains recoil particles which stop within the dimensions of the outer anode ring. The narrow distribution along the di-

agonal (region 3) corresponds to the recoil particles that stop within the dimensions of the inner ring.

The technique of using the correlations between anode ring energies also allows to differentiate between the recoil nuclei ^{1}H and ^{4}He in the gas mixture. Note that this technique only works for the region 2 of Figure 4.15, where the recoil particles stop in the outer ring. The double structure observed in the region 2 suggests possible changes in the AcTar parameters during the long run periods, such as the dropping of the high voltage value.

According to the calculations of the energy partition obtained from the energy-range simulations (see Figure 4.10), the maximum energy deposited in the single ring and deposited in the two neighbouring anode rings is expected to be around 3.1 MeV and 4.8 MeV respectively. These values reveal a slight overestimation of the results shown in Figure 4.15, suggesting that the simplified method of energy calibration adopted in the present work is not accurate enough. This is partially due to the fact that the alpha particles lose energy before reaching the AcTar active medium, as stated in Section 4.5.1. One can then confront the energy-range simulations with anode energy correlations (see the red curve in Figure 4.15 (c) and (f)) to estimate a reasonable value for the energy of the source. The corrected energy value calculated considering the alpha detected in forward direction was 4724 keV (as opposition to the initial 5486 keV).

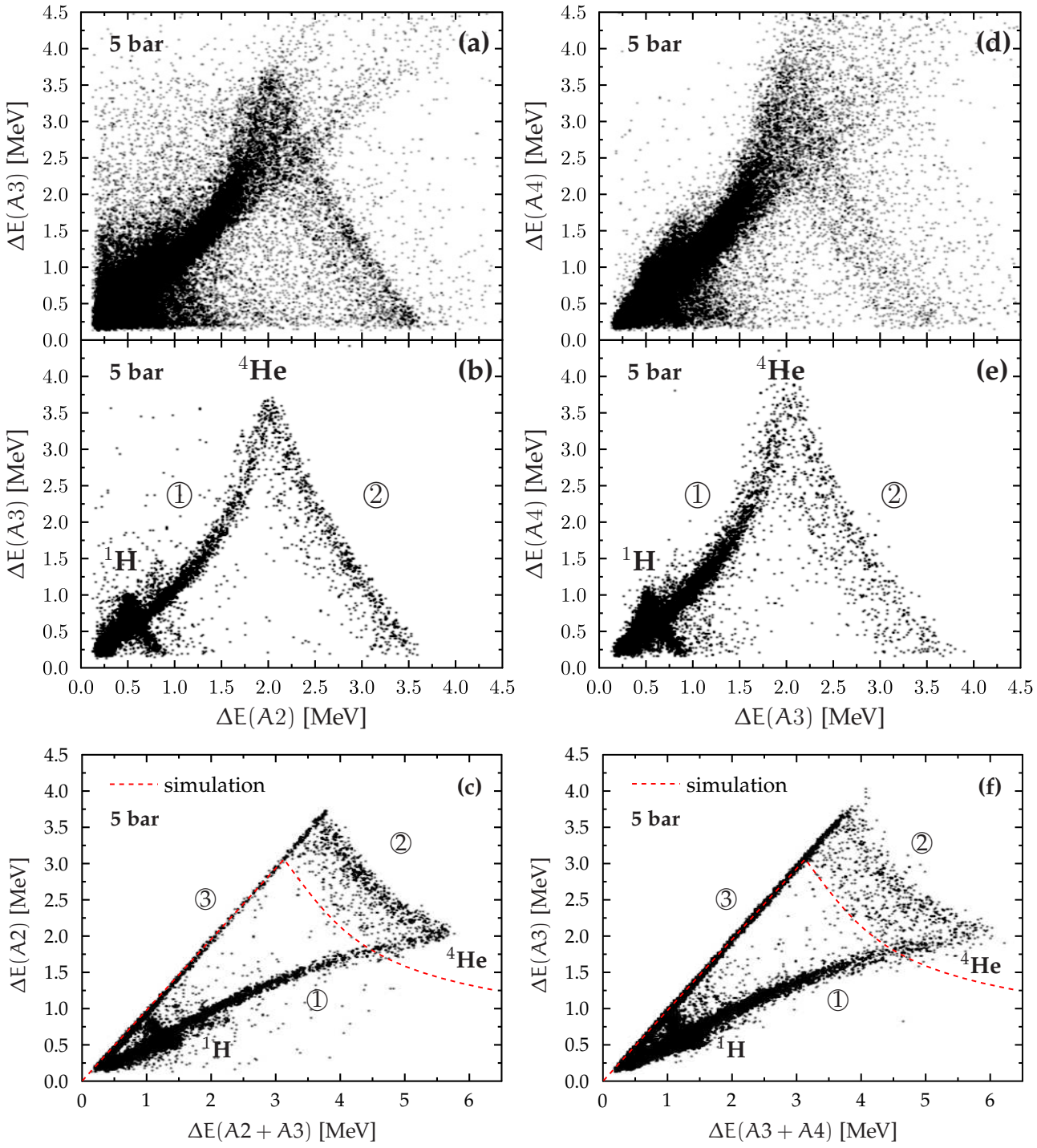

Figure 4.15: Two-dimensional correlation plots of anode energy signals (see Section 4.5 for definition), as registered in the AcTar for the case of ^{58}Ni scattering in the gas mixture at 5 bar pressure: (a) the energy measured in ring A3 cells versus the energy measured in ring A2 cells corresponding to the same sector, (b) same as (a) after selecting good events; likewise (d) and (e) show the energy correlation between ring A3 and ring A4 cells. The plots (c) and (f) show respectively A2 versus A2+A3 energies and A3 versus A3+A4 energies. The recoil particles corresponding to elastic scattering events group together to form a characteristic pattern of triangular shape. The dashed red line represents the simulated value from the energy range calculations.

Chapter 5

Summary and Outlook

Within the scope of the present thesis digital pulse shape analysis have been employed to extract information and improve the performance of two distinct detector systems, a CsI(Tl) based scintillation detector and an active-target (AcTar).

The suitability of using digital pulse shape analysis has been tested with CsI(Tl) based scintillation detectors to compensate for the detector gain shifts due to temperature fluctuations. The method exploits the influence of the temperature on the scintillation characteristics, i.e. relative fraction and time constants of the different decay components in the light pulse of the crystal. This feature of the scintillator material is carried on the pulse shape of the detector signal. Thus, Pulse Shape Analysis (PSA) provides a unique way to estimate the scintillators internal temperature and related gain corrections.

Two different ways of defining a pulse shape parameter have been proposed applying PSA on the digitised signal. One uses the ratio of integrals over different regions of the signal. The second considers signals as multidimensional vectors and by means of vectorial calculations measures the distance or angle between the current Mean Pulse Shape (MPS) and a reference MPS. The obtained shape parameters were then used to correct the temperature dependent gain shifts. Both a Photomultiplier Tube (PMT) and an Avalanche Photo-Diode (APD) were used as the crystal's readout photosensor to test the method.

The approach of using the crystals temperature to correct for the whole detector takes into account that both, the crystal and the photosensor, contribute to the gain shifts. The temperature of the photosensor is inferred via a straight mechanical contact to the crystal, hence ensuring a good thermal equilibrium. Nevertheless, there are other partly temperature-independent factors including drifts of the PMT and APD supply voltage, gain instability of the used preamplifiers and possible damage of the photosensor which may affect the gain of the systems. Such contributions are not accounted by this approach.

The results have confirmed that CsI(Tl) scintillators are well suited for this procedure. By showing a smooth monotonic dependence on temperature the proposed shape parameters have proved to serve as a "thermometer" for the crystal's interior. The resolution of both PMT and APD detector

systems have improved when applying the corrections based on the different parameters. Even in the case of the APD in which the gain shifts are strongly ruled by the large thermal sensitivity of the photosensor, this method solves the gain correction problem at a high accuracy level.

In this thesis, the signal's Principal Pulse Shape (PPS) were obtained from a dataset recorded at fairly constant temperature. In a real application the pulse shape has to be calculated as the ambient temperature changes. The idea of "running PPS ", in which the PPS updates over time, can be implemented. A way to do this consists in buffering a constant number of signals where newer signals replace the later. Alternatively, Kalman filters can be used to produce estimates of the current PPS along with their uncertainties. These estimates are updated using a weighted average, with less weight being given to estimates with higher uncertainty.

A robust and reliable method to perform Particle IDentification (PID) calibration for CsI(Tl) detectors in a unsupervised manner have been proposed. It uses fuzzy clustering algorithms to obtain the PPS for each particle species in a mixed dataset with similar population of proton and photon induced signals. These PPS were used to obtain discrimination values which successfully assigned the signals to the different particle species using discrimination regions that are – in contrast to other methods – detector independent.

In the second part of the thesis, Chapter 4, the functionality of the AcTar prototype has been tested to determine its feasibility for the R^3B setup.

The presented results concern AcTar data only. For further conclusions on the performance of this detector relatively to the physical study of elastic/inelastic reactions require other detectors information. Detectors such as crystal ball and beam tracking detectors, are necessary to select events in coincidence with the emission of gamma-rays and to know the position of the projectile in order to precisely calculate the scattering angle. The data from those detectors require further calibration which where not available at the time of this analysis. Although it can be seen that simple cuts applied using only the AcTar data can already clean up undesired background events quite efficiently.

It is possible to observe pulses from the recoils in central anodes of the AcTar because the fluctuations of the signals induced by the heavy particles are relatively small. This provides the possibility of pile-up rejection and a more complete reconstruction of the total energy deposited by the recoil particles. The results obtained from timing information of the recorded traces suggest that the PSA can indeed be used to track the recoil particles and consequently reconstruct the kinematics. The experimental data obtained in the test experiment with the AcTar prototype have proven to be of importance for the construction of the ionising chamber for the R^3B setup. For the first time an active-target of this kind has been successfully tested with beams heavier than carbon.

Ultimately the best approach to refine the pulse information has to be established and implemented in fast digital electronics. Recording the signal's full waveform is extremely demanding considering the storage space required. The online processing of the signals will allow to only record the important information, i.e. energy, timing, angle etc., what dramatically reduces the used storage space.

The present work have contributed to study the suitability of PSA to process deeply embedded information of early stage digitised detector raw signals. The results have proven great advantages in using fully digital systems.

Appendix A

Relativistic inverse kinematics

A.1 Characteristic relation for elastic/inelastic scattering reactions

This section addresses the general features of elastic and inelastic reactions when studied in inverse kinematics. Since in inverse kinematics the target is much lighter than the projectile, the CM frame travels at almost beam velocity. Measured in the CM, taking in account the conservation of momentum, the velocities of the two particles after collision between each other must be in inverse proportion to their masses (see Figure A.1).

The squared norm of the total four-momentum tensor P^{μ} of a system of particles in Minkowski space-time is a Lorentz invariant [100], i.e. invariant upon Lorentz transformations between different frames of reference, such as the system's CM frame and the laboratory (lab) frame. For a system composed of several species (as in a nuclear reaction) the invariant mass is given by:

$$P_{\mu}P^{\mu} = \left(\sum_{i} \frac{E_i}{c}\right)^2 - \left\|\sum_{i} \vec{p}_i\right\|^2, \tag{A.1}$$

where c is the speed of light, $\vec{p}$ and E are the classical three-momentum vector and energy of the given particle respectively.

Considering a projectile beam particle, with mass m_P and kinetic energy T_P, colliding with a target particle with mass m_t and at rest ($T_t^{lab} = 0$) in the laboratory frame. The reaction of this two-particle system creating a new two-particle system with masses m_r and m_S is expressed with the notation $P(t,r)S$, in which the reaction products r and S are commonly named as the recoiled and scattered particles respectively. The Lorentz invariant quantity $P_{\mu}P^{\mu}$ of the binary system ($P+t$) before collision is then calculated as

$$P_{\mu}P^{\mu} = (m_P + T_P^{lab} + m_t)^2 - ((m_P + T_P^{lab})^2 - m_P^2), \tag{A.2}$$

$$= (m_t + m_P) + 2m_t T_P^{lab}. \tag{A.3}$$

The speed of light has been conveniently normalised to unity, $c = 1$. This is not relevant for pure kinematics where only momentum vectors appear. In the CM frame the momenta of the particles P and s have the same magnitude and opposite direction. The invariant $P_{\mu}P^{\mu}$ does not change:

$$P_\mu P^\mu = \left(\sqrt{m_t^2 + p_{cm}^i} + \sqrt{m_P^2 + p_{cm}^i}\right)^2, \tag{A.4}$$

where p_i^{cm} denotes the initial momentum of both particles in the CM frame before reaction. Given that $P_\mu P^\mu$ is constant in both frame the following equation determines p_{cm}^i

$$p_{cm}^i = \sqrt{\frac{(P_\mu P^\mu - m_P^2 - m_t^2)^2 - 4m_P^2 m_t^2}{4P_\mu P^\mu}}. \tag{A.5}$$

The Lorentz transformation can be cast into a convenient form by defining a parameter ϕ called rapidity. In order to determine the rapidity, it is considered that the boost applied to the target with the CM rapidity transforms the momentum p_{cm}^i to the target particle.

$$\begin{aligned}(m_t, 0) \to (E_t, p_{cm}^i) &= (\sqrt{m_t^2 + p_{cm}^i}, p_{cm}^i), \\ &= (m_t \cosh\phi, m_t \sinh\phi).\end{aligned} \tag{A.6}$$

A simple property about hyperbolic trigonometry allows to calculate the CM rapidity ϕ in a tidier closed way

$$\cosh\phi + \sinh\phi = e^\phi \equiv \phi = \ln\left(\frac{p_{cm}^i + \sqrt{m_t^2 + p_{cm}^{i,2}}}{m_t}\right). \tag{A.7}$$

After collision the CM momentum of the reaction products follow from the Equation A.5, in which m_P and m_t are substituted by m_S and m_r:

$$p_{cm}^f = \sqrt{\frac{(P_\mu P^\mu - m_r^2 - m_S^2)^2 - 4m_r^2 m_S^2}{4P_\mu P^\mu}} \tag{A.8}$$

For the case of an elastic scattering reaction, the masses of the binary system do not change upon interaction, $m_P = m_S$ and $m_t = m_r$. On the other hand, for the case of a inelastic scattering reaction whenever the CM energy happens to match the excitation energy of the recoil particle, this excitation energy is given by the mass difference upon interaction, such that $E^* = m_S - m_P$ (and $m_t = m_r$).

Given all the masses and the beam energy (T_P), the rapidity and CM momentum are calculated. Applying the Lorentz boost with the CM rapidity to the reaction products allows to calculate their energy and momentum in the laboratory frame as function of CM quantities.

$$\begin{pmatrix} E^{lab} \\ p_\parallel^{lab} \\ p_\perp^{lab} \end{pmatrix} = \begin{pmatrix} \cosh\phi & \sinh\phi & 0 \\ \sinh\phi & \cosh\phi & 0 \\ 0 & 0 & 1 \end{pmatrix} \begin{pmatrix} E^{cm} \\ p_\parallel^{cm} \\ p_\perp^{cm} \end{pmatrix},$$

where $p_\parallel$ $p_\perp$ are the parallel and perpendicular components of the momentum relative to the beam direction. The simplified vector diagram describing elastic scattering in inverse kinematics is illustrated in Figure A.1. By inspecting the Figure a minus sign needs to be considered for the boost to the recoiled particle. The obtained recoiled energy and momentum are

$$E_r = \sqrt{p_{cm}^{f,2} + m_r^2}\cosh\phi - p_{cm}^{f}\cos\theta^{cm}\sinh\phi, \tag{A.9}$$

$$p_r\cos\theta_r = -p_{cm}^{f}\cos\theta^{cm}\cosh\phi + \sqrt{p_{cm}^{f,2} + m_r^2}\sinh\phi, \tag{A.10}$$

$$p_r\cos\theta_r = p_{cm}^{f}\cos\theta^{cm} \tag{A.11}$$

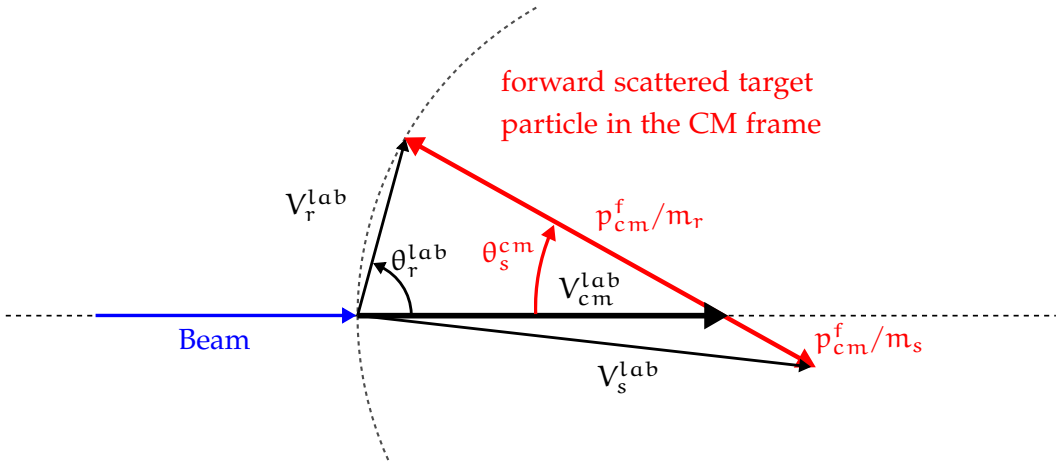

Figure A.1: Velocity diagram for elastic scattering in inverse kinematics. The picture is strictly classical, using the Galilean addition of velocities. The picture shows that the light target particle (recoil) emerges just forward 90° for small CM scattering angles.

Since all measurements are made in the CM frame, it is convenient to calculate the energy and momentum as a function of the laboratory angle. By solving the previous system of three equations in order to eliminate the CM angle, it yields the momentum of the recoiled particle as function of the laboratory angle:

$$p_r = \frac{\sqrt{p_{cm}^{f,2} + m_r^2}\cos\theta_r\sinh\phi \pm \cosh\phi\sqrt{p_{cm}^{f,2} - m_r^2\sin^2\theta_r\sinh^2\phi}}{1 + \sin^2\theta_r\sinh^2\phi} + m_r^2 \tag{A.12}$$

In this solution the quantity under the square root in the second term of the numerator must be positive or zero, since the momentum has to be real. In inverse kinematics this implies a limit on the laboratory angle of the scattered beam particle:

$$m_r\sinh\phi > p_{cm}^{f} \rightarrow \theta_{s,max}^{lab} = \arcsin\left(\frac{p_{cm}^{f}}{m_r\sinh\phi}\right). \tag{A.13}$$

Appendix B

Experimental supplement

B.1 ATOMAT — Active-Target Online Monitoring and Analysis Tool

The ability to quickly unpack, analyse, and visualise the currently accumulated data during the recording phase of the experiment is a valuable asset. It allows to monitor the data quality, for prompt detection of anomalies in the detector systems and for feedback while tuning control variables during the experiment. The unpacking is handled by the UCESB unpacker [93], which cannot only read form the already stored binary List Mode Data (LMD) files, but as well read directly from a network stream provided by the data acquisition system. The reading, analyse and visualisation of the data is performed using the Active-Target Online Monitoring and Analysis Tool (ATOMAT) which as been developed within this thesis. It a Graphical User Interface (GUI) based in the analysis framework ROOT [13]. ATOMAT updates its content automatically leading to a near–realtime (i.e. with a delay associated to the unpacker processing time) view of the data. The program can operate in two major modes: in the first mode ATOMAT shows the data in a oscilloscope fashion displaying signal traces as they are recorded by the flash Analogue to Digital Converter (ADC). It can also be observed which channels are triggered in a bi-dimensional representation of the electrodes map of the anode (see Figure 4.9b); in the second mode the raw data is pre-processed to produce several histograms and correlations of energy, angle, arrival time and shape parameter from each recorded event. Additionally, ATOMAT can be used to write new files in which now the ROOT trees represent the data after being pre-processed, i.e. after calculating the energy, angle, time-stamp and shape parameters of the Active-Target (AcTar) signals, as opposition to having the full raw traces. The branches in the new ROOT tree files store the information contained in the traces in an higher level and with a much smaller size. Therefore, allow a quite substantial decrease of the time required to process files containing large number of events, and easily specify filtering conditions (e.g. timing constraints) to produce special sets of histograms.

Figure B.1 shows screen shots of two interface panels of the running application, for each of the operating modes. In the top picture the signal traces are shown in oscilloscope mode for the first 16 AcTar channels, corresponding to a quarter of the anode area. The bottom screen shot shows the view containing different correlation histogram between energy, arrival time and angle calculated for the different anode rings of AcTar.

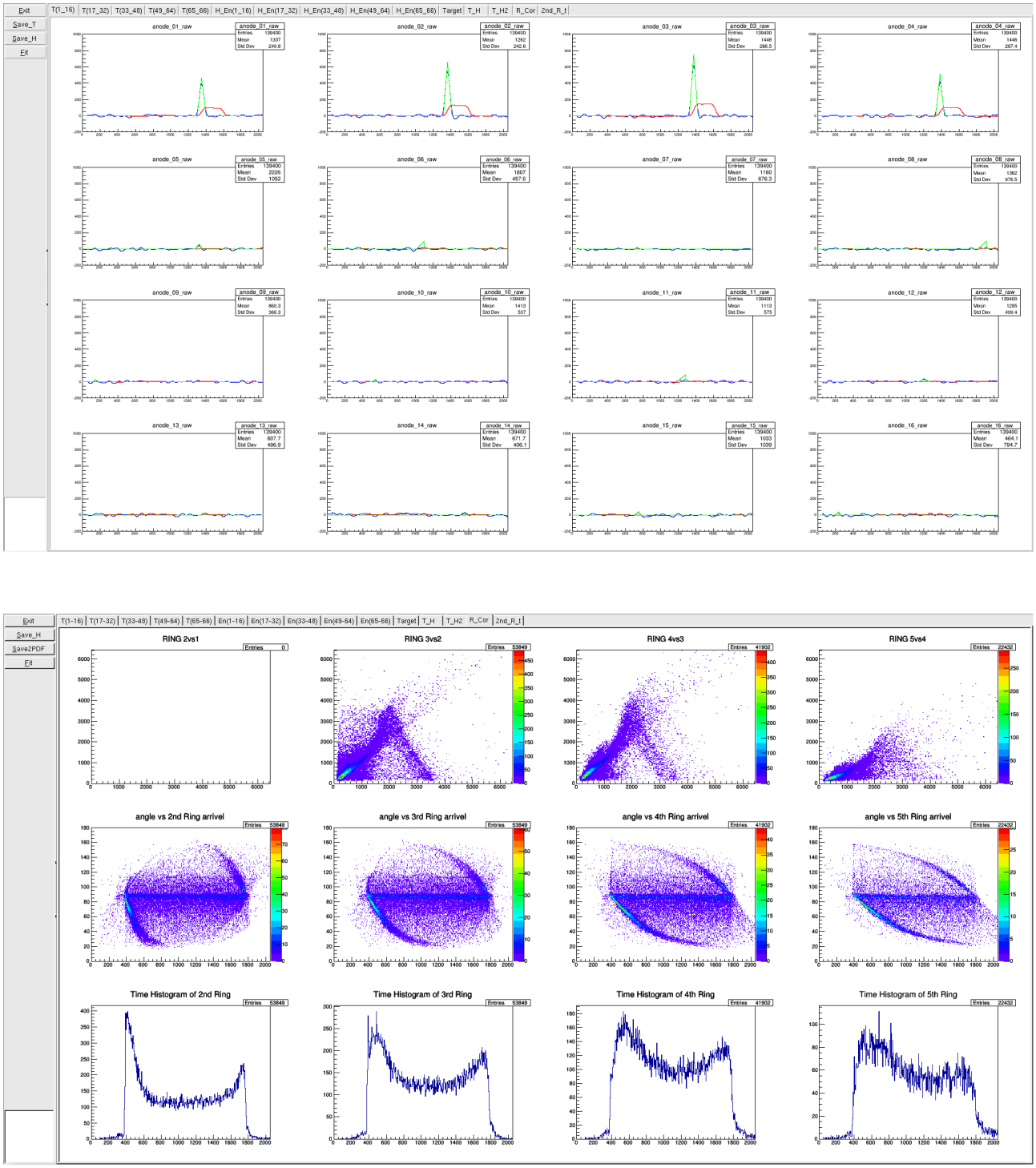

Figure B.1: Two representative screen captures showing the ATOMAT interface.

B.2 AcTar slow control

The correct operation of the AcTar relies on the stability of temperature, pressure and high-voltage parameters. During experiment such parameters are monitored by sensors equipped in the ionising chamber and the high-voltage supply modules. In order to obtain the reading of this parameter from a secured place they have to be accessed remotely. A CompactRIO control system, from National Instruments, was assembled close to the detector to allow Ethernet remote access to the parameters readings, which were then monitored in a front-end interface system build on a LabView platform an developed within this thesis. The high-voltage can as well be adjusted remotely via the same interface. Figure B.2 shows the GUI panel designed for the AcTar slow control.

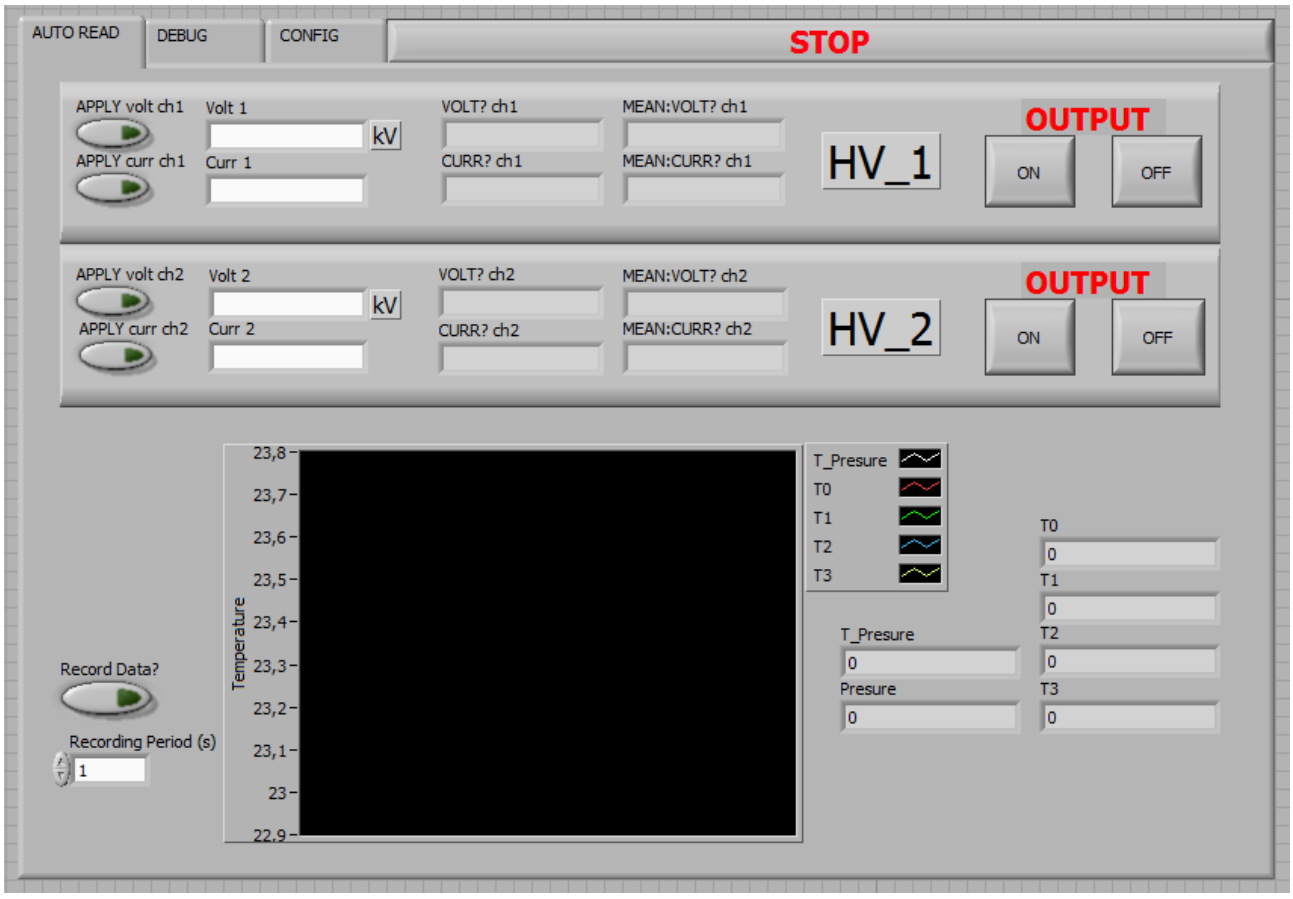

Figure B.2: Screen captures showing the ACTAR slow control interface.

Appendix C

AcTar prototype testing setup

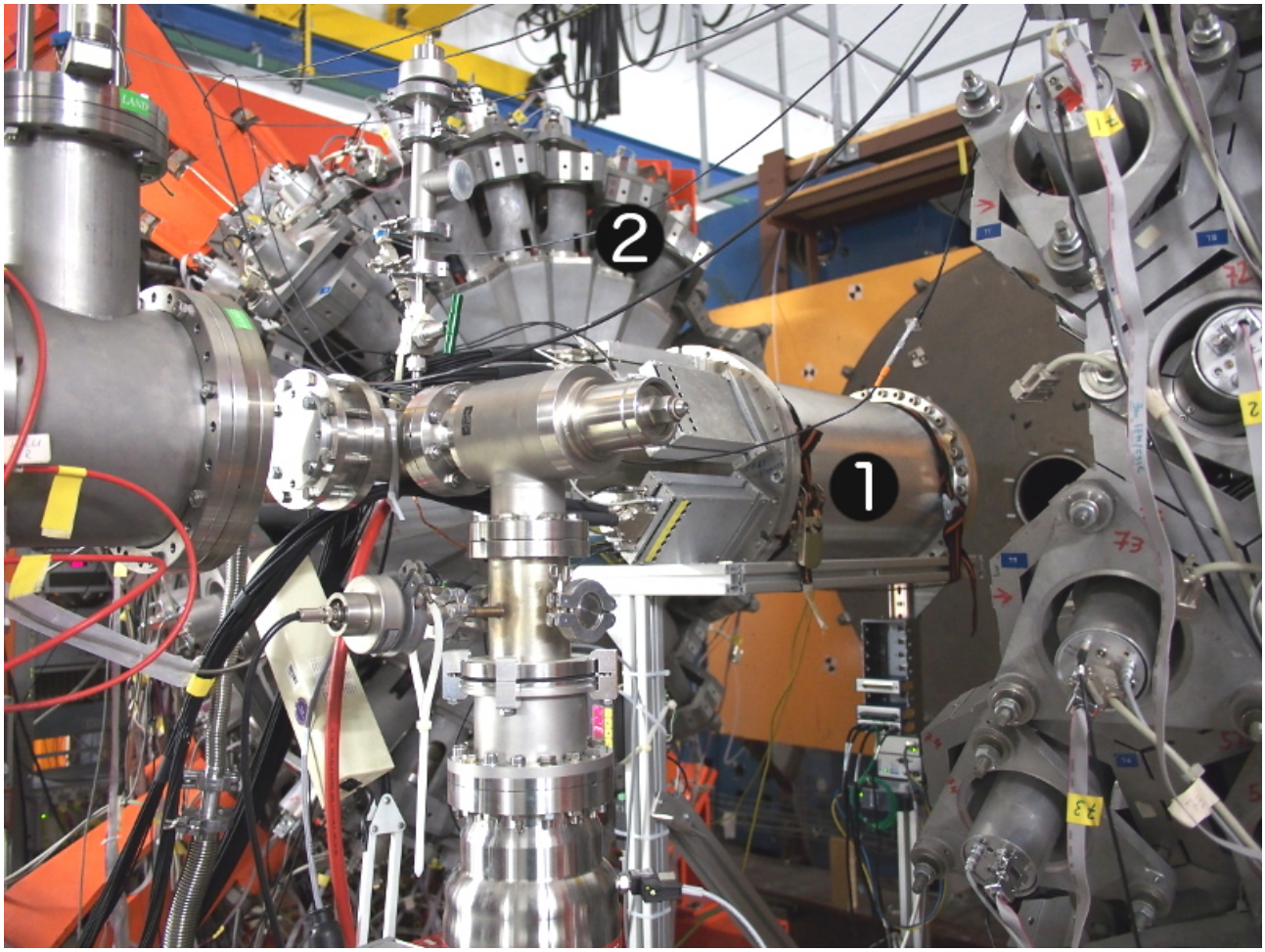

Figure C.1: Photograph of the AcTar prototype . The label in the picture indicates: 1 - the AcTar detector, 2 - the Crystal Ball calorimeter.

References

[1] H. Geiger and E. Marsden, Philosophical Magazine **LXXXIII**, 604 (1913).

[2] I. Tanihata, H. Hamagaki, O. Hashimoto, Y. Shida, N. Yoshikawa, K. Sugimoto, O. Yamakawa, T. Kobayashi, and N. Takahashi, Physical Review Letters **55**, 2676 (1985).

[3] N. N. N. Paar, D. D. D. Vretenar, E. E. E. Khan, G. Colo, and G. Colò, Rep. Prog. Phys. **70**, 691 (2007), 0701081.

[4] O. Sorlin and M. G. Porquet, Progress in Particle and Nuclear Physics **61**, 602 (2008), 0805.2561.

[5] E. Kugler, Hyperfine Interactions **129**, 23 (2000).

[6] H. Geissel, H. Weick, M. Winkler, G. Münzenberg, V. Chichkine, M. Yavor, T. Aumann, K. H. Behr, M. Böhmer, A. Brünle, et al., Nuclear Instruments and Methods in Physics Research Section B: Beam Interactions with Materials and Atoms **204**, 71 (2003).

[7] *Technical proposal for the Design, Construction, Commissioning and Operation of R3B* (2014), URL http://www.land.gsi.de/r3b/.

[8] a.a. Vorobyov, G. Korolev, A. Dobrovolsky, A. Khanzadeev, G. Petrov, E. Spiridenkov, Y. Terrien, J. Lugol, J. Saudinos, B. Silverman, et al., Nuclear Instruments and Methods in Physics Research Section A: Accelerators, Spectrometers, Detectors and Associated Equipment **270**, 419 (1988).

[9] G. Alkhazov, M. Andronenko, A. Dobrovolsky, P. Egelhof, G. Gavrilov, H. Geissel, H. Irnich, A. Khanzadeev, G. Korolev, A. Lobodenko, et al., Physical Review Letters **78**, 2313 (1997).

[10] Y. Mizoi, T. Fukuda, Y. Matsuyama, T. Miyachi, J. Nakano, N. Fukuda, M. Hirai, H. Kobinata, Y. Watanabe, H. Sakurai, et al., Nuclear Instruments and Methods in Physics Research Section A: Accelerators, Spectrometers, Detectors and Associated Equipment **431**, 112 (1999).

[11] C. Demonchy, W. Mittig, H. Savajols, P. Roussel-Chomaz, M. Chartier, B. Jurado, L. Giot, D. Cortina-Gil, M. Caamaño, G. Ter-Arkopian, et al., Nuclear Instruments and Methods in Physics Research Section A: Accelerators, Spectrometers, Detectors and Associated Equipment **573**, 145 (2007).

[12] H. Moeini, S. Ilieva, F. Aksouh, K. Boretzky, A. Chatillon, A. Corsi, P. Egelhof, H. Emling, G. Ickert, J. Jourdan, et al., Nuclear Instruments and Methods in Physics Research Section A: Accelerators, Spectrometers, Detectors and Associated Equipment **634**, 77 (2011).

[13] R. Brun and F. Rademakers, Nuclear Instruments and Methods in Physics Research, Section A: Accelerators, Spectrometers, Detectors and Associated Equipment **389**, 81 (1997).

[14] H. Nyquist, Proceedings of the IEEE **90**, 280 (2002).

[15] C. E. Shannon, Proceedings of the IEEE **86**, 447 (1998).

[16] R. Gray and D. Neuhoff, IEEE Transactions on Information Theory **44**, 2325 (1998).

[17] P. M. Figueiredo and J. C. Vital, Application Note AN-42 **Oak Ridge**, 395 (2009).

[18] B. W. Loo, F. S. Goulding, and D. Gao, IEEE Transactions on Nuclear Science **35**, 114 (1987).

[19] S. W. Smith, *Digital signal processing* (1999), ISBN 1053-5888, 97-80293.

[20] R. G. Lyons, *Understanding Digital Signal Processing, 3/E* (2011), ISBN 9780137027415.

[21] P. Marchand, Review of Scientific Instruments **54**, 1034 (1983).

[22] W. T. Eadie, D. Drijard, F. E. James, M. Roos, and B. Sadoulet, *Statistical methods in experimental physics* (American Elsevier Pub. Co (1971), 1986), ISBN 0444101179.

[23] A. Georgiev, W. Gast, and R. M. Lieder, IEEE T. Nucl. Sci. **41**, 1116 (1994).

[24] J. Stein, F. Scheuer, W. Gast, and A. Georgiev, Nuclear Instruments and Methods in Physics Research Section B: Beam Interactions with Materials and Atoms **113**, 141 (1996).

[25] M. Lauer, Ph.D. thesis (2004), URL http://archiv.ub.uni-heidelberg.de/volltextserver/id/eprint/4991.

[26] V. T. Jordanov and G. F. Knoll, Nuclear Instruments and Methods in Physics Research Section A: Accelerators, Spectrometers, Detectors and Associated Equipment **345**, 337 (1994).

[27] G. F. Knoll, *Radiation Detection and Measurement*, vol. 3 (2010), ISBN 9780470131480, arXiv:1011.1669v3.

[28] C. Hohenemser, R. Reno, and A. P. Mills, IEEE Transactions on Nuclear Science **17** (1970).

[29] B. Leskovar, *Accuracy of single photoelectron time spread measurement of fast photomultipliers* (1975).

[30] J. McGervey, J. Vogel, P. Sen, and C. Knox, *Time resolution measurements with an improved discriminator and conical scintillators* (1977).

[31] ORTEC, Application Note AN-42, Oak Ridge, Tennessee p. 24 (2000).

[32] R. E. Kalman, Journal of Basic Engineering **82**, 35 (1960).

[33] T. Alexander and F. Goulding, *An amplitude-insensitive system that distinguishes pulses of different shapes* (1961).

[34] J. Adams and G. White, Nuclear Instruments and Methods **156**, 459 (1978).

[35] E. Gatti and F. de Martini, Proceedings of the Conference on Nuclear Electronics pp. 265—-276 (1962).

[36] M. L. Roush, M. A. Wilson, and W. F. Hornyak, Nuclear Instruments and Methods **31**, 112 (1964).

[37] J. C. Bezdek, *Pattern Recognition with Fuzzy Objective Function Algoritms* (Plenum Press, 1981, 1981), ISBN 0306406713.

[38] I. Guyon, Pattern Analysis and Applications **1**, 142 (1998).

[39] D. Savran, B. Löher, M. Miklavec, and M. Vencelj, Nuclear Instruments and Methods in Physics Research Section A: Accelerators, Spectrometers, Detectors and Associated Equipment **624**, 675 (2010).

[40] J. Silva, E. Fiori, J. Isaak, B. Löher, D. Savran, M. Vencelj, and F. Wamers, Nuclear Inst. and Methods in Physics Research, A **776**, 98 (2015).

[41] R. Wirth, E. Fiori, B. Löher, D. Savran, J. Silva, H. Á. Pol, D. C. Gil, B. Pietras, T. Bloch, T. Kröll, et al., Nuclear Instruments and Methods in Physics Research Section A: Accelerators, Spectrometers, Detectors and Associated Equipment **717**, 77 (2013), 1304.1651.

[42] H. Ikeda, A. Satpathy, B. S. Ahn, V. M. Aulchenko, A. E. Bondar, B. G. Cheon, T. H. Chu, M. Fukushima, A. Y. Garmash, H. Hayashii, et al., Nuclear Instruments and Methods in Physics Research, Section A: Accelerators, Spectrometers, Detectors and Associated Equipment **441**, 401 (2000).

[43] E. Dolev, A. Manor, I. Brandys, D. Tirosh, G. Ziskind, and I. Orion, IEEE Transactions on Nuclear Science **55**, 1237 (2008).

[44] M. Kobayashi, P. Carlson, and S. Berglund, Nuclear Instruments and Methods in Physics Research Section A: Accelerators, Spectrometers, Detectors and Associated Equipment **281**, 192 (1989).

[45] J. Valentine, D. Wehe, G. Knoll, and C. Moss, in *Conference Record of the 1991 IEEE Nuclear Science Symposium and Medical Imaging Conference* (IEEE, 1991), pp. 176–182, ISBN 0-7803-0513-2, URL http://ieeexplore.ieee.org/lpdocs/epic03/wrapper.htm?arnumber=258897.

[46] R. Shepard, S. Wawrowski, M. Charland, H. Roberts, and M. Möslinger, IEEE Transactions on Nuclear Science **44**, 568 (1997).

[47] M. Vićić, L. G. Sobotka, J. F. Williamson, R. J. Charity, and J. M. Elson, Nuclear Instruments and Methods in Physics Research, Section A: Accelerators, Spectrometers, Detectors and Associated Equipment **507**, 636 (2003).

[48] J. D. Valentine, W. W. Moses, S. E. Derenzo, D. K. Wehe, and G. F. Knoll, Nuclear Instruments and Methods in Physics Research Section A: Accelerators, Spectrometers, Detectors and Associated Equipment **325**, 147 (1993).

[49] M. Grodzicka, M. Moszynski, T. Szczesniak, W. Czarnacki, M. Szawlowski, L. Swiderski, L. Kazmierczak, and K. Grodzicki, Nuclear Instruments and Methods in Physics Research Section A: Accelerators, Spectrometers, Detectors and Associated Equipment **707**, 73 (2013).

[50] A. Syntfeld-Kazuch, M. Moszynski, L. Swiderski, W. Klamra, and A. Nassalski, IEEE Transactions on Nuclear Science **55**, 1246 (2008).

[51] G. Pausch, J. Stein, and N. Teofilov, IEEE Transactions on Nuclear Science **52**, 1849 (2005).

[52] M. J. Neuer and E. Jacobs, IEEE Transactions on Nuclear Science **61**, 1304 (2014).

[53] R. S. Storey, W. Jack, and A. Ward, Proceedings of the Physical Society **72**, 1 (2002).

[54] W. Skulski and M. Momayezi, Nuclear Instruments and Methods in Physics Research, Section A: Accelerators, Spectrometers, Detectors and Associated Equipment **458**, 759 (2001).

[55] Y. Kaschuck and B. Esposito, Nuclear Instruments and Methods in Physics Research Section A: Accelerators, Spectrometers, Detectors and Associated Equipment **551**, 420 (2005).

[56] J. Kataoka, T. Saito, Y. Kuramoto, T. Ikagawa, Y. Yatsu, J. Kotoku, M. Arimoto, N. Kawai, Y. Ishikawa, and N. Kawabata, in *Nuclear Instruments and Methods in Physics Research, Section A: Accelerators, Spectrometers, Detectors and Associated Equipment* (2005), vol. 541, pp. 398–404, 0602391v1.

[57] T. Ikagawa, J. Kataoka, Y. Yatsu, T. Saito, Y. Kuramoto, N. Kawai, M. Kokubun, T. Kamae, Y. Ishikawa, and N. Kawabata, Nuclear Instruments and Methods in Physics Research, Section A: Accelerators, Spectrometers, Detectors and Associated Equipment **538**, 640 (2005).

[58] A. Bejan and A. D. Kraus, *Heat Transfer Handbook* (2003), ISBN 0471390151.

[59] W. Assmann, J. De Boer, U. Meyer-Berkhout, S. Skorka, E. Huenges, P. Kienle, H. Morinaga, E. Nolte, H. Vonach, H. Münzer, et al., Nuclear Instruments and Methods **122**, 191 (1974).

[60] a. M. Laird, A. Parikh, a. S. J. Murphy, K. Wimmer, a. a. Chen, C. M. Deibel, T. Faestermann, S. P. Fox, B. R. Fulton, R. Hertenberger, et al., Physical Review Letters **110**, 1 (2013).

[61] T. Aumann, *Technical Report for the Design, Construction and Commissioning of The CALIFA Barrel: The R3B CALorimeter for In Flight detection of gamma-rays and high energy charged pArticles.* (2011).

[62] H. Alvarez-Pol, J. Benlliure, E. Casarejos, D. Cortina, I. Durán, and M. Gascón, Nuclear Instruments and Methods in Physics Research, Section B: Beam Interactions with Materials and Atoms **266**, 4616 (2008).

[63] D. D. DiJulio, V. Avdeichikov, J. Cederkall, P. Golubev, B. Jakobsson, H. Johansson, and C. Tintori, Nuclear Instruments and Methods in Physics Research, Section A: Accelerators, Spectrometers, Detectors and Associated Equipment **612**, 127 (2009).

[64] J. Hoffmann, *FEBEX 2* (2011).

[65] H. Grassman, E. Lorenz, and H. Moser, Nuclear Instruments and Methods in Physics Research Section A: Accelerators, Spectrometers, Detectors and Associated Equipment **228**, 323 (1985).

[66] R. H. Bartram and A. Lempicki, Journal of Luminescence **68**, 225 (1996).

[67] M. Moszynski, Nuclear Instruments and Methods in Physics Research Section A: Accelerators, Spectrometers, Detectors and Associated Equipment **505**, 101 (2003).

[68] F. Benrachi, B. Chambon, B. Cheynis, D. Drain, C. Pastor, D. Seghier, K. Zaid, A. Giorni, D. Heuer, A. Llères, et al., Nuclear Instruments and Methods in Physics Research Section A: Accelerators, Spectrometers, Detectors and Associated Equipment **281**, 137 (1989).

[69] P. Schotanus and R. Kamermans, IEEE Transactions on Nuclear Science **37**, 177 (1990).

[70] V. Nagirnyi, S. Zazubovich, V. Zepelin, M. Nikl, and G. P. Pazzi, **227**, 533 (1994).

[71] V. Nagirnyi, A. Stolovich, S. Zazubovich, V. Zepelin, E. Mihokova, M. Nikl, G. P. Pazzi, and L. Salvini, Journal of Physics: Condensed Matter **7**, 3637 (1995).

[72] S. Zazubovich, Radiation Measurements **33**, 699 (2001).

[73] R. Gwin and R. B. Murray, Physical Review **131**, 501 (1963).

[74] M. M. Hamada, F. E. Costa, M. C. C. Pereira, and S. Kubota, IEEE Transactions on Nuclear Science **48**, 1148 (2001).

[75] J. C. Robertson, J. G. Lynch, and W. Jack, Proceedings of the Physical Society **78**, 1188 (1961).

[76] J. Alarja, A. Dauchy, A. Giorni, C. Morand, E. Pollaco, P. Stassi, R. Billerey, B. Chambon, B. Cheynis, D. Drain, et al., Nuclear Instruments and Methods in Physics Research Section A: Accelerators, Spectrometers, Detectors and Associated Equipment **242**, 352 (1986).

[77] T. Ikagawa, J. Kataoka, Y. Yatsu, N. Kawai, K. Mori, T. Kamae, H. Tajima, T. Mizuno, Y. Fukazawa, Y. Ishikawa, et al., Nuclear Instruments and Methods in Physics Research, Section A: Accelerators, Spectrometers, Detectors and Associated Equipment **515**, 671 (2003).

[78] J. Pansart, Nuclear Instruments and Methods in Physics Research Section A: Accelerators, Spectrometers, Detectors and Associated Equipment **387**, 186 (1997).

[79] D. Renker, in *Nuclear Instruments and Methods in Physics Research, Section A: Accelerators, Spectrometers, Detectors and Associated Equipment* (2002), vol. 486, pp. 164–169.

[80] M. Moszynski, M. Szawlowski, M. Kapusta, M. Balcerzyk, M. Moszynski, M. Szawlowski, M. Kapusta, and M. Balcerzyk, Nuclear Instruments and Methods in Physics Research, Section A: Accelerators, Spectrometers, Detectors and Associated Equipment **497**, 226 (2003).

[81] M. Gascon, H. Alvarez-Pol, J. Benlliure, E. Casarejos, D. Cortina-Gil, and I. Duran, IEEE Transactions on Nuclear Science **55**, 1259 (2008).

[82] R. Sato, J. Kataoka, Y. Kanai, Y. Ishikawa, N. Kawabata, T. Ikagawa, T. Saito, Y. Kuramoto, and N. Kawai, Nuclear Instruments and Methods in Physics Research, Section A: Accelerators, Spectrometers, Detectors and Associated Equipment **556**, 535 (2006).

[83] S. Kubota, S. Sakuragi, S. Hashimoto, and J.-z. Ruan, Nuclear Instruments and Methods in Physics Research Section A: Accelerators, Spectrometers, Detectors and Associated Equipment **268**, 275 (1988).

[84] J. Stein, A. Kreuels, Y. Kong, R. Lentering, K. Ruhnau, F. Scherwinski, and A. Wolf, Nuclear Instruments and Methods in Physics Research Section A: Accelerators, Spectrometers, Detectors and Associated Equipment **782**, 20 (2015).

[85] P. Webb, R. McIntyre, and J. Conradi, R.C.A. Review **35**, 234 (1974).

[86] T. Mitchell, *Machine Learning: A Guide to Current Research* (McGraw-Hill, 1997), ISBN 0070428077.

[87] J. Burq, M. Chemarin, M. Chevallier, A. Denisov, T. Ekelof, J. Fay, P. Grafstrom, L. Gustafsson, E. Hagberg, B. Ille, et al., Nuclear Instruments and Methods **177**, 353 (1980).

[88] A. V. Dobrovolsky, G. D. Alkhazov, M. N. Andronenko, A. Bauchet, P. Egelhof, S. Fritz, H. Geissel, C. Gross, A. V. Khanzadeev, G. A. Korolev, et al., Nuclear Physics A **766**, 1 (2006).

[89] S. P. Ahlen, Reviews of Modern Physics **52**, 121 (1980).

[90] F. J. Hambsch and I. Ruskov, Nuclear Science and Engineering **163**, 1 (2009).

[91] A. Al-Adili, F.-J. Hambsch, S. Pomp, and S. Oberstedt, Physical Review C **86**, 054601 (2012).

[92] P. Christmas, Radiation Physics and Chemistry (1977) **16**, 493 (1980).

[93] H. T. Johansson, *The UCESB unpacker generator, Long write-up documentation and manual*, http://fy.chalmers.se/~f96hajo/ucesb (2010), URL `http://fy.chalmers.se/f96hajo/ucesb`.

[94] H. Bethe, Annalen der Physik **397**, 325 (1930).

[95] F. Bloch, Annalen der Physik **16**, 285 (1933).

[96] J. F. Ziegler, M. Ziegler, and J. Biersack, Nuclear Instruments and Methods in Physics Research Section B: Beam Interactions with Materials and Atoms **268**, 1818 (2010).

[97] J. Burq, M. Chemarin, M. Chevallier, A. Denisov, T. Ekelöf, J. Fay, P. Grafström, L. Gustafsson, E. Hagberg, B. Ille, et al., Nuclear Physics B **187**, 205 (1981).

[98] J. Burq, M. Chemarin, M. Chevallier, A. Denisov, C. Doré, T. Ekelöf, J. Fay, P. Grafström, L. Gustafsson, E. Hagberg, et al., Nuclear Physics B **217**, 285 (1983).

[99] J. L. Pack and A. V. Phelps, Phys. Rev. **121**, 798 (1961).

[100] E. k. Byckling and Kajantie, *Particle Kinematics* (John Wiley andd Sons Ltd (January 1, 1973), 1973), ISBN 9780471128854.

Publication

Temperature gain correction for CsI(Tl) detection systems based on digital pulse shape analysis

Nuclear Inst. and Methods in Physics Res. A 776, 98-106 (2015)
DOI: 10.1016/j.nima.2014.12.064

Particle identification using clustering algorithms

Nuclear Inst. and Methods in Physics Res. A 717, 77-82 (2013)
DOI: 10.1016/j.nima.2013.14.006

List of Figures

List of Tables

Abbreviations

AcTar Active-Target 3, 6, 8, 75–84, 86–97, 99, 100, 105, 107, 109

ADC Analogue to Digital Converter 3, 7, 9–11, 15, 23, 25, 26, 30, 34, 45, 52, 53, 105

APD Avalanche Photo-Diode 7, 8, 20, 40–48, 50–67, 69, 99, 100

ATOMAT Active-Target Online Monitoring and Analysis Tool 83, 105

BMA Bipolar Moving Average 12, 16–19, 56

CALIFA CALorimeter for In-Flight emitted gAmmas 3, 6–8

CFD Constant Fraction Discriminator 26–29, 53, 54, 71

CM Centre-of-Mass 85

DAQ Data AcQuisition 6, 81–83

DSA Digital Signal Analysis 9, 10

DSP Digital Signal Processing 9

EXL EXotic nuclei studied in Light ion induced reactions at the NESR storage ring 6

FADC Flash-ADC 81, 82, 86, 87, 89, 91–94

FAIR Facility for Antiproton and Ion Research 1, 2

FCM Fuzzy C-Means 36, 37

FIR Finite Impulse Response 12, 16, 19, 24, 82

FRS FRagment Separator 2

GSI GSI Helmholtzzentrum für Schwerionenforschung GmbH 2, 5, 76, 77, 83

GUI Graphical User Interface 83

IC Ionisation Chamber 6

ISOL Isotope Separation On-Line 2

LED Light-Emitting Diode 41

LET Leading Edge Trigger 25, 26, 53, 54

LMD List Mode Data 83, 105

MA Moving Average 12–15, 19, 33, 54, 56

MAD Mean Absolute Deviation 25

MB Moving Binomial 12, 14, 15, 19, 53–55, 86

MBS Multi-Branch System 83

MG Moving Gradient 12, 15–17, 19, 29, 86

MPS Mean Pulse Shape 99

MWD Moving Window Deconvolution 11, 12, 20–23, 54, 55

PD Photodiode 47

PID Particle IDentification 42, 52, 67, 68, 70, 71, 100

PMT Photomultiplier Tube 8, 40–44, 47–50, 53, 54, 56–67, 99

PPS Principal Pulse Shape 23, 31–35, 56–58, 60–63, 67–73, 100

PSA Pulse Shape Analysis 23, 41, 42, 52, 67, 99, 100

PSD Pulse Shape Discrimination 30, 31, 33

QE Quantum Efficiency 47

R^{3}B Reactions with Relativistic Radioactive Beams ..... i, 2, 3, 6, 8, 75, 76, 100

RIB Radioactive Ion Beam 4, 76

RMS Root Mean Square 24, 53, 54, 56, 87

Super-FRS Super FRagment Separator 2

TPC Time Projection Chamber 76

Acknowledge

Curriculum Vitae